An advanced light scattering imaging model for total internal reflection microscopy considering a stratified medium

Alexandru Doicu [a], Dmitry S. Efremenko [b,*], Christopher L. Wirth [c], Thomas Wriedt [d]

[a] *Invenio Virtual Technologies GmbH, Robert-Bürkle-Straße 3, Ismaning, 85737, Germany*

[b] *Deutsches Zentrum für Luft- und Raumfahrt (DLR), Institut für Methodik der Fernerkundung (IMF), Munchener Str 20, Wessling, 82234, Germany*

[c] *Chemical and Biomolecular Engineering Department, Case Western Reserve University, 10900 Euclid Ave, Cleveland, OH, 44106, USA*

[d] *Leibniz-Institut für Werkstofforientierte Technologien - IWT, University of Bremen, Badgasteiner Str. 3, Bremen, 28359, Germany*

ARTICLE INFO

ABSTRACT

An advanced light scattering model for Total Internal Reflection Microscopy (TIRM) is presented. The model considers the specific TIRM geometry and deals with the scattering by an axisymmetric particle of arbitrary orientation placed in a stratified medium and the imaging of the scattered field. The scattered field is computed by truncating the scattered and internal field expansions and by using spherical and plane wave expansions for the free-space dyadic Green's function. While the first expansion is valid outside a sphere enclosing the particle, the second one is valid outside the tangent planes bounding the particle from above and below. We demonstrate that in both cases, the results are the same, and thus, that the restrictive condition according to which the interface should not intersect the particle's circumscribed sphere is not relevant. The image of the scattered field is computed by using the Debye diffraction integral and fast Fourier transform, while for a better reconstruction of the particle orientation, an image processing step consisting in a contour extraction and ellipse fitting is considered. The numerical simulations dealing with scattering by a prolate spheroid provide evidence of the remarkably sensitivity of the geometric parameters of the image ellipse to the particle orientation angles, as well as, of the integral response of the detector to the distance between the particle and the interface.

1. Introduction

Nano- to micrometer scale 'colloidal' particles regularly interact with nearby surfaces including neighboring particles and boundaries via weak kT scale interactions [1,2]. These surface interactions are responsible for a wide variety of important phenomena, including particle deposition [3–5] and the rheological response of a colloidal suspension [6–10]. Robust experimental techniques, including the Colloidal Probe Atomic Force Microscope and the Surface Force Apparatus, have been developed and adopted to measure surface interactions, but are limited due to the feature that force is measured via the mechanical manipulation of two surfaces relative to each other. Total Internal Reflection Microscopy (TIRM) was developed to infer the potential energy landscape and associated weak surface forces experienced by a particle undergoing thermal fluctuations very near a boundary [11–13]. TIRM has since been used to measure a variety of both conservative (path independent, e.g. electrostatics) and non-conservative (path dependent, e.g. hydrodynamics) surface interactions for spheres [14–18]. More recent work on Scattering Morphology Resolved TIRM has started to extend this technique to non-spherical particles by extracting reporters

of a particle's position and orientation via analysis of the morphology of light scattered by a particle [19–21].

The TIRM setup is illustrated in Fig. 1. It consists of a linearly polarized incident beam, a hemispherical glass prism, a microfluidic cell, a microscope objective, and a CCD camera. Note a dovetail prism is often used during TIRM, but recent work has shown a hemispherical prism can be used to systematically adjust azimuthal angle of the incident beam [22]. The sample is suspended in an aqueous solution inside the microfluidic cell. The cell, placed on top of the prism using refractive index matching oil, is made of a thick microscope slide at the bottom and a thin cover slide at the top. Although not necessary, a thin coating is often deposited on the bottom microscope slide of the cell to measure the influence of particular materials on the surface interactions experienced by a particle. The scattered light of isolated particles attached to the glass surface is collected with a microscope objective directly above the sample, and then analyzed by a CCD camera.

In Doicu et al. [19], we described a mathematical model for TIRM. In Yan et al. [21], Vasilyeva et al. [23] it was compared with experiments for investigating the scattering morphology of a spherical

---

Fig. 1. Simplified TIRM setup.

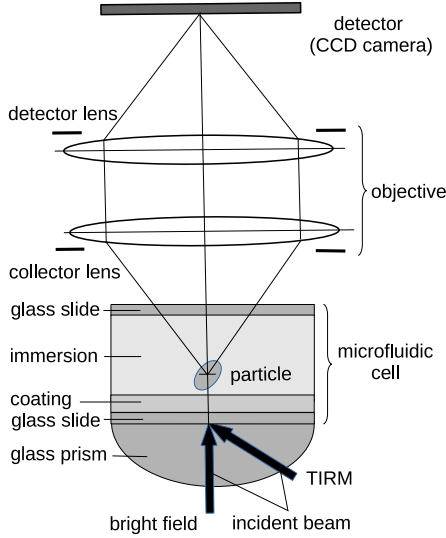**Fig. 2.** Geometry of the layer system. The particle is placed in layer 2, and the outmost layers 0 and 4 are semi-infinite in size.

particle. The model treats the scattering by an axisymmetric particle of arbitrary orientation near a plane surface, and the imaging of the scattered field. In the present paper, we intend to design a more realistic model that better reproduces the TIRM setup. More precisely, we want to take into account the fact that the particle is not near a plane surface separating two half-spaces, but rather in a stratified medium. As in Doicu et al. [19], we aim to consider both the scattering by an axisymmetric particle situated in a stratified medium and the imaging of the scattered field via microscope optics.

The paper is organized as follows. In Section 2 we describe the mathematical model for TIRM, in Section 3 we present a numerical analysis regarding the possibility to measure the particle orientation angles and the separation distance, and in Section 4 we formulate some conclusions and discuss a few feature goals.

2. Theory

In this section, we analyze the scattering by a particle in a stratified medium and describe the imagining of the scattered field.

2.1. Scattering by a particle in a stratified medium

A python package for the simulation of light scattering by multiple particles near or between planar interfaces was designed by Egel et al. [24]. The software package uses the T-matrix method for analyzing the individual particle scattering and the scattering matrix formalism for analyzing the electromagnetic field propagation through planar interfaces. Although the basic ideas are the same, we prefer to develop our own formalism which extends the one presented in Doicu et al. [19] and is devoted to the concrete TIRM geometry we are analyzing.

In our model, the stratified medium is a succession of air–glass–immersion-coating–glass interfaces, in which the "immersion" layer is an aqueous solution. The incident field propagates in the glass prism, the particle is placed in the immersion layer, and the outmost layers are semi-infinite in size. The multiple scattering problem is solved by the superposition method. To develop a scattering model we need to understand the interaction process of the radiation with the particle. The incident field strikes the particle either directly or after interacting with the layer system. The resulting field is the incident field in the immersion. On the other hand, the fields scattered by the particle also interact with the layer system and strike the particle again. In this regard, the total field in the immersion layer (containing the particle) can be decomposed into a sum of three constituents:
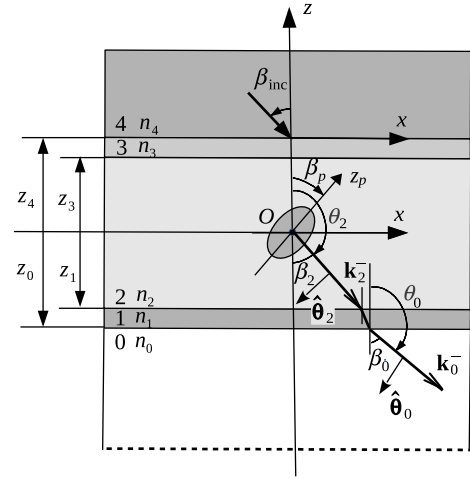
1. the incident field in the immersion layer,
2. the field scattered by the particle, and
3. the layer system response to the scattered field.

By convention, the layer system response to the scattered field will be called the interacting field. The incident field in the immersion layer together with the interacting field make the excitation field. The layer system responses are first computed as plane wave expansions after which, they are transformed into regular spherical wave expansions. As a result, a series representation for the excitation field in terms of regular spherical waves is obtained. The spherical wave expansion co-efficients of the scattered field are then linked to those of the excitation field through the transition matrix of the particle.

We consider the layer system illustrated in Fig. 2. The absolute refractive index and the wavenumber in medium j are denoted by n_j and $k_j = n_j k$, respectively, where $k = 2\pi/\lambda$ and λ are the wavenumber and the wavelength in vacuum, respectively. An axisymmetric particle of arbitrary orientation is placed in layer 2. The Cartesian coordinate system $Oxyz$ centered at the particle and having the z-axis perpendicular to the layer interfaces represents the global coordinate system. The orientation of the particle is described by the Euler orientation angles (α_p, β_p) and we denote by $Ox_p y_p z_p$ the particle (local) coordinate system. To deal with an arbitrary particle orientation, the rotation addition theorem for vector spherical vector functions will be used. In general, if the particle coordinate system $Ox_p y_p z_p$ is obtained by a rigid-body rotation of the global coordinate system $Oxyz$ with the Euler angles $(\alpha_p, \beta_p, \gamma_p)$, the addition theorem for vector spherical wave functions under coordinate rotations is [25]

$$\mathbf{M}_{mn}^{1,3}(kr, \theta, \varphi) = \sum_{m_1=-n}^{n} D_{m_1 m}^{n}(\alpha_p, \beta_p, \gamma_p) \mathbf{M}_{m_1 n}^{1,3}(kr, \theta_p, \varphi_p), \tag{1}$$

$$\mathbf{N}_{mn}^{1,3}(kr, \theta, \varphi) = \sum_{m_1=-n}^{n} D_{m_1 m}^{n}(\alpha_p, \beta_p, \gamma_p) \mathbf{N}_{m_1 n}^{1,3}(kr, \theta_p, \varphi_p), \tag{2}$$

where $D_{mm'}^{n}$ are the Wigner D-function, (r, θ, φ) are the spherical coordinates of a point in the global coordinate system $Oxyz$, and (r, θ_p, φ_p) are the spherical coordinates of the same point in the particle coordinate system $Ox_p y_p z_p$. Some basic results that will be used frequently in what follows are given in appendices. In particular, the expressions of the vector spherical wave functions and vector plane waves, as well as the transformations between them are given in Appendix A, while the main relations describing the scattering in a stratified medium and which are relevant for computing the interacting field are given in Appendix B.

2.1.1. The incident field in the immersion layer (layer 2)

The incident field is a plane electromagnetic wave propagating in the half-space 4, the azimuthal plane α_{inc} and the direction $\pi - \beta_{\mathrm{inc}}$, where β_{inc} is the angle of incidence. In the global coordinate system $Oxyz$, the incident field in the half-space 4, is given by

$$\mathbf{E}_{4\mathrm{inc}}(\mathbf{r}) = (\cos\alpha_{\mathrm{pol}}\widehat{\boldsymbol{\theta}}_4 + \sin\alpha_{\mathrm{pol}}\widehat{\boldsymbol{\varphi}}_4)e^{j\mathbf{k}_4^-\cdot\mathbf{r}}$$
$$= A\mathbf{M}(\mathbf{r}, \mathbf{k}_4^-) + B\mathbf{N}(\mathbf{r}, \mathbf{k}_4^-), \tag{3}$$

where $\mathbf{M}(\mathbf{r}, \mathbf{k}_4^-)$ and $\mathbf{N}(\mathbf{r}, \mathbf{k}_4^-)$ are the vector plane waves defined in Appendix A, $\mathbf{k}_4^- = (k_4, \pi - \beta_{\mathrm{inc}}, \alpha_{\mathrm{inc}}) = \mathbf{k}_\perp - k_z^{(4)}\widehat{\mathbf{z}}$, $k_z^{(4)} = k_4 \cos\beta_{\mathrm{inc}}$, $\widehat{\boldsymbol{\theta}}_4 = \widehat{\boldsymbol{\theta}}(\widehat{\mathbf{k}}_4^-)$, $\widehat{\boldsymbol{\varphi}}_4 = \widehat{\boldsymbol{\varphi}}(\widehat{\mathbf{k}}_4^-)$, $\widehat{\mathbf{k}}_4^- = \mathbf{k}_4^-/k_4$, $A = j\sin\alpha_{\mathrm{pol}}$, $B = -\cos\alpha_{\mathrm{pol}}$, and α_{pol} is the polarization angle.

In Appendix B it is shown that for an external excitation represented by the vector plane waves propagating downward in the half-space 4, $\mathbf{E}_4^- = \mathbf{M}(\mathbf{r}, \mathbf{k}_4^-)$ and $\mathbf{E}_4^- = \mathbf{N}(\mathbf{r}, \mathbf{k}_4^-)$, the total upward propagating fields in layer 2 are $\mathbf{E}_{2\mathrm{tot}}^+ = \widetilde{S}_\perp^+\mathbf{M}(\mathbf{r}, \mathbf{k}_2^+)$ and $\mathbf{E}_{2\mathrm{tot}}^+ = \widetilde{S}_\parallel^+\mathbf{N}(\mathbf{r}, \mathbf{k}_2^+)$, respectively, while the total downward propagating field are $\mathbf{E}_{2\mathrm{tot}}^- = \widetilde{S}_\perp^-\mathbf{M}(\mathbf{r}, \mathbf{k}_2^-)$ and $\mathbf{E}_{2\mathrm{tot}}^- = \widetilde{S}_\parallel^-\mathbf{N}(\mathbf{r}, \mathbf{k}_2^-)$, respectively. The expressions for the scattering coefficients $\widetilde{S}_X^+$ and $\widetilde{S}_X^-$, X $=\perp, \parallel$, are given by Eqs. (B.15) and (B.16), respectively. As a result, we deduce that in layer 2, the incident field exciting the particle is

$$\mathbf{E}_{2\mathrm{inc}}(\mathbf{r}) = \mathcal{A}^+\mathbf{M}(\mathbf{r}, \mathbf{k}_2^+) + \mathcal{A}^-\mathbf{M}(\mathbf{r}, \mathbf{k}_2^-)$$
$$+ \mathcal{B}^+\mathbf{N}(\mathbf{r}, \mathbf{k}_2^+) + \mathcal{B}^-\mathbf{N}(\mathbf{r}, \mathbf{k}_2^-), \tag{4}$$

where

$$\mathcal{A}^+ = A\widetilde{S}_\perp^+, \quad \mathcal{A}^- = A\widetilde{S}_\perp^-, \quad \mathcal{B}^+ = B\widetilde{S}_\parallel^+, \quad \mathcal{B}^- = B\widetilde{S}_\parallel^-. \tag{5}$$

Making use of the spherical wave expansions of the upward and downward propagating vector plane waves as given by Eqs. (A.19)–(A.20) and (A.23)–(A.24), respectively, and taking into account Eqs. (A.21)–(A.22), we find

$$\mathbf{E}_{2\mathrm{inc}}(\mathbf{r}) = \sum_{n=1}^{\infty}\sum_{m=-n}^{n} C_n[A_{mn}\mathbf{M}_{mn}^1(k_2\mathbf{r}) + B_{mn}\mathbf{N}_{mn}^1(k_2\mathbf{r})], \tag{6}$$

where $\mathbf{M}_{mn}^1(k_2\mathbf{r}) = \mathbf{M}_{mn}^1(k_2r, \theta, \varphi)$ and $\mathbf{N}_{mn}^1(k_2\mathbf{r}) = \mathbf{N}_{mn}^1(k_2r, \theta, \varphi)$ are the regular vector spherical wave functions defined in Appendix A,

$$A_{mn} = C_n\{\mathcal{A}^+\tau_n^{|m|}(\beta_2) + \mathcal{A}^-\tau_n^{|m|}(\pi - \beta_2)$$
$$+ m[\mathcal{B}^+\pi_n^{|m|}(\beta_2) + \mathcal{B}^-\pi_n^{|m|}(\pi - \beta_2)]\}e^{-jm\alpha_{\mathrm{inc}}}, \tag{7}$$

$$B_{mn} = C_n\{m[\mathcal{A}^+\pi_n^{|m|}(\beta_2) + \mathcal{A}^-\pi_n^{|m|}(\pi - \beta_2)]$$
$$+ \mathcal{B}^+\tau_n^{|m|}(\beta_2) + \mathcal{B}^-\tau_n^{|m|}(\pi - \beta_2)\}e^{-jm\alpha_{\mathrm{inc}}}, \tag{8}$$

and

$$C_n = \frac{4j^{n+1}}{\sqrt{2n(n+1)}}. \tag{9}$$

In Eqs. (7)–(8), the angle of refraction β_2 corresponds to the angle of incidence β_{inc}, i.e., $\cos\beta_2 = \pm\sqrt{1 - (n_4/n_2)^2 \sin^2\beta_{\mathrm{inc}}}$, with $\mathrm{Im}(\cos\beta_2) \geq 0$. Finally, application of the rotation addition theorem for vector spherical wave functions (cf. Eqs. (1)–(2)) yields the following expansion of the incident field in the particle coordinate system $Ox_py_pz_p$:

$$\mathbf{E}_{2\mathrm{inc}}(\mathbf{r}) = \sum_{n=1}^{\infty}\sum_{m=-n}^{n}[a_{mn}\mathbf{M}_{mn}^1(k_2r, \theta_p, \varphi_p) + b_{mn}\mathbf{N}_{mn}^1(k_2r, \theta_p, \varphi_p)], \tag{10}$$

where

$$a_{mn} = \sum_{m_1=-n}^{n} D_{mm_1}^n(\alpha_p, \beta_p, 0)A_{m_1n}, \quad b_{mn} = \sum_{m_1=-n}^{n} D_{mm_1}^n(\alpha_p, \beta_p, 0)B_{m_1n}, \tag{11}$$

or in matrix form,

$$\begin{bmatrix} a_{mn} \\ b_{mn} \end{bmatrix} = \mathrm{D}_\infty \begin{bmatrix} A_{m_1n} \\ B_{m_1n} \end{bmatrix}, \quad \mathrm{D}_\infty = \begin{bmatrix} D_{mm_1}^n(\alpha_p, \beta_p, 0) & 0 \\ 0 & D_{mm_1}^n(\alpha_p, \beta_p, 0) \end{bmatrix}. \tag{12}$$

2.1.2. The scattered field in the immersion layer (layer 2)

In the global coordinate system $Oxyz$, the Stratton–Chu formula for the scattered field gives

$$\mathbf{E}_{2\mathrm{sct}}(\mathbf{r}) = \oint_{S_p}\{[\nabla\times\overline{\mathbf{G}}_0(k_2, \mathbf{r}, \mathbf{r}_1)]\cdot\mathbf{e}_{\mathrm{int}}(\mathbf{r}_1) + j\omega\mu_0\overline{\mathbf{G}}_0(k_2, \mathbf{r}, \mathbf{r}_1)\cdot\mathbf{h}_{\mathrm{int}}(\mathbf{r}_1)\} \, d^2\mathbf{r}_1, \tag{13}$$

where $\overline{\mathbf{G}}_0(k_2, \mathbf{r}, \mathbf{r}_1)$ is the free-space dyadic Green's function with wavenumber k_2, $\mathbf{e}_{\mathrm{int}}$ and $\mathbf{h}_{\mathrm{int}}$ are the tangential components of the electric and magnetic internal fields (inside the particle), respectively, ω is the frequency, μ_0 is the magnetic permeability in vacuum, and the integration is performed over the particle surface S_p. Specific representations for the scattered field can be obtained by expanding the dyadic Green's function $\overline{\mathbf{G}}_0(k_2, \mathbf{r}, \mathbf{r}_1)$ in terms of vector spherical wave functions or vector plane waves. In the following we consider the spherical wave expansion, i.e.,

$$\overline{\mathbf{G}}_0(k_2, \mathbf{r}, \mathbf{r}_1) = -\frac{1}{k_2^2}\delta(\mathbf{r} - \mathbf{r}_1)\widehat{\mathbf{r}}\otimes\widehat{\mathbf{r}}$$
$$+ \frac{jk_2}{\pi}\sum_{n=1}^{\infty}\sum_{m=-n}^{n}\begin{cases} \mathbf{M}_{mn}^1(k_2\mathbf{r})\otimes\mathbf{M}_{-mn}^3(k_2\mathbf{r}_1) + \mathbf{N}_{mn}^1(k_2\mathbf{r})\otimes\mathbf{N}_{-mn}^3(k_2\mathbf{r}_1), \\ \qquad\qquad\qquad\qquad\qquad\qquad\qquad r < r_1 \\ \mathbf{M}_{mn}^3(k_2\mathbf{r})\otimes\mathbf{M}_{-mn}^1(k_2\mathbf{r}_1) + \mathbf{N}_{mn}^3(k_2\mathbf{r})\otimes\mathbf{N}_{-mn}^1(k_2\mathbf{r}_1), \\ \qquad\qquad\qquad\qquad\qquad\qquad\qquad r > r_1 \end{cases}. \tag{14}$$

The derivation based on the plane wave expansion of the dyadic Green's function is given in Appendix C. For a field point $\mathbf{r}$ lying on a sphere with radius R enclosing the particle, the expansion of the dyadic Green's function yields the series representation

$$\mathbf{E}_{2\mathrm{sct}}(\mathbf{r}) = \sum_{n=1}^{\infty}\sum_{m=-n}^{n}[F_{mn}\mathbf{M}_{mn}^3(k_2\mathbf{r}) + G_{mn}\mathbf{N}_{mn}^3(k_2\mathbf{r})]. \tag{15}$$

For a numerical implementation, we truncate the infinite series (15) by letting $m = -M_{\mathrm{rank}}, \ldots, M_{\mathrm{rank}}$ and $n = \max(1, |m|), \ldots, N_{\mathrm{rank}}$, where N_{rank} and M_{rank} are the maximum expansion and azimuthal orders, respectively. To simplify the writing, the finite summation $\sum_{m=-M_{\mathrm{rank}}}^{M_{\mathrm{rank}}}\sum_{n=\max(1,|m|)}^{N_{\mathrm{rank}}}$ will be written as $\sum_{(m,n)=1}^{N}$, where the multi-index $\nu = (m, n)$ ranges from 1 to N, when m ranges from $-M_{\mathrm{rank}}$ to M_{rank}, and n from $\max(1, |m|)$ to N_{rank}. In other words, we consider an approximate scattered field expressed as a (finite) linear combination of radiating vector spherical wave functions

$$\mathbf{E}_{2\mathrm{sct}}^N(\mathbf{r}) = \sum_{(m,n)=1}^{N}[F_{mn}^N\mathbf{M}_{mn}^3(k_2\mathbf{r}) + G_{mn}^N\mathbf{N}_{mn}^3(k_2\mathbf{r})], \tag{16}$$

which in the particle coordinate systems $Ox_py_pz_p$, takes the form

$$\mathbf{E}_{2\mathrm{sct}}^N(\mathbf{r}) = \sum_{(m,n)=1}^{N}[f_{mn}^N\mathbf{M}_{mn}^3(k_2r, \theta_p, \varphi_p) + g_{mn}^N\mathbf{N}_{mn}^3(k_2r, \theta_p, \varphi_p)], \tag{17}$$

where

$$F_{m_1n}^N = \sum_{m=-\min(n,M_{\mathrm{rank}})}^{\min(n,M_{\mathrm{rank}})} D_{m_1m}^n(0, -\beta_p, \alpha_p)f_{mn}^N,$$

$$G_{m_1n}^N = \sum_{m=-\min(n,M_{\mathrm{rank}})}^{\min(n,M_{\mathrm{rank}})} D_{m_1m}^n(0, -\beta_p, \alpha_p)g_{mn}^N, \tag{18}$$

or in matrix form,

$$\begin{bmatrix} F_{m_1n}^N \\ G_{m_1n}^N \end{bmatrix} = \mathrm{D}^{-1}\begin{bmatrix} f_{mn}^N \\ g_{mn}^N \end{bmatrix}, \quad \mathrm{D}^{-1} = \begin{bmatrix} D_{m_1m}^n(0, -\beta_p, \alpha_p) & 0 \\ 0 & D_{m_1m}^n(0, -\beta_p, \alpha_p) \end{bmatrix}. \tag{19}$$

Note that the upper index N indicates that the expansion coefficients depend on the truncation indices M_{rank} and N_{rank}.

In the half-space $z > 0$, the radiating vector spherical wave functions can be expressed as integrals over upward propagating vector plane waves (cf. Eqs. (A.13)–(A.14))

$$\mathbf{M}_{mn}^3(k_2\mathbf{r}) = \int_0^{2\pi} \int_0^{\pi/2-j\infty} [A_{mn}^{\mathrm{SP}}(\beta,\alpha)\mathbf{M}(\mathbf{r},\mathbf{k}_2^+) + B_{mn}^{\mathrm{SP}}(\beta,\alpha)\mathbf{N}(\mathbf{r},\mathbf{k}_2^+)] \sin\beta\,\mathrm{d}\beta\,\mathrm{d}\alpha,$$
(20)

$$\mathbf{N}_{mn}^3(k_2\mathbf{r}) = \int_0^{2\pi} \int_0^{\pi/2-j\infty} [B_{mn}^{\mathrm{SP}}(\beta,\alpha)\mathbf{M}(\mathbf{r},\mathbf{k}_2^+) + A_{mn}^{\mathrm{SP}}(\beta,\alpha)\mathbf{N}(\mathbf{r},\mathbf{k}_2^+)] \sin\beta\,\mathrm{d}\beta\,\mathrm{d}\alpha,$$
(21)

where $\mathbf{k}_2^+ = (k_2, \beta, \alpha)$, and the amplitudes $A_{mn}^{\mathrm{SP}}(\beta,\alpha)$ and $B_{mn}^{\mathrm{SP}}(\beta,\alpha)$ are given by Eqs. (A.15) and (A.16), respectively. Inserting Eqs. (20)–(21) in Eq. (16), and interchanging the order of summation and integration, gives an integral representation for the scattered field in terms of upward propagating vector plane waves,

$$\mathbf{E}_{2\mathrm{sct}}^N(\mathbf{r}) = \int_0^{2\pi} \int_0^{\pi/2-j\infty} [F^+(\beta,\alpha)\mathbf{M}(\mathbf{r},\mathbf{k}_2^+) + G^+(\beta,\alpha)\mathbf{N}(\mathbf{r},\mathbf{k}_2^+)] \sin\beta\,\mathrm{d}\beta\,\mathrm{d}\alpha,$$
(22)

where

$$F^+(\beta,\alpha) = \sum_{(m,n)=1}^{N} [F_{mn}^N A_{mn}^{\mathrm{SP}}(\beta,\alpha) + G_{mn}^N B_{mn}^{\mathrm{SP}}(\beta,\alpha)],$$
(23)

$$G^+(\beta,\alpha) = \sum_{(m,n)=1}^{N} [F_{mn}^N B_{mn}^{\mathrm{SP}}(\beta,\alpha) + G_{mn}^N A_{mn}^{\mathrm{SP}}(\beta,\alpha)],$$
(24)

are the amplitudes of the vector plane waves. Similarly, in the half-space $z < 0$, we use the integral representations (cf. Eqs. (A.17)–(A.18))

$$\mathbf{M}_{mn}^3(k_2\mathbf{r}) = \int_0^{2\pi} \int_0^{\pi/2-j\infty} [A_{mn}^{\mathrm{SP}}(\pi-\beta,\alpha)\mathbf{M}(\mathbf{r},\mathbf{k}_2^-) + B_{mn}^{\mathrm{SP}}(\pi-\beta,\alpha)\mathbf{N}(\mathbf{r},\mathbf{k}_2^-)] \sin\beta\,\mathrm{d}\beta\,\mathrm{d}\alpha,$$
(25)

$$\mathbf{N}_{mn}^3(k_2\mathbf{r}) = \int_0^{2\pi} \int_0^{\pi/2-j\infty} [B_{mn}^{\mathrm{SP}}(\pi-\beta,\alpha)\mathbf{M}(\mathbf{r},\mathbf{k}_2^-) + A_{mn}^{\mathrm{SP}}(\pi-\beta,\alpha)\mathbf{N}(\mathbf{r},\mathbf{k}_2^-)] \sin\beta\,\mathrm{d}\beta\,\mathrm{d}\alpha,$$
(26)

where $\mathbf{k}_2^- = (k_2, \pi-\beta, \alpha)$, and obtain an integral representation for the scattered field in terms of downward propagating vector plane waves,

$$\mathbf{E}_{2\mathrm{sct}}^N(\mathbf{r}) = \int_0^{2\pi} \int_0^{\pi/2-j\infty} [F^-(\beta,\alpha)\mathbf{M}(\mathbf{r},\mathbf{k}_2^-) + G^-(\beta,\alpha)\mathbf{N}(\mathbf{r},\mathbf{k}_2^-)] \sin\beta\,\mathrm{d}\beta\,\mathrm{d}\alpha,$$
(27)

where

$$F^-(\beta,\alpha) = \sum_{(m,n)=1}^{N} [F_{mn}^N A_{mn}^{\mathrm{SP}}(\pi-\beta,\alpha) + G_{mn}^N B_{mn}^{\mathrm{SP}}(\pi-\beta,\alpha)],$$
(28)

$$G^-(\beta,\alpha) = \sum_{(m,n)=1}^{N} [F_{mn}^N B_{mn}^{\mathrm{SP}}(\pi-\beta,\alpha) + G_{mn}^N A_{mn}^{\mathrm{SP}}(\pi-\beta,\alpha)].$$
(29)

Relying on the analysis presented by Egel et al. [26,27] we make the following comment. Let $z = z_{\max} < R$ be a tangent plane bounding the particle from above. The spherical wave expansion of the scattered field (15) can diverge in the region $z_{\max} \le z < R$. If we would work with the infinite series (15), we would obtain the spectral representation for the scattered field (22), in which the amplitudes $F^+(\beta,\alpha)$ and $G^+(\beta,\alpha)$ would be represented as in Eqs. (23) and (24), respectively, but by infinite instead of finite series. In this case, the spectral representation (22) would not to be valid in a part of the region inside the circumscribed sphere. The reason is due to the change of the order of integration and summation when inserting Eqs. (20)–(21) in Eq. (15). This operation is justified for $z \ge R$, but it is not allowed for $z \to z_{\max}$. In this region, the convergence is not uniform but only point-wise. However, in a practical implementation of the method, the expansion (15) must be truncated, in which case, the order of integration and summation plays no role. For

this reason, we considered from the beginning an approximate scattered field represented by the finite series (16).

2.1.3. The interacting field in the immersion layer (layer 2)

Each vector plane wave in Eqs. (22) and (27), that is, $\mathbf{M}(\mathbf{r},\mathbf{k}_2^+)$, $\mathbf{N}(\mathbf{r},\mathbf{k}_2^+)$, $\mathbf{M}(\mathbf{r},\mathbf{k}_2^-)$, and $\mathbf{N}(\mathbf{r},\mathbf{k}_2^-)$, will interact with the layer system. Because we have two integral representations for the radiating vector spherical wave functions (for $z > 0$ and $z < 0$), we will treat these cases separately.

1. In Appendix B it is shown that for an external excitation represented by the vector plane waves propagating upward in layer 2, $\mathbf{E}_2^+ = \mathbf{M}(\mathbf{r},\mathbf{k}_2^+)$ and $\mathbf{E}_2^+ = \mathbf{N}(\mathbf{r},\mathbf{k}_2^+)$, the reflected upward propagating fields in layer 2 are $\mathbf{E}_{2\mathrm{R}}^+ = S_\perp^{++}\mathbf{M}(\mathbf{r},\mathbf{k}_2^+)$ and $\mathbf{E}_{2\mathrm{R}}^+ = S_\parallel^{++}\mathbf{N}(\mathbf{r},\mathbf{k}_2^+)$, respectively, while the reflected downward propagating fields in layer 2 are $\mathbf{E}_{2\mathrm{R}}^- = S_\perp^{+-}\mathbf{M}(\mathbf{r},\mathbf{k}_2^-)$ and $\mathbf{E}_{2\mathrm{R}}^- = S_\parallel^{+-}\mathbf{N}(\mathbf{r},\mathbf{k}_2^-)$, respectively. The expressions of the scattering coefficients S_{X}^{++} and S_{X}^{+-}, X $= \perp, \parallel$, are given by Eqs. (B.17) and (B.18), respectively. Using this result in Eq. (22), we infer that the interacting field is

$$\mathbf{E}_{\mathrm{int}}^{N+}(\mathbf{r}) = \int_0^{2\pi} \int_0^{\pi/2-j\infty} \{F^+(\beta,\alpha)[S_\perp^{++}\mathbf{M}(\mathbf{r},\mathbf{k}_2^+) + S_\perp^{+-}\mathbf{M}(\mathbf{r},\mathbf{k}_2^-)] + G^+(\beta,\alpha)[S_\parallel^{++}\mathbf{N}(\mathbf{r},\mathbf{k}_2^+) + S_\parallel^{+-}\mathbf{N}(\mathbf{r},\mathbf{k}_2^-)]\} \sin\beta\,\mathrm{d}\beta\,\mathrm{d}\alpha.$$
(30)

2. In Appendix B it is shown that for an external excitation represented by the vector plane waves propagating downward in layer 2, $\mathbf{E}_2^- = \mathbf{M}(\mathbf{r},\mathbf{k}_2^-)$ and $\mathbf{E}_2^- = \mathbf{N}(\mathbf{r},\mathbf{k}_2^-)$, the reflected upward propagating fields in layer 2 are $\mathbf{E}_{2\mathrm{R}}^+ = S_\perp^{-+}\mathbf{M}(\mathbf{r},\mathbf{k}_2^+)$ and $\mathbf{E}_{2\mathrm{R}}^+ = S_\parallel^{-+}\mathbf{N}(\mathbf{r},\mathbf{k}_2^+)$, respectively, while the reflected downward propagating fields in layer 2 are $\mathbf{E}_{2\mathrm{R}}^- = S_\perp^{--}\mathbf{M}(\mathbf{r},\mathbf{k}_2^-)$ and $\mathbf{E}_{2\mathrm{R}}^- = S_\parallel^{--}\mathbf{N}(\mathbf{r},\mathbf{k}_2^-)$, respectively. The expressions of the scattering coefficients S_{X}^{-+} and S_{X}^{--}, X $= \perp, \parallel$, are given by Eqs. (B.20) and (B.21), respectively. Employing this result in Eq. (27), we deduce that the interacting field is

$$\mathbf{E}_{\mathrm{int}}^{N-}(\mathbf{r}) = \int_0^{2\pi} \int_0^{\pi/2-j\infty} \{F^-(\beta,\alpha)[S_\perp^{-+}\mathbf{M}(\mathbf{r},\mathbf{k}_2^+) + S_\perp^{--}\mathbf{M}(\mathbf{r},\mathbf{k}_2^-)] + G^-(\beta,\alpha)[S_\parallel^{-+}\mathbf{N}(\mathbf{r},\mathbf{k}_2^+) + S_\parallel^{--}\mathbf{N}(\mathbf{r},\mathbf{k}_2^-)]\} \sin\beta\,\mathrm{d}\beta\,\mathrm{d}\alpha.$$
(31)

The (total) interacting field produced by the scattered field is then

$$\mathbf{E}_{\mathrm{int}}^N(\mathbf{r}) = \mathbf{E}_{\mathrm{int}}^{N+}(\mathbf{r}) + \mathbf{E}_{\mathrm{int}}^{N-}(\mathbf{r})$$
$$= \int_0^{2\pi} \int_0^{\pi/2-j\infty} [\mathcal{F}^+(\beta,\alpha)\mathbf{M}(\mathbf{r},\mathbf{k}_2^+) + \mathcal{F}^-(\beta,\alpha)\mathbf{M}(\mathbf{r},\mathbf{k}_2^-) + \mathcal{G}^+(\beta,\alpha)\mathbf{N}(\mathbf{r},\mathbf{k}_2^+) + \mathcal{G}^-(\beta,\alpha)\mathbf{N}(\mathbf{r},\mathbf{k}_2^-)] \sin\beta\,\mathrm{d}\beta\,\mathrm{d}\alpha,$$
(32)

where

$$\mathcal{F}^+(\beta,\alpha) = F^+(\beta,\alpha)S_\perp^{++} + F^-(\beta,\alpha)S_\perp^{-+},$$
(33)

$$\mathcal{F}^-(\beta,\alpha) = F^+(\beta,\alpha)S_\perp^{+-} + F^-(\beta,\alpha)S_\perp^{--},$$
(34)

$$\mathcal{G}^+(\beta,\alpha) = G^+(\beta,\alpha)S_\parallel^{++} + G^-(\beta,\alpha)S_\parallel^{-+},$$
(35)

$$\mathcal{G}^-(\beta,\alpha) = G^+(\beta,\alpha)S_\parallel^{+-} + G^-(\beta,\alpha)S_\parallel^{--}.$$
(36)

Inserting the expansions of the upward and downward propagating vector plane waves in terms of regular vector spherical wave functions as given by Eqs. (A.19)–(A.20) and (A.23)–(A.24), respectively, in Eq. (32), we obtain the following series representation for the interacting field:

$$\mathbf{E}_{\mathrm{int}}^N(\mathbf{r}) = \sum_{(m_1,n_1)=1}^{N} [F_{1m_1n_1}^N \mathbf{M}_{m_1n_1}^1(k_2\mathbf{r}) + G_{1m_1n_1}^N \mathbf{N}_{m_1n_1}^1(k_2\mathbf{r})],$$
(37)

where

$$F_{1m_1n_1}^N = \int_0^{2\pi} \int_0^{\pi/2-j\infty} [\mathcal{F}^+(\beta,\alpha)A_{m_1n_1}^{\mathrm{PS}}(\beta,\alpha) + \mathcal{F}^-(\beta,\alpha)A_{m_1n_1}^{\mathrm{PS}}(\pi-\beta,\alpha) + \mathcal{G}^+(\beta,\alpha)B_{m_1n_1}^{\mathrm{PS}}(\beta,\alpha) + \mathcal{G}^-(\beta,\alpha)B_{m_1n_1}^{\mathrm{PS}}(\pi-\beta,\alpha)] \sin\beta\,\mathrm{d}\beta\,\mathrm{d}\alpha,$$
(38)

$$G_{\mathrm{I}m_1n_1}^N = \int_0^{2\pi} \int_0^{\pi/2-\mathrm{j}\infty} [\mathcal{F}^+(\beta,\alpha)B_{m_1n_1}^{\mathrm{PS}}(\beta,\alpha) + \mathcal{F}^-(\beta,\alpha)B_{m_1n_1}^{\mathrm{PS}}(\pi-\beta,\alpha)$$
$$+ \mathcal{G}^+(\beta,\alpha)A_{m_1n_1}^{\mathrm{PS}}(\beta,\alpha) + \mathcal{G}^-(\beta,\alpha)A_{m_1n_1}^{\mathrm{PS}}(\pi-\beta,\alpha)]\sin\beta\mathrm{d}\beta\mathrm{d}\alpha, \quad (39)$$

and $A_{m_1n_1}^{\mathrm{PS}}(\beta,\alpha)$ and $B_{m_1n_1}^{\mathrm{PS}}(\beta,\alpha)$ are given by Eqs. (A.21) and (A.22), respectively. In the particle coordinate systems $Ox_\mathrm{p}y_\mathrm{p}z_\mathrm{p}$, the spherical wave expansion of the interacting field reads as

$$\mathbf{E}_{\mathrm{int}}^N(\mathbf{r}) = \sum_{(m_1,n_1)=1}^N [f_{\mathrm{I}m_1n_1}^N \mathbf{M}_{m_1n_1}^1(k_2r,\theta,\varphi) + g_{\mathrm{I}m_1n_1}^N \mathbf{N}_{m_1n_1}^1(k_2r,\theta,\varphi)], \quad (40)$$

where

$$f_{\mathrm{I}m_1n_1}^N = \sum_{m_2=-\min(n_1,M_{\mathrm{rank}})}^{\min(n_1,M_{\mathrm{rank}})} D_{m_1m_2}^{n_1}(\alpha_\mathrm{p},\beta_\mathrm{p},0)F_{\mathrm{I}m_2n_1}^N,$$

$$g_{\mathrm{I}m_1n_1}^N = \sum_{m_2=-\min(n_1,M_{\mathrm{rank}})}^{\min(n_1,M_{\mathrm{rank}})} D_{m_1m_2}^{n_1}(\alpha_\mathrm{p},\beta_\mathrm{p},0)G_{\mathrm{I}m_2n_1}^N, \quad (41)$$

or in matrix form,

$$\begin{bmatrix} f_{\mathrm{I}m_1n_1}^N \\ g_{\mathrm{I}m_1n_1}^N \end{bmatrix} = \mathrm{D}\begin{bmatrix} F_{\mathrm{I}m_2n_1}^N \\ G_{\mathrm{I}m_2n_1}^N \end{bmatrix}, \quad \mathrm{D} = \begin{bmatrix} D_{m_1m_2}^{n_1}(\alpha_\mathrm{p},\beta_\mathrm{p},0) & 0 \\ 0 & D_{m_1m_2}^{n_1}(\alpha_\mathrm{p},\beta_\mathrm{p},0) \end{bmatrix}.$$
$$(42)$$

2.1.4. The interaction matrix

The interaction matrix relates the expansion coefficients of the interacting field ($f_{\mathrm{I}m_1n_1}^N$ and $g_{\mathrm{I}m_1n_1}^N$) to the expansion coefficients of the scattered field (f_{mn}^N and g_{mn}^N) in the particle coordinate system.

In a first step, we relate the expansion coefficients of the interacting field ($F_{\mathrm{I}m_1n_1}^N$ and $G_{\mathrm{I}m_1n_1}^N$) to the expansion coefficient of the scattered field (F_{mn}^N and G_{mn}^N) in the global coordinate system. For doing this, we note that expansions of the spectral amplitudes $\mathcal{F}^+(\beta,\alpha)$, $\mathcal{F}^-(\beta,\alpha)$, $\mathcal{G}^+(\beta,\alpha)$, and $\mathcal{G}^-(\beta,\alpha)$ in terms of the scattering field coefficients F_{mn}^N and G_{mn}^N can be obtained by combining Eqs. (23), (24), (28), and (29) with Eqs. (33)–(36). The result is

$$\mathcal{F}^+(\beta,\alpha) = \sum_{(m,n)=1}^N (\mathscr{F}_{mn}^{1+}F_{mn}^N + \mathscr{G}_{mn}^{1+}G_{mn}^N), \quad (43)$$

$$\mathcal{F}^-(\beta,\alpha) = \sum_{(m,n)=1}^N (\mathscr{F}_{mn}^{1-}F_{mn}^N + \mathscr{G}_{mn}^{1-}G_{mn}^N), \quad (44)$$

$$\mathcal{G}^+(\beta,\alpha) = \sum_{(m,n)=1}^N (\mathscr{F}_{mn}^{2+}F_{mn}^N + \mathscr{G}_{mn}^{2+}G_{mn}^N), \quad (45)$$

$$\mathcal{G}^-(\beta,\alpha) = \sum_{(m,n)=1}^N (\mathscr{F}_{mn}^{2-}F_{mn}^N + \mathscr{G}_{mn}^{2-}G_{mn}^N), \quad (46)$$

with

$$\mathscr{F}_{mn}^{1+} = S_\perp^{++}A_{mn}^{\mathrm{SP}}(\beta,\alpha) + S_\perp^{-+}A_{mn}^{\mathrm{SP}}(\pi-\beta,\alpha), \quad (47)$$

$$\mathscr{G}_{mn}^{1+} = S_\perp^{++}B_{mn}^{\mathrm{SP}}(\beta,\alpha) + S_\perp^{-+}B_{mn}^{\mathrm{SP}}(\pi-\beta,\alpha), \quad (48)$$

$$\mathscr{F}_{mn}^{1-} = S_\perp^{+-}A_{mn}^{\mathrm{SP}}(\beta,\alpha) + S_\perp^{--}A_{mn}^{\mathrm{SP}}(\pi-\beta,\alpha), \quad (49)$$

$$\mathscr{G}_{mn}^{1-} = S_\perp^{+-}B_{mn}^{\mathrm{SP}}(\beta,\alpha) + S_\perp^{--}B_{mn}^{\mathrm{SP}}(\pi-\beta,\alpha), \quad (50)$$

and

$$\mathscr{F}_{mn}^{2+} = S_\parallel^{++}B_{mn}^{\mathrm{SP}}(\beta,\alpha) + S_\parallel^{-+}B_{mn}^{\mathrm{SP}}(\pi-\beta,\alpha), \quad (51)$$

$$\mathscr{G}_{mn}^{2+} = S_\parallel^{++}A_{mn}^{\mathrm{SP}}(\beta,\alpha) + S_\parallel^{-+}A_{mn}^{\mathrm{SP}}(\pi-\beta,\alpha), \quad (52)$$

$$\mathscr{F}_{mn}^{2-} = S_\parallel^{+-}B_{mn}^{\mathrm{SP}}(\beta,\alpha) + S_\parallel^{--}B_{mn}^{\mathrm{SP}}(\pi-\beta,\alpha), \quad (53)$$

$$\mathscr{G}_{mn}^{2-} = S_\parallel^{+-}A_{mn}^{\mathrm{SP}}(\beta,\alpha) + S_\parallel^{--}A_{mn}^{\mathrm{SP}}(\pi-\beta,\alpha). \quad (54)$$

Then, substituting Eqs. (43)–(46) in Eqs. (38)–(39), yields

$$\begin{bmatrix} F_{\mathrm{I}m_1n_1}^N \\ G_{\mathrm{I}m_1n_1}^N \end{bmatrix} = \mathrm{R}\begin{bmatrix} F_{mn}^N \\ G_{mn}^N \end{bmatrix}, \quad (55)$$

where the elements of the matrix

$$\mathrm{R} = \begin{bmatrix} R_{m_1n_1,mn}^{11} & R_{m_1n_1,mn}^{12} \\ R_{m_1n_1,mn}^{21} & R_{m_1n_1,mn}^{22} \end{bmatrix} \quad (56)$$

are given by

$$R_{m_1n_1,mn}^{11} = \int_0^{2\pi}\int_0^{\pi/2-\mathrm{j}\infty} [\mathscr{F}_{mn}^{1+}A_{m_1n_1}^{\mathrm{PS}}(\beta,\alpha) + \mathscr{F}_{mn}^{1-}A_{m_1n_1}^{\mathrm{PS}}(\pi-\beta,\alpha)$$
$$+ \mathscr{F}_{mn}^{2+}B_{m_1n_1}^{\mathrm{PS}}(\beta,\alpha) + \mathscr{F}_{mn}^{2-}B_{m_1n_1}^{\mathrm{PS}}(\pi-\beta,\alpha)]\sin\beta\mathrm{d}\beta\mathrm{d}\alpha, \quad (57)$$

$$R_{m_1n_1,mn}^{12} = \int_0^{2\pi}\int_0^{\pi/2-\mathrm{j}\infty} [\mathscr{G}_{mn}^{1+}A_{m_1n_1}^{\mathrm{PS}}(\beta,\alpha) + \mathscr{G}_{mn}^{1-}A_{m_1n_1}^{\mathrm{PS}}(\pi-\beta,\alpha)$$
$$+ \mathscr{G}_{mn}^{2+}B_{m_1n_1}^{\mathrm{PS}}(\beta,\alpha) + \mathscr{G}_{mn}^{2-}B_{m_1n_1}^{\mathrm{PS}}(\pi-\beta,\alpha)]\sin\beta\mathrm{d}\beta\mathrm{d}\alpha, \quad (58)$$

$$R_{m_1n_1,mn}^{21} = \int_0^{2\pi}\int_0^{\pi/2-\mathrm{j}\infty} [\mathscr{F}_{mn}^{1+}B_{m_1n_1}^{\mathrm{PS}}(\beta,\alpha) + \mathscr{F}_{mn}^{1-}B_{m_1n_1}^{\mathrm{PS}}(\pi-\beta,\alpha)$$
$$+ \mathscr{F}_{mn}^{2+}A_{m_1n_1}^{\mathrm{PS}}(\beta,\alpha) + \mathscr{F}_{mn}^{2-}A_{m_1n_1}^{\mathrm{PS}}(\pi-\beta,\alpha)]\sin\beta\mathrm{d}\beta\mathrm{d}\alpha, \quad (59)$$

$$R_{m_1n_1,mn}^{22} = \int_0^{2\pi}\int_0^{\pi/2-\mathrm{j}\infty} [\mathscr{G}_{mn}^{1+}B_{m_1n_1}^{\mathrm{PS}}(\beta,\alpha) + \mathscr{G}_{mn}^{1-}B_{m_1n_1}^{\mathrm{PS}}(\pi-\beta,\alpha)+$$
$$+ \mathscr{G}_{mn}^{2+}A_{m_1n_1}^{\mathrm{PS}}(\beta,\alpha) + \mathscr{G}_{mn}^{2-}A_{m_1n_1}^{\mathrm{PS}}(\pi-\beta,\alpha)]\sin\beta\mathrm{d}\beta\mathrm{d}\alpha. \quad (60)$$

The expressions of the matrix elements $R_{m_1n_1,mn}^{ij}$, $i,j = 1,2$ can be simplified by making use of the expressions of $A_{mn}^{\mathrm{SP}}(\beta,\alpha)$, $B_{mn}^{\mathrm{SP}}(\beta,\alpha)$, $A_{m_1n_1}^{\mathrm{PS}}(\beta,\alpha)$ and $B_{m_1n_1}^{\mathrm{PS}}(\beta,\alpha)$ as given by Eqs. (A.15), (A.16), (A.21) and (A.22), respectively, and by integrating over the azimuth angle α; we find

$$R_{m_1n_1n}^{11} = \int_0^{\pi/2-\mathrm{j}\infty} C_{n_1n}\{\widehat{\mathscr{F}}_{m_1n}^{1+}(\beta)\tau_{n_1}^{|m_1|}(\beta) + \widehat{\mathscr{F}}_{m_1n}^{1-}(\beta)\tau_{n_1}^{|m_1|}(\pi-\beta,\alpha)$$
$$+ m_1[\widehat{\mathscr{F}}_{m_1n}^{2+}(\beta)\pi_{n_1}^{|m_1|}(\beta) + \widehat{\mathscr{F}}_{m_1n}^{2-}(\beta)\pi_{n_1}^{|m_1|}(\pi-\beta)]\}\sin\beta\mathrm{d}\beta, \quad (61)$$

$$R_{m_1n_1n}^{12} = \int_0^{\pi/2-\mathrm{j}\infty} C_{n_1n}\{\widehat{\mathscr{G}}_{m_1n}^{1+}(\beta)\tau_{n_1}^{|m_1|}(\beta) + \widehat{\mathscr{G}}_{m_1n}^{1-}(\beta)\tau_{n_1}^{|m_1|}(\pi-\beta,\alpha)$$
$$+ m_1[\widehat{\mathscr{G}}_{m_1n}^{2+}(\beta)\pi_{n_1}^{|m_1|}(\beta) + \widehat{\mathscr{G}}_{m_1n}^{2-}(\beta)\pi_{n_1}^{|m_1|}(\pi-\beta)]\}\sin\beta\mathrm{d}\beta, \quad (62)$$

$$R_{m_1n_1n}^{21} = \int_0^{\pi/2-\mathrm{j}\infty} C_{n_1n}\{m_1[\widehat{\mathscr{F}}_{m_1n}^{1+}(\beta)\pi_{n_1}^{|m_1|}(\beta) + \widehat{\mathscr{F}}_{m_1n}^{1-}(\beta)\pi_{n_1}^{|m_1|}(\pi-\beta)]$$
$$+ \widehat{\mathscr{F}}_{m_1n}^{2+}(\beta)\tau_{n_1}^{|m_1|}(\beta) + \widehat{\mathscr{F}}_{m_1n}^{2-}(\beta)\tau_{n_1}^{|m_1|}(\pi-\beta,\alpha)\}\sin\beta\mathrm{d}\beta, \quad (63)$$

$$R_{m_1n_1n}^{22} = \int_0^{\pi/2-\mathrm{j}\infty} C_{n_1n}\{m_1[\widehat{\mathscr{G}}_{m_1n}^{1+}(\beta)\pi_{n_1}^{|m_1|}(\beta) + \widehat{\mathscr{G}}_{m_1n}^{1-}(\beta)\pi_{n_1}^{|m_1|}(\pi-\beta)]$$
$$+ \widehat{\mathscr{G}}_{m_1n}^{2+}(\beta)\tau_{n_1}^{|m_1|}(\beta) + \widehat{\mathscr{G}}_{m_1n}^{2-}(\beta)\tau_{n_1}^{|m_1|}(\pi-\beta,\alpha)\}\sin\beta\mathrm{d}\beta, \quad (64)$$

where

$$C_{n_1n} = \frac{2\mathrm{j}^{n_1-n}}{\sqrt{nn_1(n+1)(n_1+1)}}, \quad (65)$$

and

$$\widehat{\mathscr{F}}_{m_1n}^{1+}(\beta) = S_\perp^{++}(\beta)\tau_n^{|m_1|}(\beta) + S_\perp^{-+}(\beta)\tau_n^{|m_1|}(\pi-\beta), \quad (66)$$

$$\widehat{\mathscr{G}}_{m_1n}^{1+}(\beta) = m_1[S_\perp^{++}(\beta)\pi_n^{|m_1|}(\beta) + S_\perp^{-+}(\beta)\pi_n^{|m_1|}(\pi-\beta)], \quad (67)$$

$$\widehat{\mathscr{F}}_{m_1n}^{1-}(\beta) = S_\perp^{+-}(\beta)\tau_n^{|m_1|}(\beta) + S_\perp^{--}(\beta)\tau_n^{|m_1|}(\pi-\beta), \quad (68)$$

$$\widehat{\mathscr{G}}_{m_1n}^{1-}(\beta) = m_1[S_\perp^{+-}(\beta)\pi_n^{|m_1|}(\beta) + S_\perp^{--}(\beta)\pi_n^{|m_1|}(\pi-\beta)], \quad (69)$$

$$\widehat{\mathscr{F}}_{m_1n}^{2+}(\beta) = m_1[S_\parallel^{++}(\beta)\pi_n^{|m_1|}(\beta) + S_\parallel^{-+}(\beta)\pi_n^{|m_1|}(\pi-\beta)], \quad (70)$$

$$\widehat{\mathscr{G}}_{m_1n}^{2+}(\beta) = S_\parallel^{++}(\beta)\tau_n^{|m_1|}(\beta) + S_\parallel^{-+}(\beta)\tau_n^{|m_1|}(\pi-\beta), \quad (71)$$

$$\widehat{\mathscr{F}}_{m_1n}^{2-}(\beta) = m_1[S_\parallel^{+-}(\beta)\pi_n^{|m_1|}(\beta) + S_\parallel^{--}\pi_n^{|m_1|}(\pi-\beta)], \quad (72)$$

$$\widehat{\mathscr{G}}_{m_1n}^{2-}(\beta) = S_\parallel^{+-}(\beta)\tau_n^{|m_1|}(\beta) + S_\parallel^{--}(\beta)\tau_n^{|m_1|}(\pi-\beta). \quad (73)$$

In the second step, we derive the expression for the interaction matrix by combining Eqs. (19), (42), and (55); we obtain

$$\begin{bmatrix} f_{\mathrm{I}m_1n_1}^N \\ g_{\mathrm{I}m_1n_1}^N \end{bmatrix} = \mathrm{A}\begin{bmatrix} f_{mn}^N \\ g_{mn}^N \end{bmatrix}, \quad (74)$$

where

$$A = DRD^{-1} = \left[A_{m_1 n_1, mn} \right] = \begin{bmatrix} A^{11}_{m_1 n_1, mn} & A^{12}_{m_1 n_1, mn} \\ A^{21}_{m_1 n_1, mn} & A^{22}_{m_1 n_1, mn} \end{bmatrix} \qquad (75)$$

is the interaction matrix whose elements are given explicitly by

$$A^{11}_{m_1 n_1, mn} = \sum_{m_2=-\min(n_1, M_{\text{rank}})}^{\min(n_1, M_{\text{rank}})} D^{n_1}_{m_1 m_2}(\alpha_{\text{p}}, \beta_{\text{p}}, 0) R^{11}_{m_2 n_1 n} D^{n}_{m_2 m}(0, -\beta_{\text{p}}, \alpha_{\text{p}}), \qquad (76)$$

$$A^{12}_{m_1 n_1, mn} = \sum_{m_2=-\min(n_1, M_{\text{rank}})}^{\min(n_1, M_{\text{rank}})} D^{n_1}_{m_1 m_2}(\alpha_{\text{p}}, \beta_{\text{p}}, 0) R^{12}_{m_2 n_1 n} D^{n}_{m_2 m}(0, -\beta_{\text{p}}, \alpha_{\text{p}}), \qquad (77)$$

$$A^{21}_{m_1 n_1, mn} = \sum_{m_2=-\min(n_1, M_{\text{rank}})}^{\min(n_1, M_{\text{rank}})} D^{n_1}_{m_1 m_2}(\alpha_{\text{p}}, \beta_{\text{p}}, 0) R^{21}_{m_2 n_1 n} D^{n}_{m_2 m}(0, -\beta_{\text{p}}, \alpha_{\text{p}}), \qquad (78)$$

$$A^{22}_{m_1 n_1, mn} = \sum_{m_2=-\min(n_1, M_{\text{rank}})}^{\min(n_1, M_{\text{rank}})} D^{n_1}_{m_1 m_2}(\alpha_{\text{p}}, \beta_{\text{p}}, 0) R^{22}_{m_2 n_1 n} D^{n}_{m_2 m}(0, -\beta_{\text{p}}, \alpha_{\text{p}}), \qquad (79)$$

2.1.5. The T-matrix equation

In the particle coordinate system, the scattered field coefficients are related to the expansion coefficients of the fields exciting the particle through the transition matrix $T = [T_{mn, m_1 n_1}]$. Taking into account that the field exciting the particle sums the contributions of the incident and interacting fields, and truncating the spherical wave expansion of the incident field (10), we find the T-matrix equation:

$$\begin{bmatrix} f^N_{mn} \\ g^N_{mn} \end{bmatrix} = T \left(\begin{bmatrix} a^N_{m_1 n_1} \\ b^N_{m_1 n_1} \end{bmatrix} + \begin{bmatrix} f^N_{Im_1 n_1} \\ g^N_{Im_1 n_1} \end{bmatrix} \right), \qquad (80)$$

and further, by making use of Eq. (74),

$$(I - TA) \begin{bmatrix} f^N_{mn} \\ g^N_{mn} \end{bmatrix} = T \begin{bmatrix} a^N_{m_1 n_1} \\ b^N_{m_1 n_1} \end{bmatrix}. \qquad (81)$$

In the above equations, the matrices are of dimension $2N_{\max} \times 2N_{\max}$, where

$$N_{\max} = N_{\text{rank}} + M_{\text{rank}}(2N_{\text{rank}} - M_{\text{rank}} + 1), \qquad (82)$$

and it is apparent that the transition matrix of the system particle–stratified medium is

$$T_{\text{system}} = (I - TA)^{-1} T = (T^{-1} - A)^{-1}. \qquad (83)$$

The transition matrix can be calculated with any method devoted to this purpose, and in particular, with the null-field method with discrete sources [28]. After solving the T-matrix equation for the scattered field coefficients in the particle coordinate system (f^N_{mn} and g^N_{mn}), the scattered field coefficients in the global coordinate system (F^N_{mn} and G^N_{mn}) are computed by means of Eq. (18) (or Eq. (19)).

2.1.6. The scattered field in half-space 0

We consider the expressions of the scattered field in layer 2 as given by Eq. (22) for $z > 0$ and Eq. (27) for $z < 0$. As before, we distinguish the following situations.

1. In Appendix B it is shown that for an external excitation represented by the vector plane waves propagating upward in layer 2, $\mathbf{E}^+_2 = \mathbf{M}(\mathbf{r}, \mathbf{k}^+_2)$ and $\mathbf{E}^+_2 = \mathbf{N}(\mathbf{r}, \mathbf{k}^+_2)$, the transmitted downward propagating fields in the half-space 0 are $\mathbf{E}^-_{0T} = S^+_\perp \mathbf{M}(\mathbf{r}, \mathbf{k}^-_0)$ and $\mathbf{E}^-_{0T} = S^+_\parallel \mathbf{N}(\mathbf{r}, \mathbf{k}^-_0)$, respectively, where the expression of the scattering coefficient S^+_X, X $=\perp, \parallel$, is given by Eq. (B.19). As a result, and by using Eqs. (23)–(24), we find

$$\mathbf{E}^{N+}_{0sct}(\mathbf{r}) = \sum_{(m,n)=1}^{N} \int_0^{2\pi} \int_0^{\pi/2-j\infty} \{ [A^{SP}_{mn}(\beta, \alpha) S^+_\perp(\beta) \mathbf{M}(\mathbf{r}, \mathbf{k}^-_0)$$
$$+ B^{SP}_{mn}(\beta, \alpha) S^+_\parallel(\beta) \mathbf{N}(\mathbf{r}, \mathbf{k}^-_0)] F^N_{mn}$$
$$+ \int_0^{2\pi} \int_0^{\pi/2-j\infty} [B^{SP}_{mn}(\beta, \alpha) S^+_\perp(\beta) \mathbf{M}(\mathbf{r}, \mathbf{k}^-_0)$$

$$+ A^{SP}_{mn}(\beta, \alpha) S^+_\parallel(\beta) \mathbf{N}(\mathbf{r}, \mathbf{k}^-_0)] G^N_{mn} \} \sin \beta \, d\beta \, d\alpha. \qquad (84)$$

2. In Appendix B it is shown that for an external excitation represented by the vector plane waves propagating upward in layer 2, $\mathbf{E}^-_2 = \mathbf{M}(\mathbf{r}, \mathbf{k}^-_2)$ and $\mathbf{E}^-_2 = \mathbf{N}(\mathbf{r}, \mathbf{k}^-_2)$, the transmitted downward propagating fields in the half-space 0 are $\mathbf{E}^-_{0T} = S^-_\perp \mathbf{M}(\mathbf{r}, \mathbf{k}^-_0)$ and $\mathbf{E}^-_{0T} = S^-_\parallel \mathbf{N}(\mathbf{r}, \mathbf{k}^-_0)$, respectively, where the expression of the scattering coefficient S^-_X, X $=\perp, \parallel$, is given by Eq. (B.22). As a result, and by using Eqs. (28)–(29), we find

$$\mathbf{E}^{N-}_{0sct}(\mathbf{r}) = \sum_{(m,n)=1}^{N} \int_0^{2\pi} \int_0^{\pi/2-j\infty} \{ [A^{SP}_{mn}(\pi - \beta, \alpha) S^-_\perp(\beta) \mathbf{M}(\mathbf{r}, \mathbf{k}^-_0)$$
$$+ B^{SP}_{mn}(\pi - \beta, \alpha) S^-_\parallel(\beta) \mathbf{N}(\mathbf{r}, \mathbf{k}^-_0)] F^N_{mn}$$
$$+ \int_0^{2\pi} \int_0^{\pi/2-j\infty} [B^{SP}_{mn}(\pi - \beta, \alpha) S^-_\perp(\beta) \mathbf{M}(\mathbf{r}, \mathbf{k}^-_0)$$
$$+ A^{SP}_{mn}(\pi - \beta, \alpha) S^-_\parallel(\beta) \mathbf{N}(\mathbf{r}, \mathbf{k}^-_0)] G^N_{mn} \} \sin \beta \, d\beta \, d\alpha. \qquad (85)$$

To compute the integrals in Eqs. (84)–(85) we use the stationary phase method. Specifically, for $\mathbf{r} = (r, \theta_0, \varphi)$ with $\theta_0 > \pi/2$, we use the results Appendix D

$$\int_0^{2\pi} \int_0^{\frac{\pi}{2}-j\infty} g(\beta, \alpha) \widehat{\boldsymbol{\alpha}}(\widehat{\mathbf{k}}^-_0) e^{j\mathbf{k}^-_0 \cdot \mathbf{r}} \sin \beta \, d\beta \, d\alpha \approx -j \frac{2\pi}{k_0 r} g(\beta_{2s}, \varphi) e^{jk_0 r} \widehat{\boldsymbol{\varphi}}(\widehat{\mathbf{r}}), \quad (86)$$

$$\int_0^{2\pi} \int_0^{\frac{\pi}{2}-j\infty} g(\beta, \alpha) \widehat{\boldsymbol{\beta}}(\widehat{\mathbf{k}}^-) e^{j\mathbf{k}^- \cdot \mathbf{r}} \sin \beta \, d\beta \, d\alpha \approx -j \frac{2\pi}{k_0 r} g(\beta_{2s}, \varphi) e^{jk_0 r} \widehat{\boldsymbol{\theta}}(\widehat{\mathbf{r}}), \quad (87)$$

where

$$\beta_{2s} = \arcsin \left(\frac{n_0}{n_2} \sin \theta_0 \right). \qquad (88)$$

Employing the above results in Eqs. (84)–(85) and using the expressions of $A^{SP}_{mn}(\beta, \alpha)$ and $B^{SP}_{mn}(\beta, \alpha)$ as given by Eqs. (A.15) and (A.16), respectively, we find that the far-field pattern $\mathbf{E}^{N\infty}_{0sct}(\theta_0, \varphi)$ of the scattered field in the half-space 0, defined through the relation

$$\mathbf{E}^N_{0sct}(\mathbf{r}) = \mathbf{E}^{N+}_{0sct}(\mathbf{r}) + \mathbf{E}^{N-}_{0sct}(\mathbf{r}) = \frac{e^{jk_0 r}}{r} \mathbf{E}^{N\infty}_{0sct}(\theta_0, \varphi), \qquad (89)$$

is

$$\mathbf{E}^{N\infty}_{0sct}(\theta_0, \varphi) = E^{N\infty}_{0\theta}(\theta_0, \varphi) \widehat{\boldsymbol{\theta}}_0 + E^{N\infty}_{0\varphi}(\theta_0, \varphi) \widehat{\boldsymbol{\varphi}}, \qquad (90)$$

where $\widehat{\boldsymbol{\theta}}_0 = \widehat{\boldsymbol{\theta}}(\widehat{\mathbf{r}})$, $\widehat{\boldsymbol{\varphi}} = \widehat{\boldsymbol{\varphi}}(\widehat{\mathbf{r}})$,

$$E^{N\infty}_{0\theta}(\theta_0, \varphi) = j \frac{1}{k_0} \sum_{(m,n)=1}^{N} C_n \{ m[\pi^{|m|}_n(\beta_{2s}) S^+_\parallel(\beta_{2s}) + \pi^{|m|}_n(\pi - \beta_{2s}) S^-_\parallel(\beta_{2s})] F^N_{mn}$$
$$+ [\tau^{|m|}_n(\beta_{2s}) S^+_\parallel(\beta_{2s}) + \tau^{|m|}_n(\pi - \beta_{2s}) S^-_\parallel(\beta_{2s})] G^N_{mn} \} e^{jm\varphi}, \qquad (91)$$

$$E^{N\infty}_{0\varphi}(\theta_0, \varphi) = -\frac{1}{k_0} \sum_{(m,n)=1}^{N} C_n \{ [\tau^{|m|}_n(\beta_{2s}) S^+_\perp(\beta_{2s}) + \tau^{|m|}_n(\pi - \beta_{2s}) S^-_\perp(\beta_{2s})] F^N_{mn}$$
$$+ m[\pi^{|m|}_n(\beta_{2s}) S^+_\perp(\beta_{2s}) + \pi^{|m|}_n(\pi - \beta_{2s}) S^-_\perp(\beta_{2s})] G^N_{mn} \} e^{jm\varphi}, \qquad (92)$$

and

$$C_n = \frac{1}{j^{n+1}} \frac{1}{\sqrt{2n(n+1)}}. \qquad (93)$$

The main steps of the algorithm for computing the expansion coefficients of the scattered field are illustrated in Fig. 3. Some remarks can be made here.

1. For a numerical computation of the integrals in Eqs. (61)–(64), we set $S^{uv}_X = e^{2jk^{(2)}_z z_3} \widehat{S}^{uv}_X$ for $u, v = +, -$ and X $=\perp, \parallel$, in Eqs. (66)–(73), where the expressions of $\widehat{S}^{uv}_X$ are given by Eqs. (B.27)–(B.30). Consequently, each integrand in Eqs. (61)–(64) will contain the factor

$$e^{2jk^{(2)}_z z_3} = e^{2jk_2 z_3 \cos \beta},$$

and so, the integrals in Eqs. (61)–(64) will be of the form

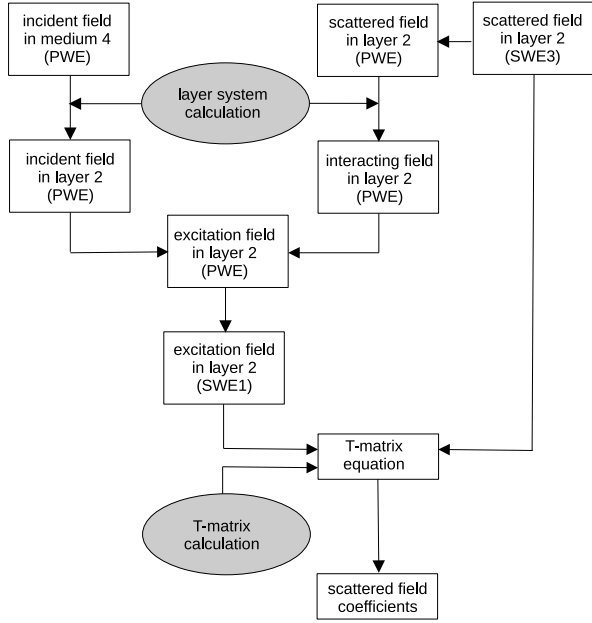$$I = \int_0^{\pi/2-j\infty} f(\cos \beta) e^{jq \cos \beta} \sin \beta \, d\beta, \qquad (94)$$

Fig. 3. Algorithm for computing the expansion coefficients of the scattered field. Here, PWE stands for plane wave expansion, SWF1 for regular spherical wave expansion, and SWF3 for radiating spherical wave expansion.

where $f(t)$ is a relatively slowly varying function and $q = 2k_2 z_3$. The standard path of integration C for β is the union of the lines $L_1 = \{(\mathrm{Re}(\beta), \mathrm{Im}(\beta)) \mid 0 \le \mathrm{Re}(\beta) \le \pi/2, \mathrm{Im}(\beta) = 0\}$ and $L_2 = \{(\mathrm{Re}(\beta), \mathrm{Im}(\beta)) \mid \mathrm{Re}(\beta) = \pi/2, -\infty < \mathrm{Im}(\beta) \le 0\}$. By the change of variable $k_\perp = k_2 \sin \beta$, the integral (94) becomes a Sommerfeld-type integral,

$$I = \int_0^\infty f\left(\frac{k_z^{(2)}}{k_2}\right) e^{jq(k_z^{(2)}/k_2)} \frac{k_\perp dk_\perp}{k_2 k_z^{(2)}}, \qquad (95)$$

where $k_z^{(2)} = \sqrt{k_2^2 - k_\perp^2}$. The computation of the integral (95) along the real axis is not a trivial task. This is because, in the neighborhood of the wave-guide mode singularities and the branch-point singularity (at $k_\perp = k_2$), the integrand is a rapidly varying function of $k_\perp$, and so, a fine sampling of the integrand would be required to achieve a good enough accuracy. A straightforward and robust approach for computing the integral (95) along the segment $[0, k_{\perp \max}]$ was proposed in Refs. [24,29]. It is a direct numerical quadrature (e.g., using the trapezoidal rule) in combination with an integration contour C_1 deflected into the negative complex half-plane [30]. Because the wave-guide mode singularities and the branch-point singularity associated with the square root are located in the positive complex half-plane [24,29], the integrand is an analytic function in the negative complex half-plane. Therefore, according to Cauchy's theorem, the integral along the deflected contour C_1 is identical to the integral along the real axis, but the numerical instabilities are avoided. On the other hand, Bobbert and Vlieger [31,32] considered the change of variable $x = -jq(\cos \beta - 1)$, yielding

$$I = \frac{e^{jq}}{jq} \int_0^\infty f\left(1 - \frac{x}{jq}\right) e^{-x} \, dx, \qquad (96)$$

and used a Gauss–Laguerre quadrature for an efficient calculation of this integral. It should be pointed out that by the above change of variable, the contour of integration is not $C = L_1 \cup L_2$, but rather a contour C_2 that starts at the point $(0,0)$ (for $x = 0$) and goes to the point at infinity ($\mathrm{Re}(\beta) \to \pi/2, \mathrm{Im}(\beta) \to -\infty$) (for

$x \to \infty$), without passing through the critical point $(\pi/2, 0)$. The standard integration contour C together with the two deflected integration contours C_1 and C_2 are shown in Fig. 4. As an example, we illustrate in Fig. 5, the integrands of Eqs. (95) and (96) for computing the matrix element $I = R_{m_1 n_1 n}^{11}$. The plots show that in the first case and in the neighborhood of the critical point $\kappa = 1$, the integrand is a rapidly varying function of $\kappa = k_\perp/k_2 = \sin \beta$, while in the second case, the integrand is a smooth function of $x = -jq(\cos \beta - 1)$. Actually, in the second case, we have $\kappa = \sin \beta = \sqrt{(x/q)^2 - 2j(x/q)}$, showing that $\mathrm{Im}(\kappa) < 0$; thus, the contour C_2 avoids the vicinity of the singularities. For this reason, the deflected integration contour C_2 was adopted in our analysis.

2. The convergence of the algorithm depends on the choice of the maximum expansion and azimuthal orders N_{rank} and M_{rank}, respectively, as well as, on the number of Laguerre quadrature points N_{int}. In practice, we may check the convergence of the differential scattering cross sections for parallel and perpendicular polarizations $\sigma_\parallel(\theta_0)$ and $\sigma_\perp(\theta_0)$, respectively, at 11 equidistant values of the scattering angle θ_0 in the range $[90°, 270°]$ for the pairs $(N_{\mathrm{rank}}, M_{\mathrm{rank}})$, $(N_{\mathrm{rank}} - 1, M_{\mathrm{rank}})$, and $(N_{\mathrm{rank}}, M_{\mathrm{rank}} - 1)$ [33]. Note that for a prolate spheroid with semi-major axis a, $\sigma_\parallel(\theta_0)$ and $\sigma_\perp(\theta_0)$ are defined, respectively by

$$\sigma_\parallel(\theta_0) = \frac{|E_{0\theta}^{N\infty}(\theta_0, \varphi = 0)|^2}{\pi a^2}, \quad \sigma_\perp(\theta_0) = \frac{|E_{0\varphi}^{N\infty}(\theta_0, \varphi = 0)|^2}{\pi a^2}. \qquad (97)$$

Alternatively, we may check the convergence of the integral response of the detector (defined below) for the same pairs of expansion and azimuthal orders.

3. The system T matrix was obtained by truncating the scattered field expansion and by considering an expansion of the dyadic Green's function in terms of vector spherical wave functions. The derivation relying on a truncation of the internal field and an expansion of the dyadic Green's function in terms vector plane waves is given in Appendix C. Note that the spherical wave expansion is valid outside a sphere enclosing the particle, i.e., for $z \ge R$, while the plane wave expansion is valid outside the tangent planes bounding the particle from above and below, i.e., for $z \ge z_{\max}$ and $z \le z_{\min}$, respectively. In both cases we obtained the same result (cf. Eqs. (83) and (C.43)). Therefore, we may conclude that for truncated field expansions, the condition $z_3 \ge R$ does not play a role.

Two simplified scattering problems can be modeled by particularizing the above formalism.

1. The scattering by a particle placed in the lower half-space and being illuminated by an incident field propagating in the upper half-space (Fig. 2). This problem can be modeled by setting $n_0 = n_1 = n_2$ and $n_3 = n_4$. In such a case, the expressions of the scattering coefficients are given by Eqs. (B.31)–(B.37) of Appendix B, and the entire mathematical formalism reduces to the one presented in Ref. [19].
2. The scattering by a particle placed in the lower half-space and being illuminated by an incident field propagating from the glass prism to the lower half-space through the coating layer (Fig. 2). This problem can be modeled by setting $n_0 = n_1 = n_2$ and $n_3 \neq n_4$. In such a case, the expressions of the scattering coefficients are given by Eqs. (B.39)–(B.42) of Appendix B. The scattering problem is considerably simplified in the sense that it does not take into account the presence of the immersion cell. (cf. Fig. 1).

2.2. Imagining of the scattered field

The imaging system of the scattered field is illustrated in Fig. 6. It consists of a pair of lenses which are placed such that their foci
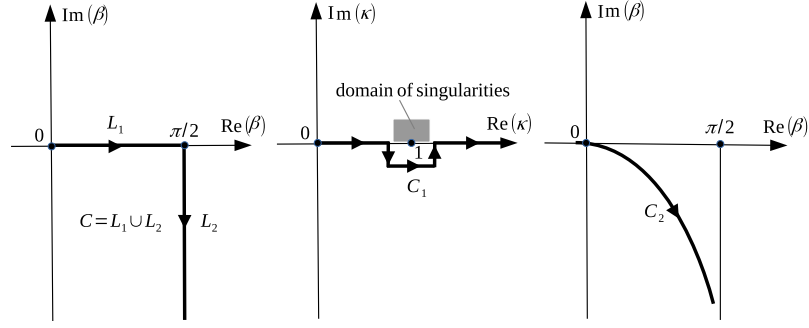
Fig. 4. Standard β-integration contour C (left), deflected κ-integration contour C_1 proposed in Refs. [24,29], where $\kappa = k_\perp/k_2 = \sin\beta$ (middle), and the deflected β-integration contour C_2 proposed in Refs. [31,32] (right).
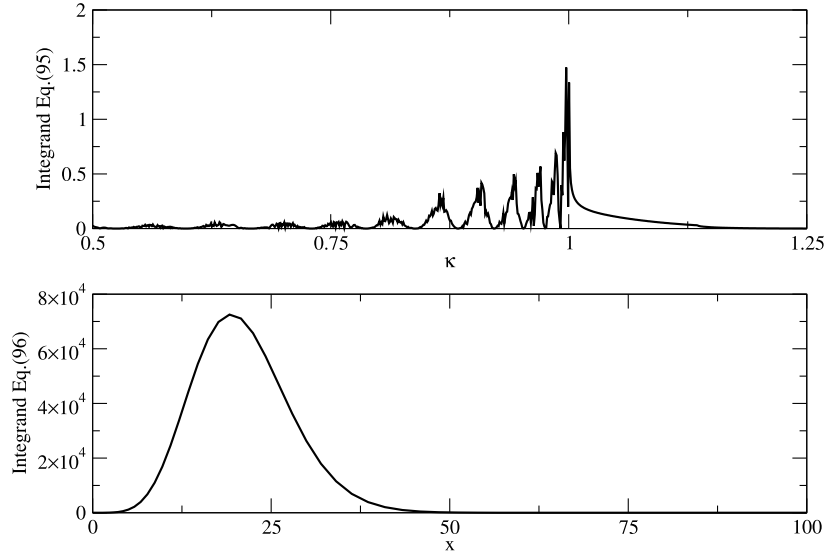

Fig. 5. The integrand of Eq. (95) as a function of $\kappa = k_\perp/k_2$ (upper panel) and the integrand of Eq. (96) as a function of x (lower panel) for computing the matrix element $I = R^{11}_{m_1 n_1 n}$. In the first case, we considered 3000 equidistant quadrature points in the interval $[0, k_{\perp\max}]$ with $k_{\perp\max} = 3k_2$, while in the second case, we considered 80 Laguerre quadrature points. The simulations correspond to $m_1 = 1$, $n_1 = n = N_{\text{rank}} = 35$, and $\text{n}_0 = 1.0003$, $\text{n}_1 = 1.515$, $\text{n}_2 = 1.33$, $\text{n}_3 = 1.42$, and $\text{n}_4 = 1.515$.

coincide, for both illumination and image formation. The particle is placed in the front focal plane of the first lens with the focal distance f_o, and the corresponding image field is formed in the back focal plane of the second lens with the focal distance f_i. The image space is assumed to be a medium with absolute refractive index n_i and wavenumber $k_i = \text{n}_i k$. The aperture angle in the object space (the polar angle under which the Gaussian reference sphere is observed at the focus of the collector lens) is

$$\Theta_o = \arcsin(\text{NA}_o/\text{n}_o),$$

where NA_o is the numerical aperture of the collector lens, the aperture angle in the image space is computed as

$$\Theta_i = \arctan\left(\frac{f_o}{f_i}\tan\Theta_o\right),$$

and the numerical aperture of the detector lens is $\text{NA}_i = \text{n}_i \sin\Theta_i$. In Fig. 6, $A_i B_i$ is the image of the object AB through the optical system, and the coordinate system $O_i x_i y_i$ is the image of the coordinate system Oxy. The right-hand side coordinate system $O_i XYZ$, centered at the focal point of the detector lens, was chosen in order to compute the focus field by means of the Debye diffraction integral. This coordinate system has the positive Y and Z axes in the opposite direction to the positive y_i and z_i axes, respectively. To calculate the image of the scattered field we compute (i) the scattered field on the Gaussian reference sphere of the collector lens, (ii) the transmitted field on the Gaussian reference sphere of the detector lens, and (iii) the focus

field by means of the Debye diffraction integral. The image is then processed in order to extract some useful information about the particle orientation angles. These computational steps are summarized below.

1. The Gaussian reference sphere of the collector lens is a sphere of radius f_o centered at the focal point. In view of Eq. (89), the scattered field on this sphere is given by

$$\mathbf{E}^N_{0\text{sct}}(\theta_0, \varphi) = \frac{e^{jk_0 f_o}}{f_0}\mathbf{E}^{N\infty}_{0\text{sct}}(\theta_0, \varphi). \tag{98}$$

An important scattering characteristics is the integral response of the detector. This is defined as the integral of the Poynting vector over the lower Gaussian hemi-sphere and is computed as

$$P = \int_0^{2\pi}\int_{\Theta_o}^{\pi}[|E^{N\infty}_{0\theta}(\theta_0, \varphi)|^2 + |E^{N\infty}_{0\varphi}(\theta_0, \varphi)|^2]\sin\theta_0 d\theta_0 d\varphi. \tag{99}$$

2. To determine the transmitted field in the image space, we assume that a ray propagating in the object space in the direction (θ_0, φ) is deflected into a ray that propagates in the image space in the direction (θ_i, φ_i); the polar angles in the image space are computed as

$$\theta_i = \arctan[(f_o/f_i)\tan(\theta_0 - \pi)], \tag{100}$$

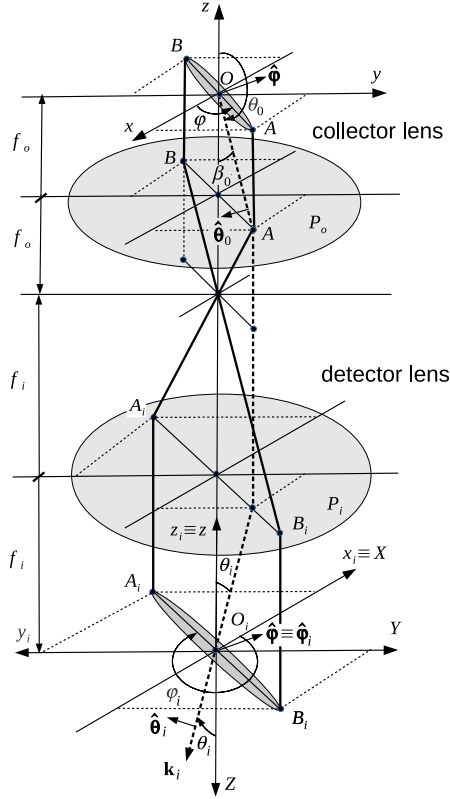$$\varphi_i = 2\pi - \varphi. \tag{101}$$

Fig. 6. The imagining system of the scattered field is represented by the two sections of the Gaussian reference spheres of the collector and detector lens, P_o and P_i, respectively. $A_\mathrm{i}B_\mathrm{i}$ is the image of the object AB and the coordinate system $O_\mathrm{i}x_\mathrm{i}y_\mathrm{i}$ is the image of the coordinate system Oxy. The right-hand side coordinate system $O_\mathrm{i}XYZ$ has the positive Y and Z axes in the opposite direction to the positive y_i and z_i axes, respectively.

Similarly, the polar unit vectors $\hat{\theta}_0$ and $\hat{\varphi}$ are deflected into the polar unit vectors $\hat{\theta}_i$ and $\hat{\varphi}_i$, for which we have the computational formulas

$$\hat{\theta}_\mathrm{i} = \cos\theta_\mathrm{i}\cos\varphi_\mathrm{i}\hat{\mathbf{X}} + \cos\theta_\mathrm{i}\sin\varphi_\mathrm{i}\hat{\mathbf{Y}} - \sin\theta_\mathrm{i}\hat{\mathbf{Z}}, \tag{102}$$

$$\hat{\varphi}_\mathrm{i} = \hat{\varphi} = -\sin\varphi_\mathrm{i}\hat{\mathbf{X}} + \cos\varphi_\mathrm{i}\hat{\mathbf{Y}}, \tag{103}$$

where $(\hat{\mathbf{X}}, \hat{\mathbf{Y}}, \hat{\mathbf{Z}})$ are the Cartesian unit vectors in the coordinate system $O_\mathrm{i}XYZ$. The Gaussian reference sphere of the detector lens is a sphere of radius f_i centered at the focal point. The transmitted field on this sphere is

$$\mathbf{E}_\mathrm{i}^N(\theta_\mathrm{i}, \varphi_\mathrm{i}) = \frac{\mathrm{e}^{\mathrm{j}k_\mathrm{i}f_\mathrm{i}}}{f_\mathrm{i}}[T_\theta E_{0\theta}^{N\infty}(\theta_\mathrm{i}, \varphi_\mathrm{i})\hat{\theta}_\mathrm{i} + T_\varphi E_{0\varphi}^{N\infty}(\theta_\mathrm{i}, \varphi_\mathrm{i})\hat{\varphi}_\mathrm{i}], \tag{104}$$

where

$$E_{0\theta}^{N\infty}(\theta_\mathrm{i}, \varphi_\mathrm{i}) = E_{0\theta}^{N\infty}(\theta_0(\theta_\mathrm{i}), \varphi(\varphi_\mathrm{i})) \text{ and } E_{0\varphi}^{N\infty}(\theta_\mathrm{i}, \varphi_\mathrm{i}) = E_{0\varphi}^{N\infty}(\theta_0(\theta_\mathrm{i}), \varphi(\varphi_\mathrm{i})) \tag{105}$$

with $\theta_0(\theta_\mathrm{i}) = \pi - \arctan[(f_\mathrm{i}/f_0)\tan\theta_\mathrm{i}]$ and $\varphi = 2\pi - \varphi_\mathrm{i}$. The quantities $T_\theta = T_\theta(\theta_\mathrm{i}, \varphi_\mathrm{i})$ and $T_\varphi = T_\varphi(\theta_\mathrm{i}, \varphi_\mathrm{i})$ in Eq. (104) are the transmission coefficients of the imagining system for parallel and perpendicular polarization, respectively. These parameters, which are input parameters of the algorithm, take into account accumulated phase distortions (aberrations at the principal plane of the detector lens) and attenuations (amplitude factors).

3. The computation of the focus field by means of the Debye diffraction integral was outlined in Doicu et al. [19] by following the results established in Leutenegger et al. [34]. Essentially, the

electric field $\mathbf{E}$ at a point (X, Y, Z) is calculated as

$$\mathbf{E}(X, Y, Z) = -\mathrm{j}\frac{f_\mathrm{i}}{\lambda}\int_0^{2\pi}$$
$$\times \int_0^{\Theta_\mathrm{i}} \mathbf{E}_\mathrm{i}^N(\theta_\mathrm{i}, \varphi_\mathrm{i})\mathrm{e}^{\mathrm{j}(k_\mathrm{iX}X + k_\mathrm{iY}Y + k_\mathrm{iZ}Z)}\sin\theta_\mathrm{i}\mathrm{d}\theta_\mathrm{i}\mathrm{d}\varphi_\mathrm{i} \tag{106}$$

$$= -\mathrm{j}\frac{f_\mathrm{i}}{\lambda k_\mathrm{i}^2}\int_{D_\mathrm{k}}\frac{\mathbf{E}_\mathrm{i}^N(\theta_\mathrm{i}, \varphi_\mathrm{i})}{\cos\theta_\mathrm{i}}\mathrm{e}^{\mathrm{j}k_\mathrm{i}Z\cos\theta_\mathrm{i}}\mathrm{e}^{\mathrm{j}(k_\mathrm{iX}X + k_\mathrm{iY}Y)}\mathrm{d}k_\mathrm{iX}\mathrm{d}k_\mathrm{iY}, \tag{107}$$

where Θ_i is the aperture angle of the detector lens. In the last equation above, we used the relations $k_\mathrm{iX} = k_\mathrm{i}\sin\theta_\mathrm{i}\cos\varphi_\mathrm{i}$, $k_\mathrm{iY} = k_\mathrm{i}\sin\theta_\mathrm{i}\sin\varphi_\mathrm{i}$, and $k_\mathrm{iZ} = k_\mathrm{i}\cos\theta_\mathrm{i}$, and defined the domain D_k as

$$D_\mathrm{k} = \{(k_\mathrm{iX}, k_\mathrm{iY}) \mid \sqrt{k_\mathrm{iX}^2 + k_\mathrm{iY}^2} \leq K\}, \tag{108}$$

where $K = k_\mathrm{i}\sin\Theta_\mathrm{i} = k\,\mathrm{NA_i}$. Assuming M sampling points over K, and considering an equidistant sampling $k_\mathrm{iX} = m\Delta K$ and $k_\mathrm{iY} = n\Delta K$, where $\Delta K = K/M$ and $m, n = -M, \ldots, M$, we find that the sampling polar angles are

$$\theta_{imn} = \arcsin\left(\frac{\Delta K}{k_\mathrm{i}}\sqrt{m^2 + n^2}\right), \tag{109}$$

$$\varphi_{imn} = \arccos\left(\frac{m}{\sqrt{m^2 + n^2}}\right). \tag{110}$$

As a result, the numerical implementation of the integral (107) is

$$\mathbf{E}(X, Y, Z) = -\mathrm{j}\frac{f_\mathrm{i}\Delta K^2}{\lambda k_\mathrm{i}^2}\sum_{m=-M}^{M}\sum_{n=-M}^{M}\frac{\mathbf{E}_\mathrm{i}^N(\theta_{imn}, \varphi_{imn})}{\cos\theta_{imn}}\mathrm{e}^{\mathrm{j}k_\mathrm{i}Z\cos\theta_{imn}}\mathrm{e}^{\mathrm{j}\Delta K(mX + nY)}, \tag{111}$$

with the convention

$$\mathbf{E}_\mathrm{i}^N(\theta_{imn}, \varphi_{imn}) = 0 \text{ for } \sqrt{m^2 + n^2} > M.$$

The double sum in Eq. (111) is computed by means of a fast Fourier transform (FFT) by choosing the number of FFT sampling points per transformed dimension as $N = 2^s \geq 4M$. To ensure this condition, the aperture matrix is enlarged by zero padding before performing the Fourier transform, while a cropping of the transform output eliminates the padding. The algorithm is summarized below.

(a) in the axial plane Z, compute the aperture matrix

$$\mathbf{E}_{\mathrm{A}m_1n_1}(Z) = -\mathrm{j}\frac{f_\mathrm{i}\Delta K^2}{\lambda k_\mathrm{i}^2}\frac{\mathbf{E}_\mathrm{i}^N(\theta_{im_1-M,n_1-M}, \varphi_{im_1-M,n_1-M})}{\cos\theta_{im_1-M,n_1-M}}\mathrm{e}^{\mathrm{j}k_\mathrm{i}Z\cos\theta_{im_1-M,n_1-M}}, \tag{112}$$

for $m_1, n_1 = 0, \ldots, N-1$, with the convention

$$\mathbf{E}_{\mathrm{A}m_1n_1}(Z) = 0 \text{ for } \sqrt{(m_1 - M)^2 + (n_1 - M)^2} > M; \tag{113}$$

(b) compute the Fourier transform of the aperture matrix,

$$\mathbf{E}_{\mathrm{F}m_1n_1}(Z) = \mathcal{F}(\mathbf{E}_{\mathrm{A}m_1n_1}(Z)); \tag{114}$$

(c) at the sampling points $X_{m_2} = m_2\Delta X$ and $Y_{n_2} = n_2\Delta Y$, where $\Delta X = \Delta Y = 2\pi/(N\Delta K)$, compute the focus field $\mathbf{E}$ as

$$\mathbf{E}(X_{m_2}, Y_{n_2}, Z) = \mathbf{E}_{\mathrm{F}m_2+N/2-1,n_2+N/2-1}(Z), \tag{115}$$

for $m_2, n_2 = -N/2 + 1, \ldots, N/2$;

(d) for $N_\mathrm{c} < N$, cut the matrix $\mathbf{E}(X_{m_2}, Y_{n_2}, Z)$ outside the range $m_2, n_2 = -N_\mathrm{c}/2 + 1, \ldots, N_\mathrm{c}/2$;
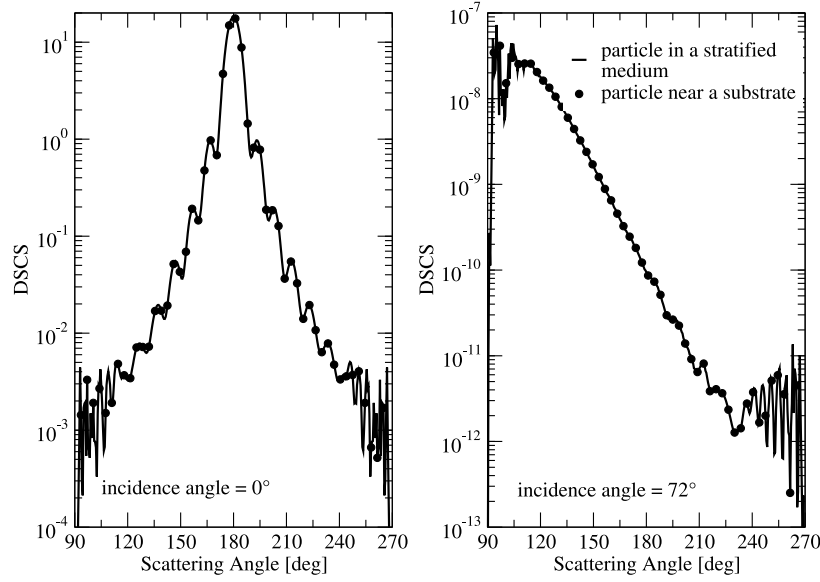
Fig. 7. Differential scattering cross sections for (i) a particle in a stratified medium with $n_0 = n_1 = n_2 = 1.33$ and $n_3 = n_4 = 1.515$, and (ii) a particle near a substrate. The incidence angles are $\beta_{\text{inc}} = 0°$ (left) and $\beta_{\text{inc}} = 72°$ (right). The results correspond to parallel polarization and a particle azimuthal orientation angle $\alpha_p = 45°$.

(e) compute the intensity at the sampling points $X_{m_2} = m_2 \Delta X$ and $Y_{n_2} = n_2 \Delta Y$ as

$$I_{m_2 n_2}(Z) = |E_X(X_{m_2}, Y_{n_2}, Z)|^2 + |E_Y(X_{m_2}, Y_{n_2}, Z)|^2 + |E_Z(X_{m_2}, Y_{n_2}, Z)|^2, \quad (116)$$

for $m_2, n_2 = -N_c/2 + 1, \ldots, N_c/2$;

(f) for a better interpretation of the information related to the particle orientation, the image is transformed into a binary image, the outer contour is extracted, and an ellipse is fitted to the data (by least squares fitting).

3. Numerical simulations

In our numerical simulations we choose the wavelength in vacuum $\lambda = 0.635\,\mu\text{m}$, and the refractive indices of the layers as $n_0 = 1.0003$ (air), $n_1 = 1.515$ (glass), $n_2 = 1.33$ (water), $n_3 = 1.42$ (poly(L-lysine)-poly(ethylene glycol), PLL-PEG [35]), and $n_4 = 1.515$ (glass). The thicknesses of the coating layer, immersion cell, and glass slide are chosen as $d_{\text{coating}} = 0.02\,\mu\text{m}$, $d_{\text{cell}} = 2.0 \times 10^3\,\mu\text{m}$, and $d_{\text{glass}} = 1.0 \times 10^3\,\mu\text{m}$, respectively. If not stated otherwise, the separation distance between the particle and the coating layer is $z_3 = 2.4\,\mu\text{m}$. The other distances to the different interfaces are computed with the formulas $z_0 = -(d_{\text{cell}} + d_{\text{glass}}) + z_3$, $z_1 = -d_{\text{cell}} + z_3$, and $z_4 = z_3 + d_{\text{coating}}$. The particle is a prolate spheroid with semi-major axis $a = 2.0\,\mu\text{m}$, semi-minor axis $b = 1.0\,\mu\text{m}$, refractive index $n_p = 1.591$, and zenith orientation angle $\beta_p = 90°$. The polarization angle of the incident wave is $\alpha_{\text{pol}} = 45°$. The refractive index in the image space is $n_i = 1.0003$ (air), the transversal magnification $M_T = f_i/f_o = 60$, and the numerical aperture in the object space $NA_o = 1.0$. In the simulations, the number of Laguerre quadrature points is $N_{\text{int}} = 80$, and for $z_3 = 2.4\,\mu\text{m}$, the maximum expansion and azimuthal orders are $N_{\text{rank}} = 35$ and $M_{\text{rank}} = 30$, respectively. The critical angle required to achieve total internal reflection in a glass–water interface ($n_4 = 1.515$ and $n_2 = 1.33$) is $\beta_{\text{crit}} = 61°$. Accordingly, the cases of a bright-field ($\beta_{\text{inc}} = 0°$) and an evanescent wave ($\beta_{\text{inc}} > \beta_{\text{crit}}$) illuminations will be considered in the following.

3.1. Model analysis

In a first test we check the accuracy of the newly developed code. For this purpose we take the results corresponding to the scattering by a particle placed in the lower half-space and being illuminated by an incident field propagating in the upper half-space (i.e., $n_0 = n_1 = n_2$ and $n_3 = n_4$) as a Ref. [19]. The results illustrated in Fig. 7 show a complete agreement between the scattering curves.

In a second test we check the accuracy of the simplified model corresponding to the scattering by a particle placed in the lower half-space and being illuminated by an incident field propagating from the glass prism to the lower half-space through the coating layer (i.e., $n_0 = n_1 = n_2$ and $n_3 \neq n_4$). The results illustrated in Fig. 8 show that there is a disagreement between the scattering curves, and so, between the integral responses of the detector. In the case of evanescent wave scattering, the integral response is reduced by about 50%.

The immersion layer and the lower glass slide have a thickness in the millimeter scale, and we can think to model such thick layers incoherently, i.e., in terms of intensity transmission instead of (complex) amplitude transmission. Incoherent scattering can be simulated by assuming the above simplified stratified medium with $n_0 = n_1 = n_2$, and $n_3 \neq n_4$, and by taking into account the transmission between the layers 2 and 0. In particular, referring to Eqs. (89)–(92), we set

$$\mathbf{E}_{0\text{sct}}^{N\pm}(\mathbf{r}) = \frac{e^{jk_0 r}}{r} \mathbf{E}_{0\text{sct}}^{N\pm\infty}(\theta_0, \varphi), \quad (117)$$

$$\mathbf{E}_{0\text{sct}}^{N\pm\infty}(\theta_0, \varphi) = E_{0\theta}^{N\pm\infty}(\theta_0, \varphi)\hat{\boldsymbol{\theta}}_0 + E_{0\varphi}^{N\pm\infty}(\theta_0, \varphi)\hat{\boldsymbol{\varphi}}, \quad (118)$$

where $E_{0\theta}^{N+\infty}$ is as in Eq. (91) but contains only the terms depending on $S_\parallel^+(\beta_{2s})$, $E_{0\theta}^{N-\infty}$ is as in Eq. (91) but contains only the terms depending on $S_\parallel^-(\beta_{2s})$, while $E_{0\varphi}^{N+\infty}$ and $E_{0\varphi}^{N-\infty}$ are defined in a similar manner from Eq. (92). The differential scattering cross sections and the integral response of the detector are then computed as

$$\sigma_\parallel(\theta_0) = \frac{|T_{02\parallel} E_{0\theta}^{N+\infty}(\theta_0, \varphi = 0)|^2 + |T_{02\parallel} E_{0\theta}^{N-\infty}(\theta_0, \varphi = 0)|^2}{\pi a^2}, \quad (119)$$

$$\sigma_\perp(\theta_0) = \frac{|T_{02\perp} E_{0\varphi}^{N+\infty}(\theta_0, \varphi = 0)|^2 + |T_{02\perp} E_{0\varphi}^{N-\infty}(\theta_0, \varphi = 0)|^2}{\pi a^2}, \quad (120)$$

and

$$P = \int_0^{2\pi} \int_{\Theta_o}^{\pi} [|T_{02\parallel} E_{0\theta}^{N+\infty}(\theta_0, \varphi)|^2 + |T_{02\parallel} E_{0\theta}^{N-\infty}(\theta_0, \varphi)|^2$$

$$+ |T_{02\perp} E_{0\varphi}^{N+\infty}(\theta_0, \varphi)|^2 + |T_{02\perp} E_{0\varphi}^{N-\infty}(\theta_0, \varphi)|^2] \sin\theta_0 \, d\theta_0 \, d\varphi, \quad (121)$$

respectively, where (cf. Eqs. (B.4) and (B.5)) $T_{02X} = T_{01X} T_{12X}$, $X = \perp, \parallel$, is the transmission between the layers 2 and 0. In Fig. 9 we show the
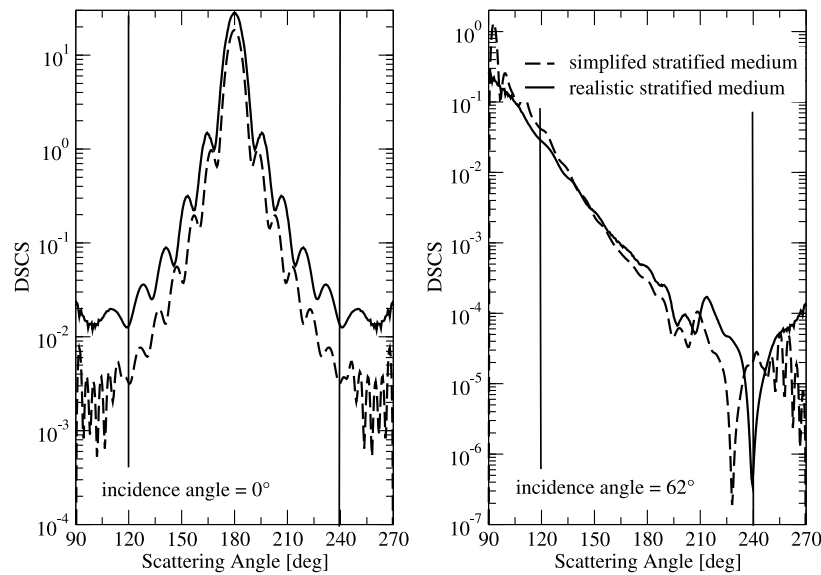
Fig. 8. Differential scattering cross sections for a particle placed in (i) a simplified stratified medium with $n_0 = n_1 = n_2 = 1.33$, $n_3 = 1.42$, and $n_4 = 1.515$, and (ii) a realistic stratified medium with $n_0 = 1.0003$, $n_1 = 1.515$, $n_2 = 1.33$, $n_3 = 1.42$, and $n_4 = 1.515$. The incidence angles are $\beta_{inc} = 0°$ (left) and $\beta_{inc} = 62°$ (right). The results correspond to parallel polarization and a particle azimuthal orientation angle $\alpha_p = 45°$. The aperture angle in the object space is $\Theta_o = 60°$, and the vertical lines at $180° - \Theta_o$ and $180° + \Theta_o$ define the angular scattering domain analyzed by the detector.
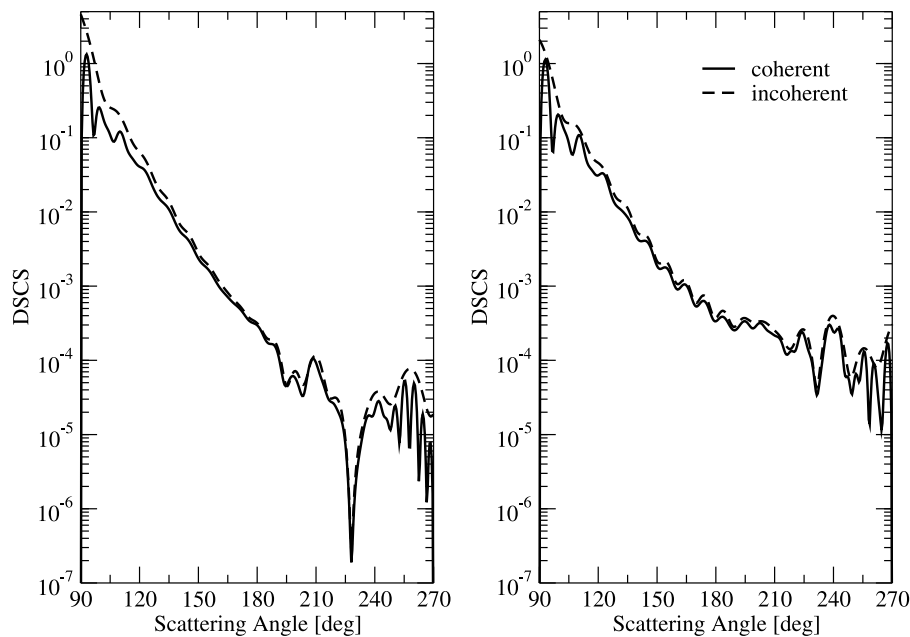
Fig. 9. Differential scattering cross sections for parallel (left) and perpendicular (right) polarizations corresponding to a coherent and an incoherent scattering model. The particle is placed in a simplified stratified medium with $n_0 = n_1 = n_2 = 1.33$, $n_3 = 1.42$, and $n_4 = 1.515$, and the incidence angle is $\beta_{inc} = 62°$.

differential scattering cross sections for a simplified stratified medium with $n_0 = n_1 = n_2$ and $n_3 \neq n_4$, computed by using a coherent and an incoherent scattering model. As expected, the incoherent scattering curves are smoother. However, as compared to a realistic stratified medium and a coherent treatment of the thick layers, the integral response is still smaller (by about 45%). The explanation of this decrease in the integral response (regardless of whether we use a coherent or an incoherent scattering model) is that in the case of a simplified stratified medium, we do not take into account the field reflected by the lower glass slide. This field increases the interacting field, and so, the scattered field (even in the case of evanescent scattering).

3.2. Measuring the particle orientation angles

In our analysis we consider the focus intensity distribution $I_{m_2 n_2}(0)$ at the sampling points $X_{m_2} = m_2 \Delta X$ and $Y_{n_2} = n_2 \Delta Y$ for $m_2, n_2 = -N/2+1, \ldots, N/2$, that is, the intensity distribution in the plane $Z = 0$. The number of sampling points over the horizontal wavenumber K is $M = 120$, and the number of FFT sampling points is $N = 512$. The original image is cropped by cutting the image $I_{m_2 n_2}(0)$ outside the range $m_2, n_2 = -N_c/2 + 1, \ldots, N_c/2$, where $N_c = 128$, and then filtered out by setting $I_{m_2 n_2}(0) = 0$ if $I_{m_2 n_2}(0) < \delta_{LPF} I_{max}(0)$, where $I_{max}(0) = \max_{m_2,n_2} I_{m_2 n_2}(0)$ and $\delta_{LPF} = 10^{-1}$ is a low-pass filter tolerance.
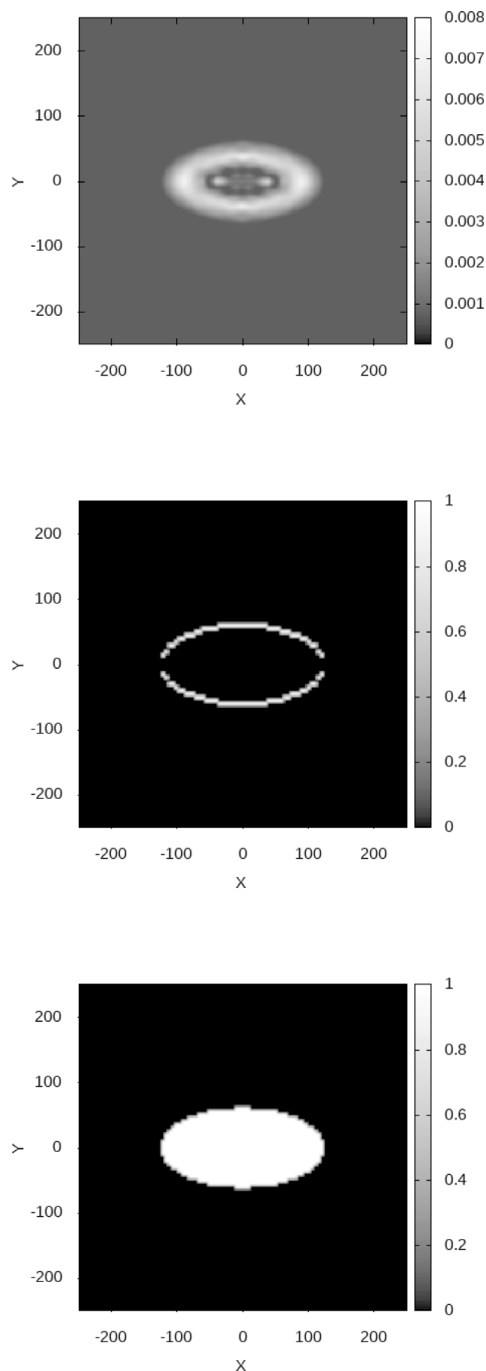
Table 1

Ellipse orientation angle in degree for different low-pass filter tolerances δ_{LPF}. The particle azimuthal orientation angle is $\alpha_p = 45°$.

δ_{LPF}	Bright field illumination ($\beta_{inc} = 0°$)	Evanescent wave illumination ($\beta_{inc} = 62°$)
10^{-1}	44.35	42.65
5×10^{-2}	44.63	38.21
10^{-2}	44.18	34.56
5×10^{-3}	44.22	27.25
10^{-3}	46.68	25.22

1. The dependence of the ellipse orientation angle $\alpha_{ellipse}$ on the particle azimuthal orientation angle α_p is shown in Fig. 13. The plots make clear that the orientation angle of the ellipse reproduces the azimuthal orientation angle of the particle. The dependence is almost linear in the case of bright-field illumination and approximately linear in the case of evanescent wave illumination. Actually, in the latter case, the curve of variation depends on the choice the low-pass filter tolerance δ_{LPF}. From Table 1, we see that the deviations from the azimuthal orientation angle of the particle are more pronounced for lower values of δ_{LPF}. However, this is not a critical problem. Choosing the same tolerance as that which is used for analyzing the measured TIRM images, we can theoretically determine the variation of $\alpha_{ellipse}$ as a function of α_p, i.e., $\alpha_{ellipse} = \alpha_{ellipse}(\alpha_p)$.

2. The variation of the ellipse aspect ratio $\varepsilon_{ellipse}$, defined as the ratio of the semi-major to the semi-minor axis, with the particle azimuthal orientation angle α_p is shown in Fig. 14. For these simulations, the particle zenith orientation angle is $\beta_p = 90°$. As before, it is apparent that the particle aspect ratio $\varepsilon_p = a/b = 2$ is well reproduced by the ellipse aspect ratio $\varepsilon_{ellipse}$ in the case of bright-field illumination, and less so in the case of evanescent wave illumination. In practice, when the dimensions of the particle, and thus, the aspect ratio ε_p are known, the ellipse aspect ratio $\varepsilon_{ellipse}$ is used to determine the particle zenith orientation angle β_p according to the relation $\beta_p = \arcsin(\varepsilon_{ellipse}/\varepsilon_p)$. Note that even in the case of evanescent wave illumination, it is possible to determine a theoretical curve of variation of $\varepsilon_{ellipse}$ as a function of α_p and β_p, i.e., $\varepsilon_{ellipse} = \varepsilon_{ellipse}(\alpha_p, \beta_p)$. Consequently, if the functions $\alpha_{ellipse} = \alpha_{ellipse}(\alpha_p)$ and $\varepsilon_{ellipse} = \varepsilon_{ellipse}(\alpha_p, \beta_p)$ are not multi-valued, the particle orientation angles α_p and β_p can be recovered. This technique was used in Rashidi et al. [20].

3.3. Measuring the separation distance

An important advantage of TIRM is that the integral response of the detector is very sensitive to the separation distance between the particle and the substrate (coating layer). This fact is highlighted in Figs. 15 and 16. The results show that the integral response of the detector decreases rapidly with increasing the separation distance z_3. As seen in Fig. 16, this is not only valid for a realistic stratified medium but also for a simplified stratified medium with $n_0 = n_1 = n_2$ and $n_3 \neq n_4$. An interesting fact that should be mentioned is that for any separation distance z_3, the integral response for a realistic stratified medium is approximately twice as big as the integral response for a simplified stratified medium (the scale factor varies between 1.95 and 2.05). This result, which suggests that the presence of the immersion cell translates into a reduction of the integral response by a factor independent of the separation distance, requires a more detailed analysis in the future.

It should be pointed out that the algorithm also converged in the case $z_3 < R$, where $R = 2.0\,\mu m$ is the radius of the circumscribed sphere, that is, for an interface situated inside the circumscribed sphere. Convergence was achieved for ($N_{rank} = 56, M_{rank} = 50$) in the case $z_3 = 1.4\,\mu m$, ($N_{rank} = 50, M_{rank} = 45$) in the case $z_3 = 1.6\,\mu m$, ($N_{rank} =$

Fig. 10. Image processing step: intensity distribution I/I_{max} (upper panel), outer contour of the image (middle panel), and fitted ellipse (lower panel). The simulations correspond to the incidence angle $\beta_{inc} = 0°$ and the azimuthal orientation angle $\alpha_p = 0°$.

In the image processing step, we transform the image into a binary image (i.e., we set $I_{m_2 n_2}(0) = 1$ if $I_{m_2 n_2}(0) > 0$ for all $m_2, n_2 = -N_c/2 + 1, \ldots, N_c/2$), extract the outer contour, and fit an ellipse to the data (Fig. 10). Specifically, the ellipse fitting is a least squares fitting over (i) the semi-major and semi-minor axes of the ellipse, (ii) the center coordinates, and (iii) the orientation angle of the major axis with respect to the x-axis.

In Figs. 11 and 12 we illustrate some simulated images in the case of bright-field and evanescent wave illuminations, respectively. The results can be interpreted as follows.
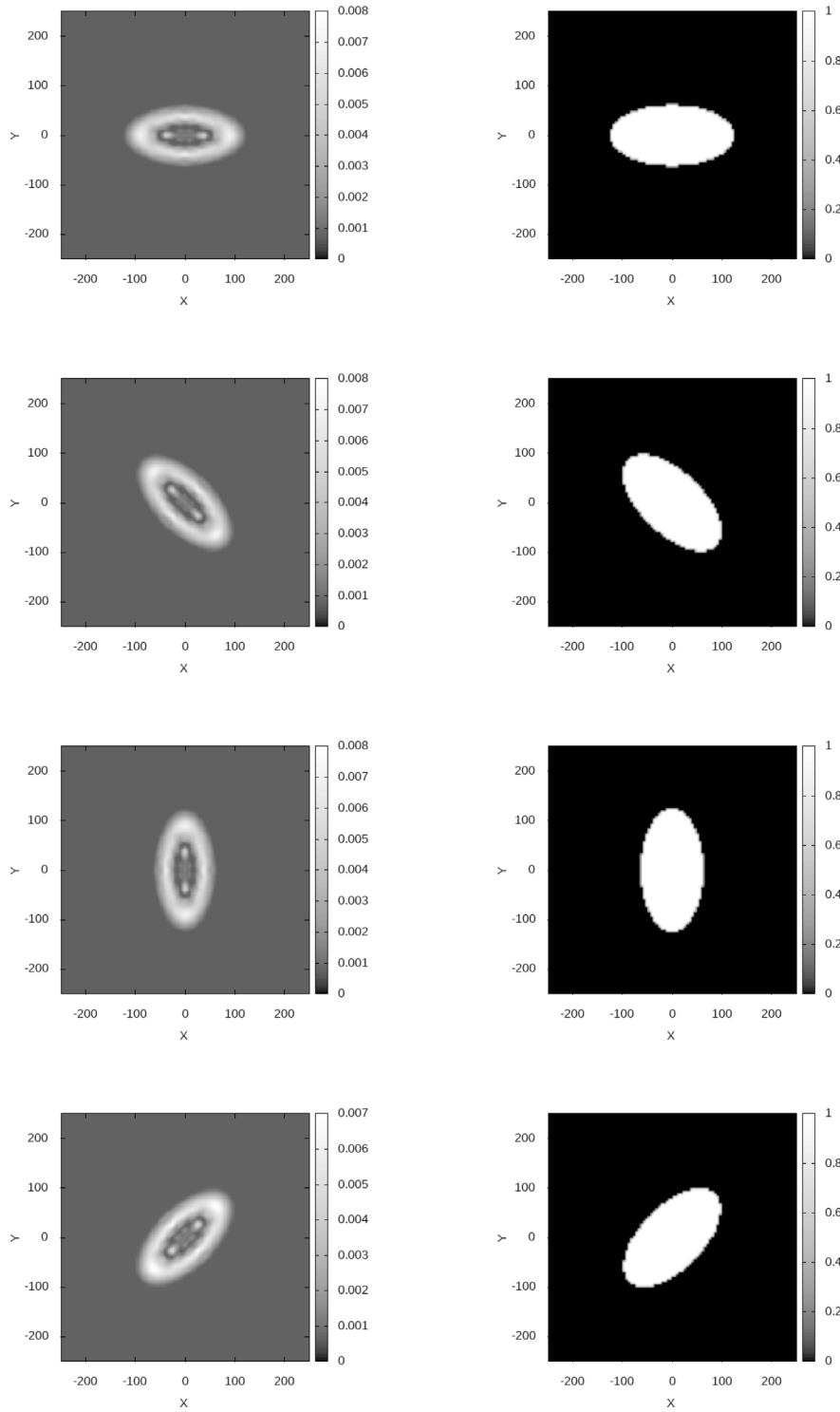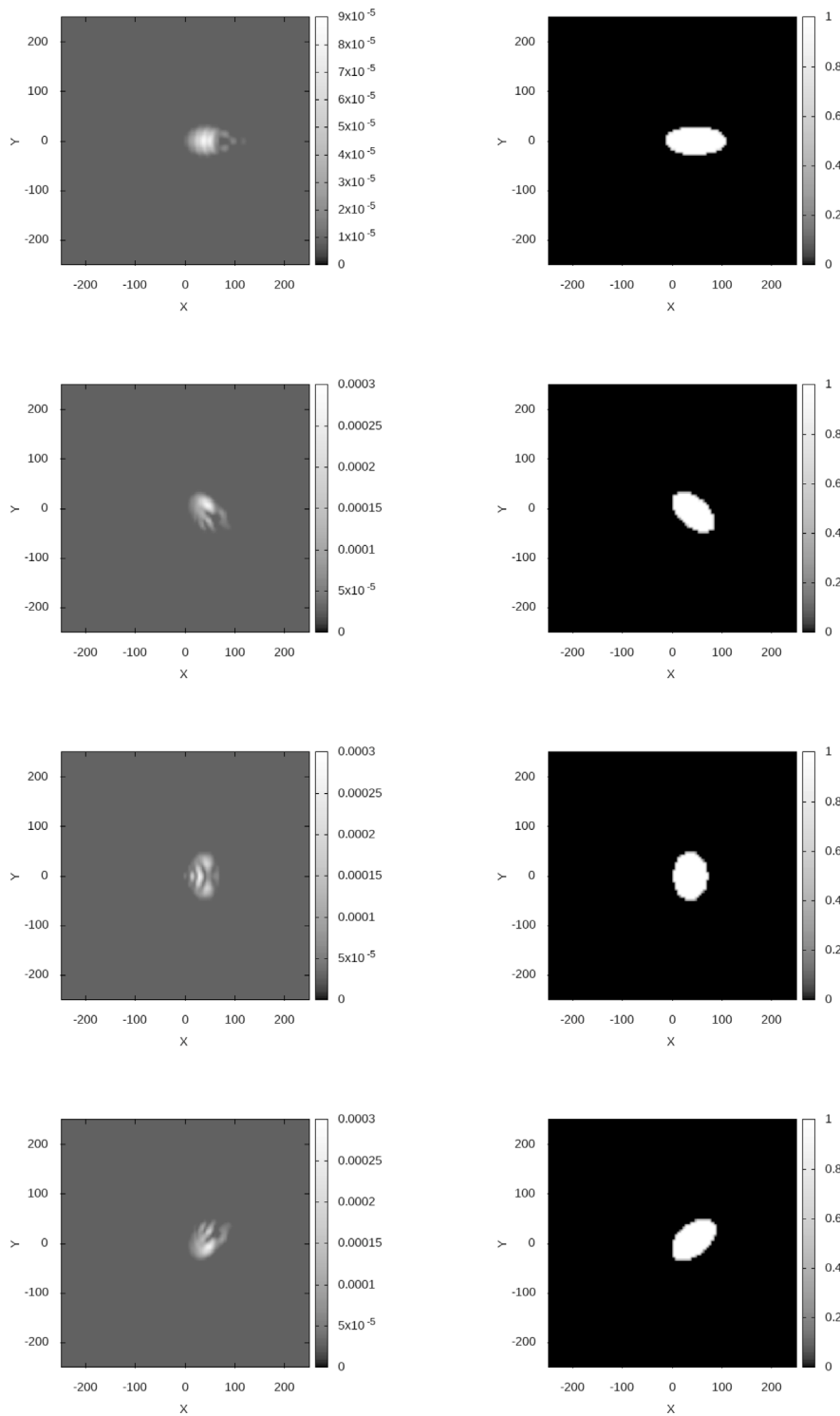
Fig. 11. Intensity distributions I/I_{max} (left columns) and fitted ellipses (right columns). The results correspond to the azimuthal orientation angles $\alpha_p = 0°$ (first row), 45° (second row), 90° (third row), and 135° (fourth row). The incidence angle is $\beta_{inc} = 0°$.

45, $M_{rank} = 40$) in the case $z_3 = 1.8\,\mu m$, and ($N_{rank} = 35$, $M_{rank} = 30$) in the case $z_3 \geq 2.0\,\mu m$. This shows that possible failures of the algorithm, especially for large size parameters, are due to numerical instability.

Along this line it should be pointed out that an important results was derived in Ref. [27]. Considering the integral (94) along the segment $[0, k_{\perp max}]$, the authors found that a large $k_{\perp max}$, leads to a decrease in

Fig. 12. Intensity distributions I/I_{max} (left columns) and fitted ellipses (right columns). The results correspond to the azimuthal orientation angles $\alpha_p = 0°$ (first row), 45° (second row), 90° (third row), and 135° (fourth row). The incidence angle is $\beta_{inc} = 62°$.

the numerical stability. Actually, for a fixed expansion order N_{rank}, the overall numerical accuracy first improves with growing $k_{\perp max}$, and then drops rapidly.

3.4. Uncertainties in layer thicknesses

In our model, the thick layers (the immersion layer of thickness d_{cell}, and the lower glass slide of thickness d_{glass} are treated coher-

ently, i.e., in terms of field amplitudes. The reason is that in order to determine the image of the scattered field, we used the Debye diffraction integral (which involves field amplitudes) for focus field calculation. However, a correct coherent simulation requires that the thicknesses d_{cell} and d_{glass} be know with wavelength-scale precision. This conclusion follows immediately by looking at the phase terms which appear in the expressions of the scattering coefficients (listed in Appendix B). Because the thickness tolerances are of the order of
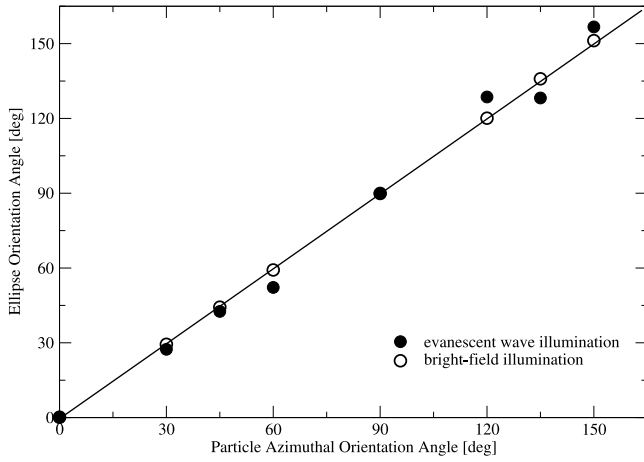
Fig. 13. Ellipse orientation angle versus particle azimuthal orientation angle for bright-field ($\beta_{inc} = 0°$) and evanescent wave ($\beta_{inc} = 62°$) illuminations.
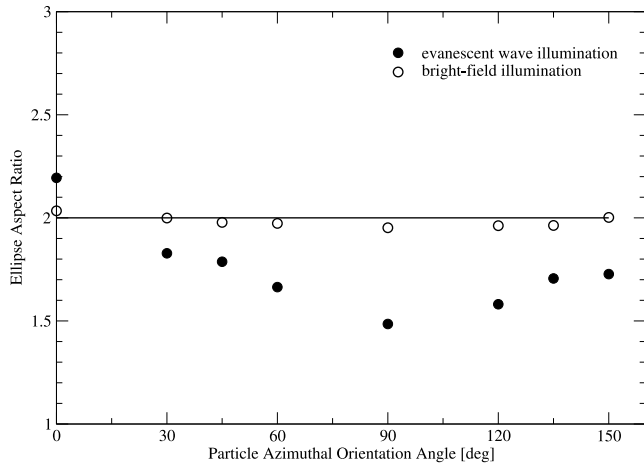

Fig. 14. Ellipse aspect ratio versus particle azimuthal orientation angle for bright-field ($\beta_{inc} = 0°$) and evanescent wave ($\beta_{inc} = 62°$) illuminations. The results correspond to the particle zenith orientation angle $\beta_p = 90°$.

Fig. 15. Differential scattering cross sections for different separation distances z_3 between the particle and the coating layer. The upper plot corresponds to a bright-field illumination ($\beta_{inc} = 0°$), while the lower plot corresponds to an evanescent wave illumination ($\beta_{inc} = 62°$). In the first case, the curves are indistinguishable. The results correspond to parallel polarization and a particle azimuthal orientation angle $\alpha_p = 45°$.

Fig. 16. Integral response of the detector versus the separation distance z_3 in the case of evanescent wave illumination ($\beta_{inc} = 62°$). The results correspond to (i) a simplified stratified medium with $n_0 = n_1 = n_2 = 1.33$, $n_3 = 1.42$, and $n_4 = 1.515$, and (ii) a realistic stratified medium with $n_0 = 1.0003$, $n_1 = 1.515$, $n_2 = 1.33$, $n_3 = 1.42$, and $n_4 = 1.515$. The particle azimuthal orientation angle is $\alpha_p = 45°$.

10 µm, it is desirable to analyze the influence of the layer thickness uncertainties on the detector signal. For this purpose, we

1. assume that d_{cell} and d_{glass} are independent random variables with uniform distributions,
2. generate N_d samples $d_k = (d_{cell\,k}, d_{glass\,k})$, $k = 1, \ldots, N_d$ in the domain $[\overline{d}_{cell} - \delta_{cell}, \overline{d}_{cell} + \delta_{cell}] \times [\overline{d}_{glass} - \delta_{glass}, \overline{d}_{glass} + \delta_{glass}]$, where $\overline{d}$ is the mean, δ the tolerance, and $\sigma = \delta/\sqrt{3}$ the standard deviation, and
3. compute the average of an energetic scattering quantity f (differential scattering cross section, integral response of the detector, focus intensity in the image space) over the thickness realizations d_k, $k = 1, \ldots, N_d$, i.e., compute $\overline{f(d)} = (1/N_d) \sum_k f(d_k)$.

In particular, our intention is to compare $\overline{f(d)}$ with $f(\overline{d})$. In Fig. 17 we illustrate the differential scattering cross sections $\overline{\sigma_X(d)}$ and $\sigma_X(\overline{d})$ for X =⊥, ∥. In this simulation, we choose $N_d = 1000$, $\overline{d}_{cell} = 2.0 \times 10^3$ µm, $\overline{d}_{glass} = 1.0 \times 10^3$ µm, and $\delta_{cell} = \delta_{glass} = 10$ µm. Actually, we used a Python script which serves as a wrapper for the original Fortran model; this employs shell commands to manage the output files from different processes and generates input files for each case. We leveraged the parallelization capabilities of Python's joblib library, distributing tasks across 12 servers, each with 80 cores, allowing for the simultaneous
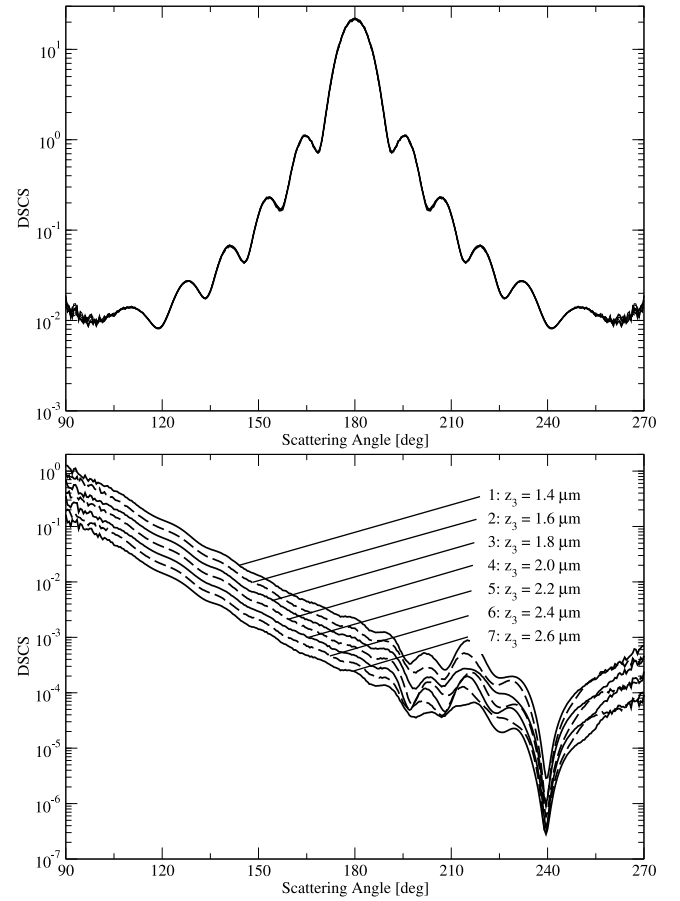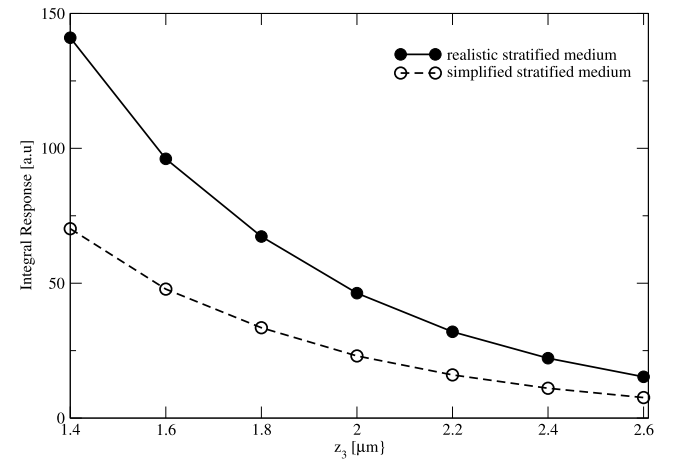
execution of approximately 960 cases. However, given the shared RAM and corresponding limitations on the number of concurrent processes, we were actually able to run about 300 cases at the same time.
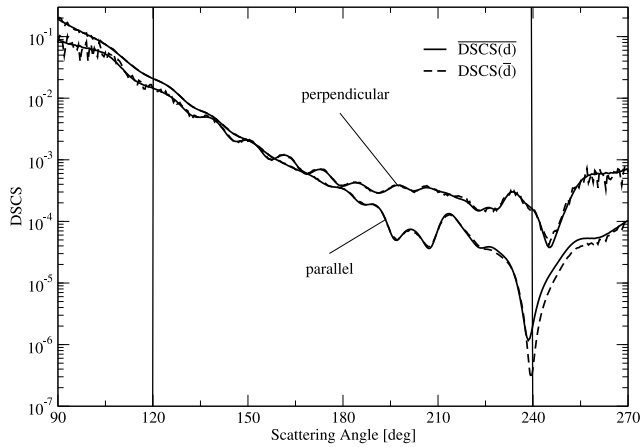
Fig. 17. Differential scattering cross sections $\overline{\sigma_X(d)}$ (denoted by $\overline{DSCS(d)}$) and $\sigma_X(\overline{d})$ (denoted by $DSCS(\overline{d})$) for parallel (X =∥) and perpendicular (X =⊥) polarizations. The particle is placed in a stratified medium with $n_0 = 1.0003$, $n_1 = 1.515$, $n_2 = 1.33$, $n_3 = 1.42$, and $n_4 = 1.515$, and the separation distance, the particle azimuthal orientation angle, and the incidence angle are $z_3 = 2.4\,\mu m$, $\alpha_p = 45°$, and $\beta_{inc} = 62°$, respectively. The vertical lines at 120° and 240° define the angular scattering domain analyzed by the detector.

Completing the full set of 1,000 simulations took 40 min. The results show that $\overline{\sigma_X(d)}$ is a smoothed version of $\sigma_X(\overline{d})$, and that in the angular scattering domain analyzed by the detector, the curves are very close. As a result, the integral responses of the detector are almost the same, i.e., $\overline{P(d)} = 22.210$ and $P(\overline{d}) = 22.227$. Note that because in the image processing step, the fitted ellipses are obtained by an image filtering, a binary-image transformation, and a contour extraction, they remain practically unchanged through the averaging process. These results are not shown here.

4. Conclusions

An advanced light scattering model for TIRM was described herein. The model treats (i) the scattering by an axisymmetric particle of arbitrary orientation situated in a stratified medium and (ii) the imaging of the scattered light.

The important tasks related to the scattering analysis include the calculation of (i) the layer system responses to the incident and scattered fields, (ii) the interaction matrix, and (iii) the transition matrix of an isolated particle. The layer system responses were computed as plane wave expansions and then transformed into regular spherical wave expansions, while the transition matrix was calculated with the null-field method. To deal with an arbitrary particle orientation, the addition theorem for vector spherical wave functions under coordinate rotations was used. An important theoretical development was the computation of the interaction matrix, and so of the system T matrix by (i) truncating the scattered and internal field expansions and (ii) employing spherical and plane wave expansions for the dyadic Green's function. While the spherical wave expansion is valid outside a sphere enclosing the particle, the plane wave expansion is valid outside the tangent planes bounding the particle. We showed that in both cases, the expressions of the interaction matrix were the same. This results demonstrates that the restrictive condition according to which the sphere enclosing the particle should be at most tangent to the interface is not required.

The image of the scattered field was obtained by computing (i) the scattered field on the Gaussian reference sphere of the collector lens, (ii) the transmitted field on the Gaussian reference sphere of the detector lens, and (iii) the focus field by means of the Debye diffraction integral and fast Fourier transform. In addition, for a better reconstruction of the

particle orientation, an image processing step consisting in a contour extraction and ellipse fitting was considered.

In the case of a prolate spheroid, the numerical simulations were focused on a model validation and an analysis of

1. a simplified stratified medium with coherent and incoherent scattering,
2. the influence of the layer thickness uncertainties on the signal, and
3. the model ability to recover the particle orientation angles and separation distance.

The latter simulations were not exhaustive. They were only intended to show the exquisite sensitivity of the geometric parameters of the image ellipse to the particle orientation angles. A more detailed analysis, with the specification of the variation curves $\alpha_{ellipse} = \alpha_{ellipse}(\alpha_p)$ and $\varepsilon_{ellipse} = \varepsilon_{ellipse}(\alpha_p, \beta_p)$, is an ongoing work. In the future we intend to improve the algorithm by

1. including the invariant embedding method [36–38], in order to compute the transition matrix of particles with complex geometries, such as capped spheres and biconcave discs,
2. incorporating a Gaussian beam illumination by using the plane wave representation of a third-order Davis beam [39],
3. modeling chiral particles as in Ref. [28], in order to study chiroptical effects for a circularly polarized incident wave,
4. adding a second incident wave, in order to avoid the multi-valued nature of the functions $\alpha_{ellipse} = \alpha_{ellipse}(\alpha_p)$ and $\varepsilon_{ellipse} = \varepsilon_{ellipse}(\alpha_p, \beta_p)$,
5. fitting a two-dimensional Gaussian to the particle image (as in Ref. [20]), in order to improve the reconstruction process of the particle orientation angles,
6. computing the integral (96) by means of a trapezoidal quadrature rule along a reduced domain of integration, e.g., $[0, x_{max}]$, and determining a relationship between x_{max} and N_{rank} (as in Ref. [27]), in order to increase the numerical stability of the method for particles with large size parameters situated very close to the substrate.

CRediT authorship contribution statement

Alexandru Doicu: Writing – original draft, Software, Investigation. **Dmitry S. Efremenko:** Writing – original draft, Formal analysis, Investigation. **Christopher L. Wirth:** Writing – review & editing, Methodology, Investigation. **Thomas Wriedt:** Writing – review & editing, Conceptualization, Investigation.

Declaration of competing interest

The authors declare that they have no known competing financial interests or personal relationships that could have appeared to influence the work reported in this paper.

Data availability

No data was used for the research described in the article.

Appendix A. Vector spherical wave functions and vector plane waves

The vector spherical wave functions are defined by

$$\mathbf{M}_{mn}^{1,3}(k\mathbf{r}) = z_n^{1,3}(kr)\mathbf{m}_{mn}(\theta,\varphi),$$

$$\mathbf{N}_{mn}^{1,3}(k\mathbf{r}) = \sqrt{n(n+1)}\frac{z_n^{1,3}(kr)}{kr}\mathbf{l}_{mn}(\theta,\varphi) + \frac{[krz_n^{1,3}(kr)]'}{kr}\mathbf{n}_{mn}(\theta,\varphi), \tag{A.1}$$

where $\mathbf{r} = (r, \theta, \varphi)$, z_n^1 designates the spherical Bessel functions j_n, z_n^3 stands for the spherical Hankel functions of the first order $h_n^{(1)}$,

$$\mathbf{l}_{mn}(\theta, \varphi) = \frac{1}{\sqrt{2}} P_n^{|m|}(\cos\theta) e^{jm\varphi} \hat{\mathbf{r}},$$

$$\mathbf{n}_{mn}(\theta, \varphi) = \frac{1}{\sqrt{2n(n+1)}} [\tau_n^{|m|}(\theta)\hat{\theta} + jm\pi_n^{|m|}(\theta)\hat{\varphi}] e^{jm\varphi},$$

$$\mathbf{m}_{mn}(\theta, \varphi) = \frac{1}{\sqrt{2n(n+1)}} [jm\pi_n^{|m|}(\theta)\hat{\theta} - \tau_n^{|m|}(\theta)\hat{\varphi}] e^{jm\varphi} \tag{A.2}$$

are the spherical harmonic vectors, $(\hat{\mathbf{r}}, \hat{\theta}, \hat{\varphi})$ are the spherical unit vectors, $P_n^{|m|}(\cos\theta)$ the associated Legendre functions, and

$$\pi_n^{|m|}(\theta) = \frac{P_n^{|m|}(\cos\theta)}{\sin\theta} \text{ and } \tau_n^{|m|}(\theta) = \frac{d}{d\theta} P_n^{|m|}(\cos\theta), \tag{A.3}$$

the standard angular functions.

The scalar plane wave functions, otherwise known as the Weyl plane wave functions, are defined by

$$\chi(\mathbf{r}, \mathbf{k}^\pm) = \exp(j\mathbf{k}^\pm \cdot \mathbf{r}) = \exp[j(\mathbf{k}_\perp \cdot \mathbf{r}_\perp \pm k_z(k_\perp)z)], \tag{A.4}$$

where

$$\mathbf{k}^\pm = \mathbf{k}_\perp \pm k_z(k_\perp)\hat{\mathbf{z}}, \tag{A.5}$$

$$\mathbf{r} = \mathbf{r}_\perp + z\hat{\mathbf{z}}, \tag{A.6}$$

and

$$\mathbf{r}_\perp = x\hat{\mathbf{x}} + y\hat{\mathbf{y}}, \tag{A.7}$$

$$\mathbf{k}_\perp = k_x\hat{\mathbf{x}} + k_y\hat{\mathbf{y}}, \tag{A.8}$$

$$k_z(k_\perp) = \sqrt{k^2 - k_\perp^2}, \quad \text{Im}(k_z) \geq 0, \tag{A.9}$$

$$k_\perp = \sqrt{k_x^2 + k_y^2}, \tag{A.10}$$

with $(\hat{\mathbf{x}}, \hat{\mathbf{y}}, \hat{\mathbf{z}})$ being the Cartesian unit vectors. These scalar functions can be used to represent upward and downward propagating waves, as well as, upward and downward evanescent waves. In Eq. (A.9), $k_\perp$, and so, k_x and k_y are real, but k_z can be complex if k is real and $k < k_\perp$, or k is complex. The vector plane wave functions $\mathbf{M}(\mathbf{r}, \mathbf{k}^\pm)$ and $\mathbf{N}(\mathbf{r}, \mathbf{k}^\pm)$ are transverse vector functions and are defined in terms of scalar plane wave functions by

$$\mathbf{M}(\mathbf{r}, \mathbf{k}^\pm) = -j\hat{\varphi}(\hat{\mathbf{k}}^\pm)\chi(\mathbf{r}, \mathbf{k}^\pm), \tag{A.11}$$

$$\mathbf{N}(\mathbf{r}, \mathbf{k}^\pm) = -\hat{\theta}(\hat{\mathbf{k}}^\pm)\chi(\mathbf{r}, \mathbf{k}^\pm), \tag{A.12}$$

where $(\hat{\mathbf{k}}^\pm, \hat{\theta}(\hat{\mathbf{k}}^\pm), \hat{\varphi}(\hat{\mathbf{k}}^\pm))$ are the spherical unit vectors.

In the half-space $z > 0$, the radiating vector spherical wave functions can be expressed in terms of upward propagating vector plane waves as

$$\mathbf{M}_{mn}^3(k_2\mathbf{r}) = \int_0^{2\pi}\int_0^{\pi/2-j\infty} [A_{mn}^{SP}(\beta, \alpha)\mathbf{M}(\mathbf{r}, \mathbf{k}_2^+) + B_{mn}^{SP}(\beta, \alpha)\mathbf{N}(\mathbf{r}, \mathbf{k}_2^+)]\sin\beta d\beta d\alpha, \tag{A.13}$$

$$\mathbf{N}_{mn}^3(k_2\mathbf{r}) = \int_0^{2\pi}\int_0^{\pi/2-j\infty} [B_{mn}^{SP}(\beta, \alpha)\mathbf{M}(\mathbf{r}, \mathbf{k}_2^+) + A_{mn}^{SP}(\beta, \alpha)\mathbf{N}(\mathbf{r}, \mathbf{k}_2^+)]\sin\beta d\beta d\alpha, \tag{A.14}$$

where $\mathbf{k}_2^+ = (k_2, \beta, \alpha)$, and the amplitudes $A_{mn}^{SP}(\beta, \alpha)$ and $B_{mn}^{SP}(\beta, \alpha)$ are given respectively, by

$$A_{mn}^{SP}(\beta, \alpha) = \frac{1}{2\pi j^{n+1}} \frac{1}{\sqrt{2n(n+1)}} \tau_n^{|m|}(\beta)e^{jm\alpha}, \tag{A.15}$$

$$B_{mn}^{SP}(\beta, \alpha) = \frac{1}{2\pi j^{n+1}} \frac{1}{\sqrt{2n(n+1)}} m\pi_n^{|m|}(\beta)e^{jm\alpha}. \tag{A.16}$$

In the half-space $z < 0$, we have the representations

$$\mathbf{M}_{mn}^3(k_2\mathbf{r}) = \int_0^{2\pi}\int_0^{\pi/2-j\infty} [A_{mn}^{SP}(\pi - \beta, \alpha)\mathbf{M}(\mathbf{r}, \mathbf{k}_2^-) + B_{mn}^{SP}(\pi - \beta, \alpha)\mathbf{N}(\mathbf{r}, \mathbf{k}_2^-)]\sin\beta d\beta d\alpha, \tag{A.17}$$

$$\mathbf{N}_{mn}^3(k_2\mathbf{r}) = \int_0^{2\pi}\int_0^{\pi/2-j\infty} [B_{mn}^{SP}(\pi - \beta, \alpha)\mathbf{M}(\mathbf{r}, \mathbf{k}_2^-) + A_{mn}^{SP}(\pi - \beta, \alpha)\mathbf{N}(\mathbf{r}, \mathbf{k}_2^-)]\sin\beta d\beta d\alpha, \tag{A.18}$$

where $\mathbf{k}_2^- = (k_2, \pi - \beta, \alpha)$.

The upward propagating vector plane waves can be expanded in terms of regular vector spherical wave functions as

$$\mathbf{M}(\mathbf{r}, \mathbf{k}_2^+) = \sum_{n=1}^\infty \sum_{m=-n}^n [A_{mn}^{PS}(\beta, \alpha)\mathbf{M}_{mn}^1(k_2\mathbf{r}) + B_{mn}^{PS}(\beta, \alpha)\mathbf{N}_{mn}^1(k_2\mathbf{r})], \tag{A.19}$$

$$\mathbf{N}(\mathbf{r}, \mathbf{k}_2^+) = \sum_{n=1}^\infty \sum_{m=-n}^n [B_{mn}^{PS}(\beta, \alpha)\mathbf{M}_{mn}^1(k_2\mathbf{r}) + A_{mn}^{PS}(\beta, \alpha)\mathbf{N}_{mn}^1(k_2\mathbf{r})], \tag{A.20}$$

where

$$A_{mn}^{PS}(\beta, \alpha) = \frac{4j^{n+1}}{\sqrt{2n(n+1)}} \tau_n^{|m|}(\beta)e^{-jm\alpha}, \tag{A.21}$$

$$B_{mn}^{PS}(\beta, \alpha) = \frac{4j^{n+1}}{\sqrt{2n(n+1)}} m\pi_n^{|m|}(\beta)e^{-jm\alpha}. \tag{A.22}$$

For downward propagating vector plane waves, we have the expansions

$$\mathbf{M}(\mathbf{r}, \mathbf{k}_2^-) = \sum_{n=1}^\infty \sum_{m=-n}^n [A_{mn}^{PS}(\pi - \beta, \alpha)\mathbf{M}_{mn}^1(k_2\mathbf{r}) + B_{mn}^{PS}(\pi - \beta, \alpha)\mathbf{N}_{mn}^1(k_2\mathbf{r})], \tag{A.23}$$

$$\mathbf{N}(\mathbf{r}, \mathbf{k}_2^-) = \sum_{n=1}^\infty \sum_{m=-n}^n [B_{mn}^{PS}(\pi - \beta, \alpha)\mathbf{M}_{mn}^1(k_2\mathbf{r}) + A_{mn}^{PS}(\pi - \beta, \alpha)\mathbf{N}_{mn}^1(k_2\mathbf{r})]. \tag{A.24}$$

Appendix B. Scattering in a stratified medium

A stratified medium is a collection of layers filled with a homogeneous medium and separated by z-surfaces. The scattering in a stratified medium was described by Egel [29] by following the prescriptions given by Ko and Sambles [40]. Specifically, in each layer, the electric field is expanded in terms of upward and downward propagating vector plane waves, relative to a local coordinate system with the origin at the bottom of the layer. Reflection at a layer interface relates the upward propagating wave to its downward propagating counterpart. This relation is expressed in matrix form, by organizing the coefficients of the upward and downward propagating vector plane waves into a two-dimensional vector (for each state of polarization). The coefficient vectors for two neighboring layers are linked by a transfer matrix, which is computed from the boundary conditions for the electromagnetic fields. The transfer matrix of the layer system is then calculated as the product of the individual transfer matrices corresponding to all neighboring layers. However, for evanescent field propagation, the transfer matrix scheme is numerically unstable. A numerically more stable algorithm is the scattering matrix formalism. The scattering matrix of a layer system relates the coefficients of the outgoing vector plane waves to the incoming amplitudes, and is computed by using the iterative scheme described by Ko and Sambles [40]. Subsequently, the scattering matrix scheme was used by Egel to compute the waves generated inside the layer system by a scattering center.

In this section we give the main formulas describing the scattering in the assumed stratified medium, which are relevant for computing the interacting and the scattered fields. Instead of using the iterative approach described in Ko and Sambles [40], we will use a direct approach based on the superposition method. The use of this approach is facilitated by the fact that the geometry of the layer system is not very complicated.

Let us consider the layer system illustrated in Fig. 2, where n_j and $k_j = n_j k$ are the absolute refractive index and the wavenumber in medium j, respectively, and k is the wavenumber in vacuum. The different angles of incidence and refraction are determined by Snell's

law

$$n_0 \sin\beta_0 = n_1 \sin\beta_1 = n_2 \sin\beta_2 = n_3 \sin\beta_3 = n_4 \sin\beta_4, \qquad (B.1)$$

where $\beta_j \in [0, \pi/2 - \mathrm{j}\infty)$. For example, in the case of a plane electromagnetic wave propagating in medium 2 at the angle of incidence β_2, we compute $\cos\beta_j = \pm\sqrt{1 - (n_2/n_j)^2 \sin^2\beta_2}$, $j = 0, 1, 3, 4$ and choose the sign of the square root, such that $\mathrm{Im}(\cos\beta_j) \geq 0$. In this way, we guarantee that the amplitudes of the upward and downward propagating waves will tend to zero with increasing $|z|$. The z-components of the wavenumbers are then calculated as $k_z^{(j)} = k_j \cos\beta_j$. The amplitudes of the refracted waves are computed by using the Fresnel equations. In general, for a plane electromagnetic wave traveling from medium 1 into medium 2, the reflection and transmission Fresnel coefficients for perpendicular ($\perp$) and parallel ($\parallel$) polarizations are given respectively, by

$$R_{21\perp} = \frac{k_z^{(1)} - k_z^{(2)}}{k_z^{(1)} + k_z^{(2)}}, \qquad (B.2)$$

$$R_{21\parallel} = \frac{k_2^2 k_z^{(1)} - k_1^2 k_z^{(2)}}{k_2^2 k_z^{(1)} + k_1^2 k_z^{(2)}} = \frac{n_2^2 k_z^{(1)} - n_1^2 k_z^{(2)}}{n_2^2 k_z^{(1)} + n_1^2 k_z^{(2)}}, \qquad (B.3)$$

and

$$T_{21\perp} = \frac{2 k_z^{(1)}}{k_z^{(1)} + k_z^{(2)}}, \qquad (B.4)$$

$$T_{21\parallel} = \frac{2 k_1 k_2 k_z^{(1)}}{k_2^2 k_z^{(1)} + k_1^2 k_z^{(2)}} = \frac{2 n_1 n_2 k_z^{(1)}}{n_2^2 k_z^{(1)} + n_1^2 k_z^{(2)}}. \qquad (B.5)$$

Note that the lower indices in the expressions of Fresnel's coefficients are read from right to left, i.e., 21 stands for a wave traveling from medium 1 into medium 2.

In a first step, we consider the layer system a consisting of the layer 3 and the half-space 4, and the layer system b consisting of the half-space 0 and the layer 1. The layer systems a and b are bounded from below and from above by a half-space with the refractive index n_2 corresponding to the layer 2, respectively. We consider the following situations.

1. The half-space 2 and the layer system a. For an external excitation represented by the vector plane waves propagating upward in the half-space 2 (Fig. B.18a),

$$\mathbf{E}_2^+ = \mathbf{M}(\mathbf{r}, \mathbf{k}_2^+) \text{ and } \mathbf{E}_2^+ = \mathbf{N}(\mathbf{r}, \mathbf{k}_2^+),$$

the transmitted fields in the half-space 4 are

$$\mathbf{E}_{4T}^+ = S_{a\perp}^+ \mathbf{M}(\mathbf{r}, \mathbf{k}_4^+) \text{ and } \mathbf{E}_{4T}^+ = S_{a\parallel}^+ \mathbf{N}(\mathbf{r}, \mathbf{k}_4^+),$$

respectively, while the reflected fields in the half-space 2 are

$$\mathbf{E}_{2R}^- = S_{a\perp}^- \mathbf{M}(\mathbf{r}, \mathbf{k}_2^-) \text{ and } \mathbf{E}_{2R}^- = S_{a\parallel}^- \mathbf{N}(\mathbf{r}, \mathbf{k}_2^-),$$

respectively. The scattering coefficients S_{aX}^+ and S_{aX}^-, $X = \perp, \parallel$, are given respectively, by

$$S_{aX}^+ = e^{\mathrm{j}[k_z^{(2)} - k_z^{(3)}]z_3} \frac{\mathcal{T}_{43X}}{1 - \mathcal{R}_{23X}\mathcal{R}_{43X}} T_{32X}, \qquad (B.6)$$

$$S_{aX}^- = e^{2\mathrm{j}k_z^{(2)} z_3} R_{32X} + e^{\mathrm{j}[k_z^{(2)} - k_z^{(3)}]z_3} \frac{\mathcal{T}_{23X}\mathcal{R}_{43X}}{1 - \mathcal{R}_{23X}\mathcal{R}_{43X}} T_{32X}, \qquad (B.7)$$

where

$$\mathcal{R}_{23X} = e^{-2\mathrm{j}k_z^{(3)} z_3} R_{23X}, \quad \mathcal{T}_{23X} = e^{\mathrm{j}[k_z^{(2)} - k_z^{(3)}]z_3} T_{23X}, \qquad (B.8)$$

$$\mathcal{R}_{43X} = e^{2\mathrm{j}k_z^{(3)} z_4} R_{43X}, \quad \mathcal{T}_{43X} = e^{\mathrm{j}[k_z^{(3)} - k_z^{(4)}]z_4} T_{43X}. \qquad (B.9)$$

If the external excitation is represented by the vector plane waves propagating downward in the half-space 4 (Fig. B.18b),

$$\mathbf{E}_4^- = \mathbf{M}(\mathbf{r}, \mathbf{k}_4^-) \text{ and } \mathbf{E}_4^- = \mathbf{N}(\mathbf{r}, \mathbf{k}_4^-),$$

the transmitted fields in the half-space 2 are

$$\mathbf{E}_{2T}^- = \widetilde{S}_{a\perp}^- \mathbf{M}(\mathbf{r}, \mathbf{k}_2^-) \text{ and } \mathbf{E}_{2T}^- = \widetilde{S}_{a\parallel}^- \mathbf{N}(\mathbf{r}, \mathbf{k}_2^-),$$
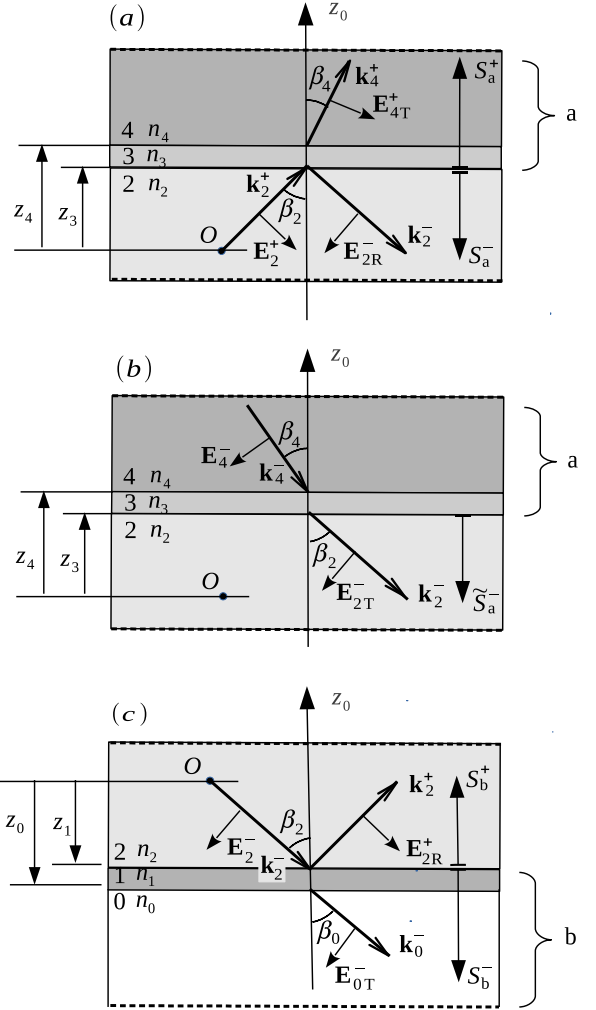

Fig. B.18. The layer system a consisting of the layer 3 and the half-space 4, and the layer system b consisting of the half-space 0 and the layer 1. The external excitation is represented by vector plane waves propagating upward in the half-space 2 (a), downward in the half-space 4 (b), and downward in the half-space 2 (c).

where

$$\widetilde{S}_{aX}^- = e^{\mathrm{j}[k_z^{(3)} - k_z^{(4)}]z_4} \frac{\mathcal{T}_{23X}}{1 - \mathcal{R}_{43X}\mathcal{R}_{23X}} T_{34X}. \qquad (B.10)$$

2. The half-space 2 and the layer system b. For an external excitation represented by the vector plane waves propagating downward in the half-space 2 (Fig. B.18c),

$$\mathbf{E}_2^- = \mathbf{M}(\mathbf{r}, \mathbf{k}_2^-) \text{ and } \mathbf{E}_2^- = \mathbf{N}(\mathbf{r}, \mathbf{k}_2^-),$$

the reflected fields in the half-space 2 are

$$\mathbf{E}_{2R}^+ = S_{b\perp}^+ \mathbf{M}(\mathbf{r}, \mathbf{k}_2^+) \text{ and } \mathbf{E}_{2R}^+ = S_{b\parallel}^+ \mathbf{N}(\mathbf{r}, \mathbf{k}_2^+),$$

respectively, while the transmitted fields in the half-space 0 are

$$\mathbf{E}_{0T}^- = S_{b\perp}^- \mathbf{M}(\mathbf{r}, \mathbf{k}_0^-) \text{ and } \mathbf{E}_{0T}^- = S_{b\parallel}^- \mathbf{N}(\mathbf{r}, \mathbf{k}_0^-),$$

respectively. The scattering coefficients S_{bX}^+ and S_{bX}^-, $X = \perp, \parallel$, are given respectively, by

$$S_{bX}^+ = e^{-2\mathrm{j}k_z^{(2)} z_1} R_{12X} + e^{\mathrm{j}[k_z^{(1)} - k_z^{(2)}]z_1} \frac{\mathcal{T}_{21X}\mathcal{R}_{01X}}{1 - \mathcal{R}_{21X}\mathcal{R}_{01X}} T_{12X}, \qquad (B.11)$$

$$S_{bX}^- = e^{\mathrm{j}[k_z^{(1)} - k_z^{(2)}]z_1} \frac{\mathcal{T}_{01X}}{1 - \mathcal{R}_{21X}\mathcal{R}_{01X}} T_{12X}, \qquad (B.12)$$
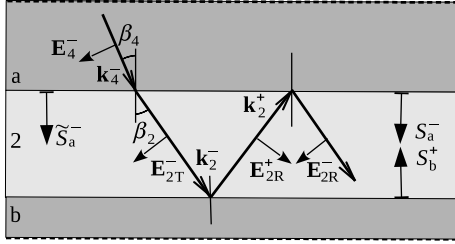
Fig. B.19. Geometry for computing the incident field. The external excitation is represented by vector plane waves propagating downward in the half-space 4.

where

$$\mathcal{R}_{01X} = e^{-2jk_z^{(1)}z_0}R_{01X}, \quad \mathcal{T}_{01X} = e^{j[k_z^{(0)}-k_z^{(1)}]z_0}T_{01X}, \tag{B.13}$$

$$\mathcal{R}_{21X} = e^{2jk_z^{(1)}z_1}R_{21X}, \quad \mathcal{T}_{21X} = e^{j[k_z^{(1)}-k_z^{(2)}]z_1}T_{21X}. \tag{B.14}$$

We come now to the layer system shown in Fig. 2, in which the layer 2 is of finite vertical extent. To characterize the incident field, we consider as external excitation the vector plane waves propagating downward in the half-space 4 (Fig. B.19),

$$\mathbf{E}_4^- = \mathbf{M}(\mathbf{r}, \mathbf{k}_4^-) \text{ and } \mathbf{E}_4^- = \mathbf{N}(\mathbf{r}, \mathbf{k}_4^-).$$

In this case, the total upward propagating fields in layer 2 are

$$\mathbf{E}_{2tot}^+ = \mathbf{E}_{2R}^+ = \tilde{S}_\perp^+ \mathbf{M}(\mathbf{r}, \mathbf{k}_2^+) \text{ and } \mathbf{E}_{2tot}^+ = \mathbf{E}_{2R}^+ = \tilde{S}_\parallel^+ \mathbf{N}(\mathbf{r}, \mathbf{k}_2^+),$$

respectively, while the total downward propagating fields are

$$\mathbf{E}_{2tot}^- = \mathbf{E}_{2T}^- + \mathbf{E}_{2R}^- = \tilde{S}_\perp^- \mathbf{M}(\mathbf{r}, \mathbf{k}_2^-) \text{ and } \mathbf{E}_{2tot}^- = \mathbf{E}_{2T}^- + \mathbf{E}_{2R}^- = \tilde{S}_\parallel^- \mathbf{N}(\mathbf{r}, \mathbf{k}_2^-),$$

respectively. The scattering coefficients $\tilde{S}_X^+$ and $\tilde{S}_X^-$, X $=\perp, \parallel$, are given respectively, by

$$\tilde{S}_X^+ = \frac{\tilde{S}_{aX}^- S_{bX}^+}{1 - S_{aX}^- S_{bX}^+}, \tag{B.15}$$

$$\tilde{S}_X^- = \frac{\tilde{S}_{aX}^-}{1 - S_{aX}^- S_{bX}^+}. \tag{B.16}$$

To compute the interaction matrix and to characterize the scattered field, we consider two situations.

1. The external excitation is represented by the vector plane waves propagating upward in layer 2 (Fig. B.20a),

$$\mathbf{E}_2^+ = \mathbf{M}(\mathbf{r}, \mathbf{k}_2^+) \text{ and } \mathbf{E}_2^+ = \mathbf{N}(\mathbf{r}, \mathbf{k}_2^+).$$

In this case, the reflected upward propagating fields in layer 2 are

$$\mathbf{E}_{2R}^+ = S_\perp^{++} \mathbf{M}(\mathbf{r}, \mathbf{k}_2^+) \text{ and } \mathbf{E}_{2R}^+ = S_\parallel^{++} \mathbf{N}(\mathbf{r}, \mathbf{k}_2^+),$$

respectively, the reflected downward propagating fields in layer 2 are

$$\mathbf{E}_{2R}^- = S_\perp^{+-} \mathbf{M}(\mathbf{r}, \mathbf{k}_2^-) \text{ and } \mathbf{E}_{2R}^- = S_\parallel^{+-} \mathbf{N}(\mathbf{r}, \mathbf{k}_2^-),$$

respectively, and the transmitted downward propagating fields in the half-space 0 are

$$\mathbf{E}_{0T}^- = S_\perp^+ \mathbf{M}(\mathbf{r}, \mathbf{k}_0^-) \text{ and } \mathbf{E}_{0T}^- = S_\parallel^+ \mathbf{N}(\mathbf{r}, \mathbf{k}_0^-),$$

respectively. The scattering coefficients S_X^{++}, S_X^{+-}, and S_X^+, X $=\perp, \parallel$, are given respectively, by

$$S_X^{++} = \frac{S_{aX}^- S_{bX}^+}{1 - S_{aX}^- S_{bX}^+}, \tag{B.17}$$

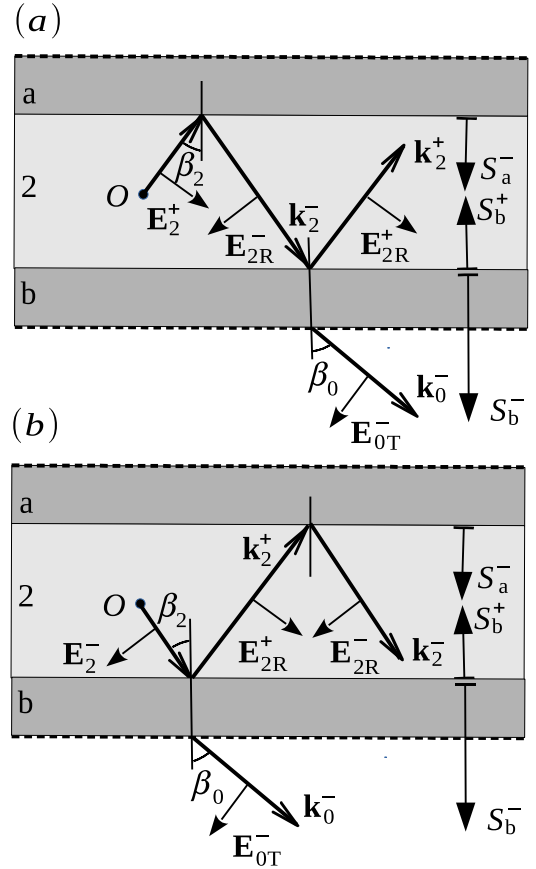$$S_X^{+-} = \frac{S_{aX}^-}{1 - S_{aX}^- S_{bX}^+}, \tag{B.18}$$

Fig. B.20. Geometry for computing the interaction matrix and the scattered field. The external excitation is represented by vector plane waves propagating upward (a) and downward (b) in layer 2.

$$S_X^+ = \frac{S_{aX}^- S_{bX}^-}{1 - S_{aX}^- S_{bX}^+}. \tag{B.19}$$

2. The external excitation is represented by the vector plane waves propagating downward in layer 2 (Fig. B.20b),

$$\mathbf{E}_2^- = \mathbf{M}(\mathbf{r}, \mathbf{k}_2^-) \text{ and } \mathbf{E}_2^- = \mathbf{N}(\mathbf{r}, \mathbf{k}_2^-).$$

In this case, the reflected upward propagating fields in layer 2 are

$$\mathbf{E}_{2R}^+ = S_\perp^{-+} \mathbf{M}(\mathbf{r}, \mathbf{k}_2^+) \text{ and } \mathbf{E}_{2R}^+ = S_\parallel^{-+} \mathbf{N}(\mathbf{r}, \mathbf{k}_2^+),$$

respectively, the reflected downward propagating fields in layer 2 are

$$\mathbf{E}_{2R}^- = S_\perp^{--} \mathbf{M}(\mathbf{r}, \mathbf{k}_2^-) \text{ and } \mathbf{E}_{2R}^- = S_\parallel^{--} \mathbf{N}(\mathbf{r}, \mathbf{k}_2^-),$$

and the transmitted downward propagating fields in the half-space 0 are

$$\mathbf{E}_{0T}^- = S_\perp^- \mathbf{M}(\mathbf{r}, \mathbf{k}_0^-) \text{ and } \mathbf{E}_{0T}^- = S_\parallel^- \mathbf{N}(\mathbf{r}, \mathbf{k}_0^-),$$

respectively. The scattering coefficients S_X^{-+}, S_X^{--}, and S_X^-, X $=\perp, \parallel$, are given respectively, by

$$S_X^{-+} = \frac{S_{bX}^+}{1 - S_{aX}^- S_{bX}^+}, \tag{B.20}$$

$$S_X^{--} = S_X^{++} = \frac{S_{aX}^- S_{bX}^+}{1 - S_{aX}^- S_{bX}^+}, \tag{B.21}$$

$$S_X^- = \frac{S_{bX}^-}{1 - S_{aX}^- S_{bX}^+}. \tag{B.22}$$

In order to compute the elements of the interaction matrix by using Gauss–Laguerre quadrature, we need to factorize the term $\exp(2jk_z^{(2)}z_3)$ in the expressions of the scattering coefficients S_X^{uv}, i.e.,

$$S_X^{uv} = e^{2jk_z^{(2)}z_3}\widehat{S}_X^{uv}, \quad u,v = +,-, \quad X = \perp, \parallel. \tag{B.23}$$

For doing this, we set in Eqs. (B.7) and (B.11)

$$S_{aX}^- = e^{2jk_z^{(2)}z_3}\widehat{S}_{aX}^-, \quad S_{bX}^+ = e^{-2jk_z^{(2)}z_1}\widehat{S}_{bX}^+, \tag{B.24}$$

with

$$\widehat{S}_{aX}^- = R_{32X} + \frac{e^{2jk_z^{(3)}(z_4-z_3)}}{1 - e^{2jk_z^{(3)}(z_4-z_3)}R_{23X}R_{43X}}T_{23X}R_{43X}T_{32X}, \tag{B.25}$$

$$\widehat{S}_{bX}^+ = R_{12X} + \frac{e^{-2jk_z^{(1)}(z_0-z_1)}}{1 - e^{-2jk_z^{(1)}(z_0-z_1)}R_{21X}R_{01X}}T_{21X}R_{01X}T_{12X}, \tag{B.26}$$

and obtain

$$\widehat{S}_X^{++} = \frac{e^{-2jk_z^{(2)}z_1}\widehat{S}_{aX}^-\widehat{S}_{bX}^+}{1 - e^{2jk_z^{(2)}(z_3-z_1)}\widehat{S}_{aX}^-\widehat{S}_{bX}^+}, \tag{B.27}$$

$$\widehat{S}_X^{+-} = \frac{\widehat{S}_{aX}^-}{1 - e^{2jk_z^{(2)}(z_3-z_1)}\widehat{S}_{aX}^-\widehat{S}_{bX}^+}, \tag{B.28}$$

$$\widehat{S}_X^{-+} = \frac{e^{-2jk_z^{(2)}(z_1+z_3)}\widehat{S}_{bX}^+}{1 - e^{2jk_z^{(2)}(z_3-z_1)}\widehat{S}_{aX}^-\widehat{S}_{bX}^+}, \tag{B.29}$$

$$\widehat{S}_X^{--} = \widehat{S}_X^{++} = \frac{e^{-2jk_z^{(2)}z_1}\widehat{S}_{aX}^-\widehat{S}_{bX}^+}{1 - e^{2jk_z^{(2)}(z_3-z_1)}\widehat{S}_{aX}^-\widehat{S}_{bX}^+}. \tag{B.30}$$

Referring to Fig. 2, we distinguish two particular scattering problems.

1. The scattering by a particle placed in the lower half-space and being illuminated by an incident field propagating in the upper half-space. This problem, which corresponds to the scattering by a particle near a substrate (a plane surface separating two half-spaces), can be modeled by choosing $n_0 = n_1 = n_2$ and $n_3 = n_4$. In this case, Eqs. (B.6)–(B.7), (B.11)–(B.12), and (B.10) reduce to

$$S_{aX}^+ = e^{j[k_z^{(2)}-k_z^{(3)}]z_3}T_{32X}, \quad S_{aX}^- = e^{2jk_z^{(2)}z_3}R_{32X}, \tag{B.31}$$

$$S_{bX}^+ = 0, \quad S_{bX}^- = 1, \quad \text{and} \tag{B.32}$$

$$\widetilde{S}_{aX}^- = e^{j[k_z^{(2)}-k_z^{(3)}]z_3}T_{23X}, \tag{B.33}$$

respectively, Eqs. (B.15)–(B.16) to

$$\widetilde{S}_X^+ = 0. \quad \widetilde{S}_X^- = e^{j[k_z^{(2)}-k_z^{(3)}]z_3}T_{23X}, \tag{B.34}$$

Eqs. (B.17)–(B.18) and (B.20)–(B.21) to

$$S_X^{++} = 0, \quad S_X^{+-} = e^{2jk_z^{(2)}z_3}R_{32X}, \quad \text{and} \tag{B.35}$$

$$S_X^{-+} = S_X^{--} = 0, \tag{B.36}$$

respectively, and Eqs. (B.19) and (B.22) to

$$S_X^+ = e^{2jk_z^{(2)}z_3}R_{32X} \quad \text{and} \quad S_X^- = 1, \tag{B.37}$$

respectively.

2. The scattering by a particle placed in the lower half-space and being illuminated by an incident field propagating from the glass prism to the lower half-space through the coating layer. This problem can be modeled by choosing $n_0 = n_1 = n_2$. In this case, Eqs. (B.6)–(B.7) and (B.10) remain valid, but Eqs. (B.11)–(B.12), reduce to

$$S_{bX}^+ = 0, \quad S_{bX}^- = 1, \tag{B.38}$$

Eqs. (B.15)–(B.16) to

$$\widetilde{S}_X^+ = 0. \quad \widetilde{S}_X^- = \widetilde{S}_{aX}^-, \tag{B.39}$$

Eqs. (B.17)–(B.18) and (B.20)–(B.21) to

$$S_X^{++} = 0, \quad S_X^{+-} = S_{aX}^-, \quad \text{and} \tag{B.40}$$

$$S_X^{-+} = S_X^{--} = 0, \tag{B.41}$$

respectively, and Eqs. (B.19) and (B.22) to

$$S_X^+ = S_{aX}^- \quad \text{and} \quad S_X^- = 1, \tag{B.42}$$

respectively.

Appendix C. The system T matrix for a plane wave expansion of the dyadic Green's function

Let $z = z_{\max}$ and $z = z_{\min}$ be two tangent planes bounding the particle from above and below, respectively, and

$$\overline{\mathbf{G}}_0(k_2, \mathbf{r}, \mathbf{r}_1) = -\frac{1}{k_2^2}\delta(\mathbf{r} - \mathbf{r}_1)\widehat{\mathbf{z}} \otimes \widehat{\mathbf{z}}$$
$$+ \frac{jk_2}{8\pi^2}\begin{cases} \int \left[\mathbf{M}(\mathbf{r}, \mathbf{k}_2^+) \otimes \mathbf{M}(-\mathbf{r}_1, \mathbf{k}_2^+) + \mathbf{N}(\mathbf{r}, \mathbf{k}_2^+) \otimes \mathbf{N}(-\mathbf{r}_1, \mathbf{k}_2^+)\right]\frac{d^2\mathbf{k}_\perp}{k_2 k_z^{(2)}}, \\ \qquad\qquad z > z_1 \\ \int \left[\mathbf{M}(\mathbf{r}, \mathbf{k}_2^-) \otimes \mathbf{M}(-\mathbf{r}_1, \mathbf{k}_2^-) + \mathbf{N}(\mathbf{r}, \mathbf{k}_2^-) \otimes \mathbf{N}(-\mathbf{r}_1, \mathbf{k}_2^-)\right]\frac{d^2\mathbf{k}_\perp}{k_2 k_z^{(2)}}, \\ \qquad\qquad z < z_1 \end{cases}. \tag{C.1}$$

the representation for the free-space dyadic Green's function in term of vector plane waves.

For a field point with $z \geq z_{\max} > z_1$, substitution of Eq. (C.1) in Eq. (13), yields the integral representation (22), with the amplitudes

$$F^+(\beta, \alpha) = \frac{jk_2^2}{8\pi^2}\oint_{S_p}\left[\mathbf{N}(-\mathbf{r}_1, \mathbf{k}_2^+) \cdot \mathbf{e}_{\mathrm{int}}(\mathbf{r}_1) + j\sqrt{\frac{\mu_0}{\varepsilon_2}}\mathbf{M}(-\mathbf{r}_1, \mathbf{k}_2^+) \cdot \mathbf{h}_{\mathrm{int}}(\mathbf{r}_1)\right]d^2\mathbf{r}_1, \tag{C.2}$$

$$G^+(\beta, \alpha) = \frac{jk_2^2}{8\pi^2}\oint_{S_p}\left[\mathbf{M}(-\mathbf{r}_1, \mathbf{k}_2^+) \cdot \mathbf{e}_{\mathrm{int}}(\mathbf{r}_1) + j\sqrt{\frac{\mu_0}{\varepsilon_2}}\mathbf{N}(-\mathbf{r}_1, \mathbf{k}_2^+) \cdot \mathbf{h}_{\mathrm{int}}(\mathbf{r}_1)\right]d^2\mathbf{r}_1. \tag{C.3}$$

Approximating the tangential fields $\mathbf{e}_{\mathrm{int}}(\mathbf{r}_1)$ and $\mathbf{h}_{\mathrm{int}}(\mathbf{r}_1)$ in the global coordinate system by a (finite) linear combination of regular vector spherical wave functions, i.e.

$$\mathbf{e}_{\mathrm{int}}^N(\mathbf{r}_1) = \sum_{(m,n)=1}^N \{C_{mn}^N[\widehat{\mathbf{n}}(\mathbf{r}_1) \times \mathbf{M}_{mn}^1(k_p\mathbf{r}_1)] + D_{mn}^N[\widehat{\mathbf{n}}(\mathbf{r}_1) \times \mathbf{N}_{mn}^1(k_p\mathbf{r}_1)]\}, \tag{C.4}$$

$$\mathbf{h}_{\mathrm{int}}^N(\mathbf{r}_1) = -j\sqrt{\frac{\varepsilon_p}{\mu_0}}\sum_{(m,n)=1}^N \{C_{mn}^N[\widehat{\mathbf{n}}(\mathbf{r}_1) \times \mathbf{N}_{mn}^1(k_p\mathbf{r}_1)] + D_{mn}^N[\widehat{\mathbf{n}}(\mathbf{r}_1) \times \mathbf{M}_{mn}^1(k_p\mathbf{r}_1)]\}, \tag{C.5}$$

where k_p and ε_p are the wavenumber and the electric permittivity of the particle, respectively, we obtain (compare with Eqs. (23)–(24))

$$F^+(\beta, \alpha) = \sum_{(m,n)=1}^N [C_{mn}^N q_{mn}^{11}(\beta, \alpha) + D_{mn}^N q_{mn}^{12}(\beta, \alpha)], \tag{C.6}$$

$$G^+(\beta, \alpha) = \sum_{(m,n)=1}^N [C_{mn}^N q_{mn}^{21}(\beta, \alpha) + D_{mn}^N q_{mn}^{22}(\beta, \alpha)], \tag{C.7}$$

where

$$q_{mn}^{11}(\beta, \alpha) = \frac{jk_2^2}{8\pi^2}\oint_{S_p}\left\{[\widehat{\mathbf{n}}(\mathbf{r}_1) \times \mathbf{M}_{mn}^1(k_p\mathbf{r}_1)] \cdot \mathbf{N}(-\mathbf{r}_1, \mathbf{k}_2^+)\right.$$
$$\left. + \sqrt{\frac{\varepsilon_p}{\varepsilon_2}}[\widehat{\mathbf{n}}(\mathbf{r}_1) \times \mathbf{N}_{mn}^1(k_p\mathbf{r}_1)] \cdot \mathbf{M}(-\mathbf{r}_1, \mathbf{k}_2^+)\right\}d^2\mathbf{r}_1, \tag{C.8}$$

$$q_{mn}^{12}(\beta, \alpha) = \frac{jk_2^2}{8\pi^2}\oint_{S_p}\left\{[\widehat{\mathbf{n}}(\mathbf{r}_1) \times \mathbf{N}_{mn}^1(k_p\mathbf{r}_1)] \cdot \mathbf{N}(-\mathbf{r}_1, \mathbf{k}_2^+)\right.$$

$$+ \sqrt{\frac{\varepsilon_{\mathrm{p}}}{\varepsilon_2}} [\hat{\mathbf{n}}(\mathbf{r}_1) \times \mathbf{M}_{mn}^1(k_{\mathrm{p}}\mathbf{r}_1)] \cdot \mathbf{M}(-\mathbf{r}_1, \mathbf{k}_2^+) \Big\} \, \mathrm{d}^2\mathbf{r}_1, \tag{C.9}$$

$$q_{mn}^{21}(\beta, \alpha) = \frac{\mathrm{j}k_2^2}{8\pi^2} \oint_{S_{\mathrm{p}}} \Big\{ [\hat{\mathbf{n}}(\mathbf{r}_1) \times \mathbf{M}_{mn}^1(k_{\mathrm{p}}\mathbf{r}_1)] \cdot \mathbf{M}(-\mathbf{r}_1, \mathbf{k}_2^+)$$

$$+ \sqrt{\frac{\varepsilon_{\mathrm{p}}}{\varepsilon_2}} [\hat{\mathbf{n}}(\mathbf{r}_1) \times \mathbf{N}_{mn}^1(k_{\mathrm{p}}\mathbf{r}_1)] \cdot \mathbf{N}(-\mathbf{r}_1, \mathbf{k}_2^+) \Big\} \, \mathrm{d}^2\mathbf{r}_1, \tag{C.10}$$

$$q_{mn}^{22}(\beta, \alpha) = \frac{\mathrm{j}k_2^2}{8\pi^2} \oint_{S_{\mathrm{p}}} \Big\{ [\hat{\mathbf{n}}(\mathbf{r}_1) \times \mathbf{N}_{mn}^1(k_{\mathrm{p}}\mathbf{r}_1)] \cdot \mathbf{M}(-\mathbf{r}_1, \mathbf{k}_2^+)$$

$$+ \sqrt{\frac{\varepsilon_{\mathrm{p}}}{\varepsilon_2}} [\hat{\mathbf{n}}(\mathbf{r}_1) \times \mathbf{M}_{mn}^1(k_{\mathrm{p}}\mathbf{r}_1)] \cdot \mathbf{N}(-\mathbf{r}_1, \mathbf{k}_2^+) \Big\} \, \mathrm{d}^2\mathbf{r}_1, \tag{C.11}$$

To simplify the expressions for the coefficients $q_{N,mn}^{ij}(\beta, \alpha)$, $i, j = 1, 2$, given by Eqs. (C.4)–(C.11), we use the expansions

$$\mathbf{M}(-\mathbf{r}, \mathbf{k}_2^+) = 8\pi \sum_{n_1=1}^{\infty} \sum_{m_1=-n_1}^{n_1} [A_{m_1 n_1}^{\mathrm{SP}}(\beta, \alpha) \mathbf{M}_{-m_1 n_1}^1(k_2\mathbf{r}) + B_{m_1 n_1}^{\mathrm{SP}}(\beta, \alpha) \mathbf{N}_{-m_1 n_1}^1(k_2\mathbf{r})], \tag{C.12}$$

$$\mathbf{N}(-\mathbf{r}, \mathbf{k}_2^+) = 8\pi \sum_{n_1=1}^{\infty} \sum_{m_1=-n_1}^{n_1} [B_{m_1 n_1}^{\mathrm{SP}}(\beta, \alpha) \mathbf{M}_{-m_1 n_1}^1(k_2\mathbf{r}) + A_{m_1 n_1}^{\mathrm{SP}}(\beta, \alpha) \mathbf{N}_{-m_1 n_1}^1(k_2\mathbf{r})], \tag{C.13}$$

and obtain

$$q_{mn}^{11}(\beta, \alpha) = \sum_{(m_1, n_1)=1}^{N} [A_{m_1 n_1}^{\mathrm{SP}}(\beta, \alpha) Q_{11 m_1 n_1, mn}^{11} + B_{m_1 n_1}^{\mathrm{SP}}(\beta, \alpha) Q_{11 m_1 n_1, mn}^{21}], \tag{C.14}$$

$$q_{mn}^{12}(\beta, \alpha) = \sum_{(m_1, n_1)=1}^{N} [A_{m_1 n_1}^{\mathrm{SP}}(\beta, \alpha) Q_{11 m_1 n_1, mn}^{12} + B_{m_1 n_1}^{\mathrm{SP}}(\beta, \alpha) Q_{11 m_1 n_1, mn}^{22}], \tag{C.15}$$

$$q_{mn}^{21}(\beta, \alpha) = \sum_{(m_1, n_1)=1}^{N} [B_{m_1 n_1}^{\mathrm{SP}}(\beta, \alpha) Q_{11 m_1 n_1, mn}^{11} + A_{m_1 n_1}^{\mathrm{SP}}(\beta, \alpha) Q_{11 m_1 n_1, mn}^{21}], \tag{C.16}$$

$$q_{mn}^{22}(\beta, \alpha) = \sum_{(m_1, n_1)=1}^{N} [B_{m_1 n_1}^{\mathrm{SP}}(\beta, \alpha) Q_{11 m_1 n_1, mn}^{12} + A_{m_1 n_1}^{\mathrm{SP}}(\beta, \alpha) Q_{11 m_1 n_1, mn}^{22}], \tag{C.17}$$

where

$$Q_{11 m_1 n_1, mn}^{11} = \frac{\mathrm{j}k_2^2}{\pi} \oint_{S_{\mathrm{p}}} \Big\{ [\hat{\mathbf{n}} \times \mathbf{M}_{mn}^1(k_{\mathrm{p}}\cdot)] \cdot \mathbf{N}_{-m_1 n_1}^1(k_2\cdot)$$

$$+ \frac{k_{\mathrm{p}}}{k_2} [\hat{\mathbf{n}} \times \mathbf{N}_{mn}^1(k_{\mathrm{p}}\cdot)] \cdot \mathbf{M}_{-m_1 n_1}^1(k_2\cdot) \Big\} \, \mathrm{d}^2\mathbf{r}_1, \tag{C.18}$$

$$Q_{11 m_1 n_1, mn}^{12} = \frac{\mathrm{j}k_2^2}{\pi} \oint_{S_{\mathrm{p}}} \Big\{ [\hat{\mathbf{n}} \times \mathbf{N}_{mn}^1(k_{\mathrm{p}}\cdot)] \cdot \mathbf{N}_{-m_1 n_1}^1(k_2\cdot)$$

$$+ \frac{k_{\mathrm{p}}}{k_2} [\hat{\mathbf{n}} \times \mathbf{M}_{mn}^1(k_{\mathrm{p}}\cdot)] \cdot \mathbf{M}_{-m_1 n_1}^1(k_2\cdot) \Big\} \, \mathrm{d}^2\mathbf{r}_1, \tag{C.19}$$

$$Q_{11 m_1 n_1, mn}^{21} = \frac{\mathrm{j}k_2^2}{\pi} \oint_{S_{\mathrm{p}}} \Big\{ [\hat{\mathbf{n}} \times \mathbf{M}_{mn}^1(k_{\mathrm{p}}\cdot)] \cdot \mathbf{M}_{-m_1 n_1}^1(k_2\cdot)$$

$$+ \frac{k_{\mathrm{p}}}{k_2} [\hat{\mathbf{n}} \times \mathbf{N}_{mn}^1(k_{\mathrm{p}}\cdot)] \cdot \mathbf{N}_{-m_1 n_1}^1(k_2\cdot) \Big\} \, \mathrm{d}^2\mathbf{r}_1, \tag{C.20}$$

$$Q_{11 m_1 n_1, mn}^{22} = \frac{\mathrm{j}k_2^2}{\pi} \oint_{S_{\mathrm{p}}} \Big\{ [\hat{\mathbf{n}} \times \mathbf{N}_{mn}^1(k_{\mathrm{p}}\cdot)] \cdot \mathbf{M}_{-m_1 n_1}^1(k_2\cdot)$$

$$+ \frac{k_{\mathrm{p}}}{k_2} [\hat{\mathbf{n}} \times \mathbf{M}_{mn}^1(k_{\mathrm{p}}\cdot)] \cdot \mathbf{N}_{-m_1 n_1}^1(k_2\cdot) \Big\} \, \mathrm{d}^2\mathbf{r}_1. \tag{C.21}$$

Actually, the matrix

$$Q_{11} = \left[Q_{11 m_1 n_1, mn} \right] = \begin{bmatrix} Q_{11 m_1 n_1, mn}^{11} & Q_{11 m_1 n_1, mn}^{12} \\ Q_{11 m_1 n_1, mn}^{21} & Q_{11 m_1 n_1, mn}^{22} \end{bmatrix}, \tag{C.22}$$

appears in the null-field method and relates the expansion coefficients of the approximate scattered field to those of the internal field in the global coordinate system, i.e.,

$$\begin{bmatrix} F_{m_1 n_1}^N \\ G_{m_1 n_1}^N \end{bmatrix} = Q_{11} \begin{bmatrix} C_{mn}^N \\ D_{mn}^N \end{bmatrix}. \tag{C.23}$$

In summary, by considering expansions of the dyadic Green's function in terms of vector spherical wave functions and vector plane waves, we obtain the spectral representation for the scattered field (22). In the first case, the Green's function expansion is valid outside a sphere enclosing the particle, i.e., for $z \geq R$, and the spectral amplitudes depend on the expansion coefficients of the scattered field approximation (cf. Eqs. (23)–(24)). In the second case, the Green's function expansion is valid outside a tangent plane bounding the particle from above, i.e., for $z \geq z_{\max}$, and the spectral amplitudes depend on the expansion coefficients of the internal field approximation (cf. Eqs. (C.6)–(C.7)).

For a field point with $z \leq z_{\min} < z_1$, we employ similar arguments. We obtain the integral representation (27) with

$$F^-(\beta, \alpha) = \sum_{(m,n)=1}^{N} [C_{mn}^N q_{mn}^{11}(\pi - \beta, \alpha) + D_{mn}^N q_{mn}^{12}(\pi - \beta, \alpha)], \tag{C.24}$$

$$G^-(\beta, \alpha) = \sum_{(m,n)=1}^{N} [C_{mn}^N q_{mn}^{21}(\pi - \beta, \alpha) + D_{mn}^N q_{mn}^{22}(\pi - \beta, \alpha)]. \tag{C.25}$$

Further we proceed as in the case of a spherical wave expansion of the dyadic Green's function.

1. In the global coordinate system, we obtain the series representation (37) for the interacting field with the expansion coefficients $F_{1m_1 n_1}^N$ and $G_{1m_1 n_1}^N$ as given by Eqs. (38) and (39), respectively, while in the local coordinate system, we obtain the series representation (40) with the expansion coefficients $f_{1m_1 n_1}^N$ and $g_{1m_1 n_1}^N$ as given by Eq. (42)

2. Expansions of the spectral amplitudes $\mathcal{F}^+(\beta, \alpha)$, $\mathcal{F}^-(\beta, \alpha)$, $\mathcal{G}^+(\beta, \alpha)$, and $\mathcal{G}^-(\beta, \alpha)$ in terms of the internal field coefficients C_{mn}^N and D_{mn}^N are obtained in the form

$$\mathcal{F}^+(\beta, \alpha) = \sum_{(m,n)=1}^{N} (\mathscr{F}_{mn}^{1+} C_{mn}^N + \mathscr{G}_{mn}^{1+} D_{mn}^N), \tag{C.26}$$

$$\mathcal{F}^-(\beta, \alpha) = \sum_{(m,n)=1}^{N} (\mathscr{F}_{mn}^{1-} C_{mn}^N + \mathscr{G}_{mn}^{1-} D_{mn}^N), \tag{C.27}$$

$$\mathcal{G}^+(\beta, \alpha) = \sum_{(m,n)=1}^{N} (\mathscr{F}_{mn}^{2+} C_{mn}^N + \mathscr{G}_{mn}^{2+} D_{mn}^N), \tag{C.28}$$

$$\mathcal{G}^-(\beta, \alpha) = \sum_{(m,n)=1}^{N} (\mathscr{F}_{mn}^{2-} C_{mn}^N + \mathscr{G}_{mn}^{2-} D_{mn}^N), \tag{C.29}$$

where

$$\mathscr{F}_{mn}^{1+} = S_\perp^{++} q_{mn}^{11}(\beta, \alpha) + S_\perp^{-+} q_{mn}^{11}(\pi - \beta, \alpha), \tag{C.30}$$

$$\mathscr{G}_{mn}^{1+} = S_\perp^{++} q_{mn}^{12}(\beta, \alpha) + S_\perp^{-+} q_{mn}^{12}(\pi - \beta, \alpha), \tag{C.31}$$

$$\mathscr{F}_{mn}^{1-} = S_\perp^{+-} q_{mn}^{11}(\beta, \alpha) + S_\perp^{--} q_{mn}^{11}(\pi - \beta, \alpha), \tag{C.32}$$

$$\mathscr{G}_{mn}^{1-} = S_\perp^{+-} q_{mn}^{12}(\beta, \alpha) + S_\perp^{--} q_{mn}^{12}(\pi - \beta, \alpha), \tag{C.33}$$

and

$$\mathscr{F}_{mn}^{2+} = S_\parallel^{++} q_{mn}^{21}(\beta, \alpha) + S_\parallel^{-+} q_{mn}^{21}(\pi - \beta, \alpha), \tag{C.34}$$

$$\mathscr{G}_{mn}^{2+} = S_\parallel^{++} q_{mn}^{22}(\beta, \alpha) + S_\parallel^{-+} q_{mn}^{22}(\pi - \beta, \alpha), \tag{C.35}$$

$$\mathscr{F}_{mn}^{2-} = S_\parallel^{+-} q_{mn}^{21}(\beta, \alpha) + S_\parallel^{--} q_{mn}^{21}(\pi - \beta, \alpha), \tag{C.36}$$

$$\mathscr{G}_{mn}^{2-} = S_\parallel^{+-} q_{mn}^{22}(\beta, \alpha) + S_\parallel^{--} q_{mn}^{22}(\pi - \beta, \alpha), \tag{C.37}$$

3. Substituting Eqs. (C.26)–(C.29) in Eqs. (38)–(39), yields

$$\begin{bmatrix} F_{1m_1 n_1}^N \\ G_{1m_1 n_1}^N \end{bmatrix} = RQ_{11} \begin{bmatrix} C_{mn}^N \\ D_{mn}^N \end{bmatrix}, \tag{C.38}$$

and then,

$$\begin{bmatrix} f^N_{\mathrm{Im}_1 n_1} \\ g^N_{\mathrm{Im}_1 n_1} \end{bmatrix} = \mathrm{AQ}_{11} \begin{bmatrix} c^N_{mn} \\ d^N_{mn} \end{bmatrix}, \tag{C.39}$$

where $\mathrm{Q}_{11} = \mathrm{D}\mathcal{Q}_{11}\mathrm{D}^{-1}$ is the matrix which relates the expansion coefficients of the approximate scattered field to those of the internal field in the particle coordinate system. On the other hand, from the null-field equation relating the expansion coefficients of the internal field to those of the external excitation,

$$\mathrm{Q}_{31} \begin{bmatrix} c^N_{mn} \\ d^N_{mn} \end{bmatrix} = -\left(\begin{bmatrix} a^N_{m_1 n_1} \\ b^N_{m_1 n_1} \end{bmatrix} + \begin{bmatrix} f^N_{\mathrm{Im}_1 n_1} \\ g^N_{\mathrm{Im}_1 n_1} \end{bmatrix} \right), \tag{C.40}$$

we find

$$(\mathrm{Q}_{31} + \mathrm{AQ}_{11}) \begin{bmatrix} c^N_{mn} \\ d^N_{mn} \end{bmatrix} = - \begin{bmatrix} a^N_{m_1 n_1} \\ b^N_{m_1 n_1} \end{bmatrix}, \tag{C.41}$$

and then, using the relation $\mathrm{T} = -\mathrm{Q}_{11}\mathrm{Q}_{31}^{-1}$,

$$\begin{bmatrix} f^N_{m_1 n_1} \\ g^N_{m_1 n_1} \end{bmatrix} = \mathrm{Q}_{11} \begin{bmatrix} c^N_{mn} \\ d^N_{mn} \end{bmatrix} = \mathrm{T}(\mathrm{I} - \mathrm{AT})^{-1} \begin{bmatrix} a^N_{m_1 n_1} \\ b^N_{m_1 n_1} \end{bmatrix}. \tag{C.42}$$

Thus, the transition matrix of the system particle–stratified medium is given by

$$\mathrm{T}_{\mathrm{system}} = \mathrm{T}(\mathrm{I} - \mathrm{AT})^{-1} = (\mathrm{T}^{-1} - \mathrm{A})^{-1}. \tag{C.43}$$

This is exactly Eq. (83), and we deduce that both representations for the dyadic Green's function lead to the same result.

Appendix D. Stationary phase evaluation of multidimensional integrals

In this appendix we discuss the stationary phase method for computing the n-dimensional integral

$$I = \int_{\mathbb{R}^n} g(\mathrm{x}) \mathrm{e}^{\mathrm{j}kf(\mathrm{x})} \mathrm{d}^n \mathrm{x}, \tag{D.1}$$

in the limit $k \to \infty$, where by assumption, $g(\mathrm{x})$ is a slowly varying function on $\mathrm{x} = (x_1, \ldots, x_n)$. Let x_{s} be a stationary point of $f(\mathrm{x})$, i.e., $\nabla f(\mathrm{x}_{\mathrm{s}}) = 0$, and consider the Taylor expansion around x_{s},

$$f(\mathrm{x}) = f(\mathrm{x}_{\mathrm{s}}) + \frac{1}{2}(\mathrm{x} - \mathrm{x}_{\mathrm{s}})^T \mathrm{H}(\mathrm{x}_{\mathrm{s}})(\mathrm{x} - \mathrm{x}_{\mathrm{s}}), \tag{D.2}$$

where

$$\mathrm{H}(\mathrm{x}_{\mathrm{s}}) = [\frac{\partial^2 f}{\partial x_i \partial x_j}(\mathrm{x}_{\mathrm{s}})] \tag{D.3}$$

is the Hessian matrix of f at x_{s}. Set $\widetilde{\mathrm{x}} = \mathrm{x} - \mathrm{x}_{\mathrm{s}}$, to obtain

$$(\mathrm{x} - \mathrm{x}_{\mathrm{s}})^T \mathrm{H}(\mathrm{x}_{\mathrm{s}})(\mathrm{x} - \mathrm{x}_{\mathrm{s}}) = \widetilde{\mathrm{x}}^T \mathrm{H}(0)\widetilde{\mathrm{x}}. \tag{D.4}$$

Assume that the Hessian is positive definite, i.e., that x_{s} is a local minimum. Because H is symmetric and positive definite, its eigenvalues are positive, and we have the eigendecomposition

$$\mathrm{H}(0) = \mathrm{V}\varLambda \mathrm{V}^T, \tag{D.5}$$

where V is the orthonormal matrix of the eigenvectors, and $\varLambda$ is the diagonal matrix of the eigenvalues, $\varLambda = [\mathrm{diag}(\lambda_i)]$. By the change of variable $y = \mathrm{V}^T \widetilde{\mathrm{x}}$, we obtain

$$(\mathrm{x} - \mathrm{x}_{\mathrm{s}})^T \mathrm{H}(\mathrm{x}_{\mathrm{s}})(\mathrm{x} - \mathrm{x}_{\mathrm{s}}) = y^T \varLambda y. \tag{D.6}$$

From $\widetilde{\mathrm{x}} = \mathrm{V}y$ and $|\det(\mathrm{V})| = 1$, we deduce that the determinant of the Jacobian matrix $\partial \widetilde{\mathrm{x}}/\partial y$ is one, i.e.,

$$|\det(\frac{\partial \widetilde{\mathrm{x}}}{\partial y})| = |\det(\mathrm{V})| = 1, \tag{D.7}$$

and so, that the coordinates transformation is

$$\mathrm{d}^n \widetilde{\mathrm{x}} = |\det(\frac{\partial \widetilde{\mathrm{x}}}{\partial y})|\mathrm{d}^n y = \mathrm{d}^n y. \tag{D.8}$$

Because by assumption, $g(\mathrm{x})$ is a slowly varying function on x, we find

$$I \approx g(\mathrm{x}_{\mathrm{s}})\mathrm{e}^{\mathrm{j}kf(\mathrm{x}_{\mathrm{s}})} \int_{\mathbb{R}^n} \mathrm{e}^{\mathrm{j}\frac{1}{2}k\widetilde{\mathrm{x}}^T \mathrm{H}(0)\widetilde{\mathrm{x}}} \mathrm{d}^n \widetilde{\mathrm{x}}$$

$$= g(\mathrm{x}_{\mathrm{s}})\mathrm{e}^{\mathrm{j}kf(\mathrm{x}_{\mathrm{s}})} \int_{\mathbb{R}^n} \mathrm{e}^{\mathrm{j}\frac{1}{2}ky^T \varLambda y} \mathrm{d}^n y = \left(\frac{2\pi}{k}\right)^{n/2} \frac{g(\mathrm{x}_{\mathrm{s}})}{\sqrt{\prod \lambda_i}} \mathrm{e}^{\mathrm{j}kf(\mathrm{x}_{\mathrm{s}})+\mathrm{j}\frac{n\pi}{4}}, \tag{D.9}$$

where we made use of the result

$$\int_{-\infty}^{\infty} \mathrm{e}^{\mathrm{j}\frac{1}{2}\sigma y^2} \mathrm{d}y = \sqrt{\frac{2\pi}{\sigma}} \mathrm{e}^{\mathrm{j}\frac{\pi}{4}}. \tag{D.10}$$

Finally, taking into account that

$$\prod_i \lambda_i = \det(\varLambda) = \det[\mathrm{H}(0)] > 0, \tag{D.11}$$

we end up with

$$I \approx \left(\frac{2\pi}{k}\right)^{n/2} \frac{g(\mathrm{x}_{\mathrm{s}})}{\sqrt{\det[\mathrm{H}(\mathrm{x}_{\mathrm{s}})]}} \mathrm{e}^{\mathrm{j}kf(\mathrm{x}_{\mathrm{s}})+\mathrm{j}\frac{n\pi}{4}}. \tag{D.12}$$

If x_{s} is a saddle point for f, then the Hessian matrix has both positive and negative eigenvalues. In this case, the stationary phase approximation is

$$I \approx \left(\frac{2\pi}{k}\right)^{n/2} \frac{g(\mathrm{x}_{\mathrm{s}})}{\sqrt{\left| \det[\mathrm{H}(\mathrm{x}_{\mathrm{s}})] \right|}} \mathrm{e}^{\mathrm{j}kf(\mathrm{x}_0)+\mathrm{j}\frac{\sigma\pi}{4}}, \tag{D.13}$$

where σ the signature of the Hessian matrix (the number of positive eigenvalues minus the number of negative eigenvalues).

Consider now the integral

$$I = \int_0^{2\pi} \int_0^{\frac{\pi}{2}-\mathrm{j}\infty} g(\beta, \alpha)\mathrm{e}^{\mathrm{j}k\hat{\mathbf{s}}(\beta,\alpha)\cdot\mathbf{r}} \sin\beta \mathrm{d}\beta \mathrm{d}\alpha, \tag{D.14}$$

with

$$\hat{\mathbf{s}}(\beta, \alpha) = \sin\beta\cos\alpha\hat{\mathbf{x}} + \sin\beta\sin\alpha\hat{\mathbf{y}} + \cos\beta\hat{\mathbf{z}},$$

$$\mathbf{r} = r(\sin\theta\cos\varphi\hat{\mathbf{x}} + \sin\theta\sin\varphi\hat{\mathbf{y}} + \cos\theta\hat{\mathbf{z}}).$$

The stationary point $(\beta_{\mathrm{s}}, \alpha_{\mathrm{s}})$ of the function

$$f(\beta, \alpha) = \hat{\mathbf{s}}(\beta, \alpha) \cdot \mathbf{r} = r[\cos\beta\cos\theta + \sin\beta\sin\theta\cos(\varphi - \alpha)]$$

is

$$\beta_{\mathrm{s}} = \theta, \quad \alpha_{\mathrm{s}} = \varphi,$$

and the Hessian matrix is

$$\mathrm{H}(\beta_{\mathrm{s}}, \alpha_{\mathrm{s}}) = \begin{bmatrix} -r & 0 \\ 0 & -r\sin^2\theta \end{bmatrix}.$$

Hence, the signature and the determinant of H are $\sigma = -2$ and $\det[\mathrm{H}(\beta_{\mathrm{s}}, \alpha_{\mathrm{s}})] = r^2 \sin^2\theta$, respectively, and we get

$$I \approx -\mathrm{j}\frac{2\pi}{kr} g(\theta, \varphi)\mathrm{e}^{\mathrm{j}kr}. \tag{D.15}$$

References

[1] Israelachvili J. Intermolecular and surface forces. Elsevier; 2011, http://dx.doi.org/10.1016/c2009-0-21560-1.

[2] Berg JC. An introduction to interfaces and colloids: the bridge to nanoscience. WORLD SCIENTIFIC; 2009, http://dx.doi.org/10.1142/7579.

[3] Goreke U, Iram S, Singh G, Domínguez-Medina S, Man Y, Bode A, et al. Catch bonds in sickle cell disease: Shear-enhanced adhesion of red blood cells to laminin. Biophys J 2023;122(12):2564–76. http://dx.doi.org/10.1016/j.bpj.2023.05.010.

[4] Suresh L, Walz JY. Effect of surface roughness on the interaction energy between a colloidal sphere and a flat plate. J Colloid Interface Sci 1996;183(1):199–213. http://dx.doi.org/10.1006/jcis.1996.0535.

[5] Weroński P, Walz JY, Elimelech M. Effect of depletion interactions on transport of colloidal particles in porous media. J Colloid Interface Sci 2003;262(2):372–83. http://dx.doi.org/10.1016/s0021-9797(03)00174-7.

[6] Lee K, Das M, Pitell M, Wirth CL. Surfactant induced catastrophic collapse of carbon black suspensions used in flow battery application. J Colloid Interface Sci 2023;633:712–22. http://dx.doi.org/10.1016/j.jcis.2022.11.097.

[7] Hipp JB, Richards JJ, Wagner NJ. Structure-property relationships of sheared carbon black suspensions determined by simultaneous rheological and neutron scattering measurements. J Rheol 2019;63(3):423–36. http://dx.doi.org/10.1122/1.5071470.

[8] Jiang J-S, Guo R-H, Chiu Y-S, Hua C-C. Percolation behaviors of model carbon black pastes. Soft Matter 2018;14(48):9786–97. http://dx.doi.org/10.1039/c8sm01591k.

[9] Das M, Chambon L, Varga Z, Vamvakaki M, Swan JW, Petekidis G. Shear driven vorticity aligned flocs in a suspension of attractive rigid rods. Soft Matter 2021;17(5):1232–45. http://dx.doi.org/10.1039/d0sm01576h.

[10] Khalkhal F, Negi AS, Harrison J, Stokes CD, Morgan DL, Osuji CO. Evaluating the dispersant stabilization of colloidal suspensions from the scaling behavior of gel rheology and adsorption measurements. Langmuir 2017;34(3):1092–9. http://dx.doi.org/10.1021/acs.langmuir.7b03343.

[11] Prieve DC, Frej NA. Total internal reflection microscopy: a quantitative tool for the measurement of colloidal forces. Langmuir 1990;6(2):396–403. http://dx.doi.org/10.1021/la00092a019.

[12] Prieve DC. Measurement of colloidal forces with TIRM. Adv Colloid Interface Sci 1999;82(1–3):93–125. http://dx.doi.org/10.1016/s0001-8686(99)00012-3.

[13] Juárez JJ, Cui J-Q, Liu BG, Bevan MA. Kt-scale colloidal interactions in high frequency inhomogeneous ac electric fields. I. Single particles. Langmuir 2011;27(15):9211–8. http://dx.doi.org/10.1021/la201478y.

[14] Biggs S, Dagastine RR, Prieve DC. Oscillatory packing and depletion of polyelectrolyte molecules at an oxide-water interface. J Phys Chem B 2002;106(44):11557–64. http://dx.doi.org/10.1021/jp026425k,.

[15] Gong X, Wang Z, Ngai T. Direct measurements of particle-surface interactions in aqueous solutions with total internal reflection microscopy. Chem Commun 2014;50(50):6556–70. http://dx.doi.org/10.1039/c4cc00624k,.

[16] Swavola JC, Edwards TD, Bevan MA. Direct measurement of macromolecule-coated colloid-mucus interactions. Langmuir 2015;31(33):9076–85. http://dx.doi.org/10.1021/acs.langmuir.5b01460,.

[17] Edwards TD, Bevan MA. Depletion-mediated potentials and phase behavior for micelles, macromolecules, nanoparticles, and hydrogel particles. Langmuir 2012;28(39):13816–23. http://dx.doi.org/10.1021/la302805n,.

[18] Bevan MA, Prieve DC. Forces and hydrodynamic interactions between polystyrene surfaces with adsorbed PEO-PPO-PEO. Langmuir 2000;16(24):9274–81. http://dx.doi.org/10.1021/la0006869,.

[19] Doicu A, Vasilyeva A, Efremenko D, Wirth C, Wriedt T. A light scattering model for total internal reflection microscopy of geometrically anisotropic particles. J Modern Opt 2019;66:1139–51. http://dx.doi.org/10.1080/09500340.2019.1605005.

[20] Rashidi A, Domínguez-Medina S, Yan J, Efremenko D, Vasilyeva A, Doicu A, et al. Developing scattering morphology resolved total internal reflection microscopy (SMR-TIRM) for orientation detection of colloidal ellipsoids. Langmuir 2020;36:13041–50. http://dx.doi.org/10.1021/acs.langmuir.0c02482.

[21] Yan J, Efremenko DS, Vasilyeva AA, Doicu A, Wriedt T, Wirth C. Scattering morphology resolved total internal reflection microscopy (SMR-TIRM) of colloidal spheres. Comput Math Model 2021;32(1):86–93. http://dx.doi.org/10.1007/s10598-021-09518-x.

[22] Yan J, Wirth CL. Anisotropic colloidal particles near boundaries. J Appl Phys 2022;131(15). http://dx.doi.org/10.1063/5.0089206,.

[23] Vasilyeva A, Efremenko D, Doicu A. Image simulator for the total internal reflection microscopy. In: Lomonosov's readings. Moscow State University; 2020, p. 22–3.

[24] Egel A, Czajkowski K, Theobald D, Ladutenko K, Kuznetsov A, Pattelli L. SMUTHI: A python package for the simulation of light scattering by multiple particles near or between planar interfaces. J Quant Spectrosc Radiat Transfer 2021;273:107846. http://dx.doi.org/10.1016/j.jqsrt.2021.107846.

[25] Stein S. Addition theorem for spherical wave functions. Quart Appl Math 1961;19:15–24. http://dx.doi.org/10.1090/QAM/120407.

[26] Egel A, Theobald D, Donie Y, Lemmer U, Gomard G. Light scattering by oblate particles near planar interfaces: on the validity of the T-matrix approach. Opt Express 2016;24:25154–68. http://dx.doi.org/10.1364/OE.24.025154.

[27] Egel A, Eremin Y, Wriedt T, Theobald D, Lemmer U, Gomard G. Extending the applicability of the T-matrix method to light scattering by flat particles on a substrate via truncation of sommerfeld integrals. J Quant Spectrosc Radiat Transfer 2017;202:279–85. http://dx.doi.org/10.1016/j.jqsrt.2017.08.016.

[28] Doicu A, Wriedt T, Eremin Y. Light scattering by systems of particles. Springer Berlin Heidelberg; 2006, http://dx.doi.org/10.1007/978-3-540-33697-6.

[29] Egel A. Accurate optical simulation of disordered scattering layers for light extraction from organic light emitting diodes [Ph.D. thesis], 2019, http://dx.doi.org/10.5445/IR/1000093961.

[30] Chew W. Waves and fields in inhomogeneous media. New York: IEEE Press; 1995.

[31] Bobbert P, Vlieger J. Light scattering by a sphere on a substrate. Physica 1986;137A:209–41. http://dx.doi.org/10.1016/0378-4371(86)90072-5.

[32] Bobbert P, Vlieger J, Greef R. Light reflection from a substrate sparsely seeded with spheres — comparison with an ellipsometric experiment. Physica 1986;137A:243–57. http://dx.doi.org/10.1016/0378-4371(86)90073-7.

[33] Barber P, Hill S. Light scattering by particles: Computational methods. Singapore: World Scientific; 1990, http://dx.doi.org/10.1142/0784.

[34] Leutenegger M, Rao R, Leitgeb R, Lasser T. Fast focus field calculations. Opt Express 2006;14:11277–91. http://dx.doi.org/10.1364/OE.14.011277.

[35] Sannomiya T, Balmer TE, Heuberger M, Vörös J. Simultaneous refractive index and thickness measurement with the transmission interferometric adsorption sensor. J Phys D: Appl Phys 2010;43(40):405302. http://dx.doi.org/10.1088/0022-3727/43/40/405302,.

[36] Johnson B. Invariant imbedding t matrix approach to electromagnetic scattering. Appl Opt 1988;27:4861–73. http://dx.doi.org/10.1364/AO.27.004861.

[37] Doicu A, Wriedt T, Khebbache N. An overview of the methods for deriving recurrence relations for T-matrix calculation. J Quant Spectrosc Radiat Transfer 2019;224:289–302. http://dx.doi.org/10.1016/j.jqsrt.2018.11.029.

[38] Bi L, Yang P, Kattawar G, Mishchenko M. Efficient implementation of the invariant imbedding T-matrix method and the separation of variables method applied to large nonspherical inhomogeneous particles. J Quant Spectrosc Radiat Transfer 2013;116:169–83. http://dx.doi.org/10.1016/j.jqsrt.2012.11.014.

[39] Doicu A, Wriedt T. Plane wave spectrum of electromagnetic beams. Opt Commun 1997;136(1–2):114–24. http://dx.doi.org/10.1016/s0030-4018(96)00641-4.

[40] Ko D, Sambles J. Scattering matrix method for propagation of radiation in stratified media: attenuated total reflection studies of liquid crystals. J Opt Soc Amer A 1988;5:1863–6. http://dx.doi.org/10.1364/JOSAA.5.001863.